UNIVERSITY OF OKLAHOMA

GRADUATE COLLEGE

COUPLING THE ADVANCED REGIONAL PREDICTION SYSTEM AND THE DISCRETE EVENT SPECIFICATION FIRE SPREAD MODEL TO PREDICT WILDFIRE BEHAVIOR

A DISSERTATION

SUBMITTED TO THE GRADUATE FACULTY

in partial fulfillment of the requirements for the

Degree of

DOCTOR OF PHILOSOPHY

By

NATHAN AARON DAHL
Norman, Oklahoma
2014

COUPLING THE ADVANCED REGIONAL PREDICTION SYSTEM AND THE DISCRETE EVENT SPECIFICATION FIRE SPREAD MODEL TO PREDICT WILDFIRE BEHAVIOR

A DISSERTATION APPROVED FOR THE
SCHOOL OF METEOROLOGY

BY

_____
Dr. Ming Xue, Chair

_____
Dr. Keith Brewster

_____
Dr. Brian Fiedler

_____
Dr. Yang Hong

_____
Dr. Alan Shapiro

Acknowledgements

My foremost thanks must go to Dr. Ming Xue for obtaining the funding that made this research possible (NSF Grants CNS-0941432, CNS-0941491, and CNS-0940134) and for arranging for my position on this project in an incredibly timely fashion. I extend additional thanks to him and Dr. Keith Brewster, Dr. Brian Fiedler, Dr. Yang Hong, and Dr. Alan Shapiro for serving on my dissertation committee and freely providing collaboration, advice, and constructive criticism whenever it was requested. I am also grateful to the research scientists and staff at the Center for Analysis and Prediction of Storms (too many to list here) who provided much-needed encouragement and technical support over the last four years.

This work would not have been possible without the supercomputing resources provided by the OU Supercomputing Center for Education and Research (Boomer), Oak Ridge Laboratory (Kraken), and the San Diego Supercomputing Center (Gordon). Equally essential was the assistance of Haidong Xue, who was regularly charged with augmenting the DEVS-FIRE code as potential improvements were proposed. Collaboration with Dr. Xiaolin Hu and Dr. Lewis Ntaimo was crucial in shaping the course of the project and obtaining necessary background data. The free use of fuel and terrain data from the Texas Forest Service, background weather data from the National Climatic Data Center and the National Center for Environmental Prediction, and high-resolution FIREFLUX observations from Dr. Craig Clements were absolutely vital and immensely appreciated. All of these entities have my enduring gratitude.

Lastly, I express all of my gratitude and love to my wife, Brittany, and my family. Without your inspiration and support, this effort would never have been completed.

Table of Contents

List of Tables

List of Figures

Abstract

The cost of wildfire suppression in the United States has risen dramatically over the last 20 years. As the interface between wildland and urban areas expands, increased emphasis is being placed on rapid, efficient deployment of firefighting resources. Various numerical models of wildfire spread have been developed to assist wildfire management efforts over the last several decades; however, the use of coupled fire-weather models to capture important feedbacks between the wildfire and the atmosphere is a relatively new development.

This research evaluates a coupled system consisting of the Advanced Regional Prediction System (ARPS) atmospheric model and the raster-based Discrete Event Specification Fire Spread model (DEVS-FIRE). After the theoretical basis of coupled fire-atmosphere modeling and the basic design of previous vector-based models are outlined, idealized tests, verification using data from the FIREFLUX experiment, and case studies of the September 2000 Moore Branch Fire and the April 2011 Rock House Fire are presented. The current version of ARPS/DEVS-FIRE produces mixed results; broader-scale feedbacks appear to be represented somewhat skillfully, but the model also exhibits systematic flaws, which are exacerbated by efforts to depict fine-scale feedbacks or fire spread in high-wind cases. These results demonstrate the importance of coupled modeling and suggest improvements that must be made to ARPS/DEVS-FIRE before reliable results may be obtained.

CHAPTER 1

INTRODUCTION

Although the question of proper wildfire management is complicated by the recognized benefits of naturally-occurring burns to certain ecosystems (Keene et al., 2008), the negative impact on human interests is well-documented. In 2012, wildfires in the United States alone consumed over 37000 km^2, destroyed over 4000 man-made structures, and killed 15 firefighters employed by the Unites States Forest Service and Department of the Interior (DOI; see U.S. Library of Congress, 2013). This occurred despite a susbtantial increase in government resources dedicated to wildfire management in recent years, with DOI fire-related appropriations increasing from roughly $1.5 billion (adjusted) for FY 1999 to roughly $2.7 billion for FY 2011 (Office of Policy Analysis 2012).

Moreover, these statistics do not include "indirect" wildfire costs, including the impact of air quality hazards (soot and gaseous by-products) on the health of general population, additional risk of flooding due to altered hydrological properties in the burn areas, and declines in property value and tourism near the damage swath (Western Forestry Leadership Coalition, 2010). With the expectation that conditions conducive to wildfires will occur more often and with greater intensity and duration due to global climate change (Intergovernmental Panel on Climate Change, 2007), there is increased urgency to develop greater understanding of wildfire behavior and greater ability to predict wildfire spread in order to optimize the use of firefighting resources and personnel.

While the general atmospheric conditions conducive to wildfire ignition are well understood (with high temperatures, very low relative humidity, and high winds over regions of dried fuels such as timber or brush listed by Novy et al., 2013), accurate prediction of subsequent wildfire intensity and rate of spread has proven far more elusive. One error source stems from continuing uncertainties regarding the radiative properties and chemical processes responsible for fire spread through wildland fuels. Controlled burns and laboratory tests have aided in the development of semi-empirical mathematical models to combat this uncertainty, but they generally necessitate a simplistic representation of fuel bed characteristics (e.g. continuous and/or homogeneous) that constitutes another error source. Furthermore, the sensitivity of wildfire behavior to fuel characteristics (moisture, depth, slope, fuel element shape, etc.) threatens additional spread model errors due to sparse spatial and temporal sampling of fuel beds, particularly in rural areas. (See Albini, 1976.)

However, the main source of difficulty is the rapidly-evolving interaction between the fire and the atmosphere above it (Sun et al., 2008). Because the behavior of the leading edge of the fire (hereafter "fire front") is heavily influenced by near-surface atmospheric conditions (particularly wind speed and direction; see Rothermel, 1972) and near-surface atmospheric conditions may be strongly influenced by heat release from the fire, nonlinear feedbacks can contribute to rapid evolution of the fire front. These feedbacks can lead to wildly unpredictable behavior even in wildfires that are seemingly contained, with consequent danger to the resources and lives of firefighting personnel (e.g. the deaths of 15 firefighters due to rapid growth of a spot ignition during the 1953 Rattlesnake Fire in California as described in Cliff et al., 1953).

A relatively recent innovation is the development of coupled fire-atmosphere models seeking to capture these feedbacks. These models essentially consist of a component dedicated to simulating wildfire spread and associated heat release, a component dedicated to simulating the evolution of the atmosphere above the burn area, and an interface through which those components exchange relevant information. The representation of physical processes in these models can be quite complex; for example, the FIRETEC model (Linn and Cunningham, 2005) obtains wildfire heat release rates from explicit calculation of the rate of combustion based on the proportions of the key reactants (specifically oxygen, solid fuel, and water) in a given fuel bed. However, FIRETEC is unable to run faster than real-time due to this complexity, even with recent advances in computational capabilities.

In order to obtain true forecasts to assist wildfire management efforts, other models estimate combustion rates from simple empirical or semi-empirical formulas based on averaged fuel characteristics such as those detailed in Anderson (1982). Even in this approach, however, simulating the temporal evolution of the fire front can incur significant computational cost. With the fire spreading through the fuel bed as a contiguous wave, the shape of the front changes as spatial variations in fuel, terrain, and surface winds alter the local spread rate. Because the atmospheric response to the fire is influenced by the shape of the fire front, these changes must be coherently tracked. One popular method is to treat the fire as a polygon spreading outward from the initial point of ignition, as in the CAWFE model (Clark et al., 2004) and the WRF-SFIRE model (Mandel et al., 2011). However, such vector-based methods are still

comparatively expensive since the polygon must be monitored as a separate entity whose geometry becomes increasingly complex over time.

In an effort to streamline the representation of the fire front while retaining forecast accuracy, raster-based treatments of fire spread have also been developed. In this approach, the fire is represented as a cluster of discrete cells, which evolves as the fire spreads from each ignited cell to its neighbors. This localized approach is far more efficient than a polygon-based method, and becomes even more so when implemented as a cellular automaton with each cell acting as an independent "agent." (See Clarke et al., 1994.) However, since this approach is more likely than a vector-based approach to significantly distort the fire front shape (Cui and Perera, 2008), the suitability of coupling a raster-based representation of fire spread to an atmospheric model is uncertain.

To investigate the utility of using such a model in a coupled framework as a tool to aid wildfire management, the raster-based Discrete Event Specification Fire spread model (DEVS-FIRE) has been coupled to the Advanced Regional Prediction System atmospheric model (ARPS). This account of the project will proceed as follows: Chapter 2 will provide a review of literature detailing the theoretical understanding of wildfire spread and an overview of existing fire spread models; Chapter 3 will describe the individual DEVS-FIRE and ARPS models, detail the methods used to couple them together, and outline the tests to which the coupled model was subjected; Chapter 4 will describe and discuss the test results; and Chapter 5 will provide a summary of conclusions as well as topics for future study.

CHAPTER 2

LITERATURE REVIEW

A. Principles of Biomass Combustion and Wildfire Spread

A wildfire is essentially a process of sustained, progressive, energetic oxidation of a layer of biomass. The first difficulty in modeling this process lies in the fact that wildland fuels are chemically-complex combinations of celluloses and lignins with uncertain molecular masses; therefore, Byram (1959) summarized complete oxidation of the fuel as a single-step chemical reaction:

$$4C_6H_9O_4 + 25O_2 + [0.322M H_2O + 94.0N_2] \rightarrow 18H_2O + 24CO_2 + [0.322M H_2O + 94.0N_2] + 11.6\ \text{MJ} \quad (1)$$

Here, M is the moisture content as a percentage of the ovendry fuel mass and the proportional carbon, hydrogen, and oxygen content in the wildland fuel is represented by the "composite" molecule $C_6H_9O_4$.

However, as also indicated by Byram, wildland fuel combustion is actually a complicated, multi-stage process. The initial phase involves drying and *pre-heating* the fuel, which is accomplished by warm, dry atmospheric conditions and/or radiation from an approaching fire front. This is followed by *pyrolysis*, where the fuel releases volatile gasses (which then combust) and transforms into char. Finally, *burning* the charcoal produces ash and other by-products. The chemical reactants and products in each of these phases vary widely depending on the reaction temperature and the stoichiometric ratio of fuel to available oxygen. For example, pyrolysis at higher temperatures

produces char with higher carbon content, and incomplete combustion produces carbon monoxide and NO_x as additional by-products.

As described previously, some fire spread models (e.g. FIRETEC) seek to specifically model the evolution of the main constituents though each step of the process in order to calculate the heat released by the combustion and the transfer of heat from the fire to adjacent unburned fuel. However, such models are too complex to run faster than real-time to provide useful forecasts; such speeds have been attainable only by treating the fuel bed as a uniform slab, with fire behavior governed by bulk characteristics defined by fuel type. Anderson (1982) indicated that, for a given fuel

Table 1: Properties of standard wildland fuel types (from Anderson, 1982)

Fuel Type	Fuel load ($kg\ m^{-2}$)	Dead fuel ($kg\ m^{-2}$)	Live foliage ($kg\ m^{-2}$)	Fuel depth (m)	S-V ratio (m^{-1})	Burn time (s)	Extinction Moisture (%)
1 Short grass	0.180	0.180	0.0	0.305	11483	8.2	12
2 Timber (grass and understory)	0.972	0.486	0.122	0.305	9134	8.2	15
3 Tall grass	0.730	0.730	0.0	0.762	4921	8.2	25
4 Chaparral	3.162	1.216	1.216	1.829	5705	211.4	20
5 Brush (2 ft)	0.851	0.243	0.486	0.610	9134	117.5	20
6 Dormant brush/hard-wood slash	1.459	0.365	0.0	0.762	9134	117.5	25
7 Southern rough	1.192	0.268	0.097	0.762	9134	117.5	40
8 Closed timber litter	1.216	0.365	0.0	0.061	9134	1057.1	30
9 Hardwood litter	0.851	0.705	0.0	0.061	8150	1057.1	25
10 Timber (litter and understory)	2.918	0.730	0.486	0.305	5787	1057.1	25
11 Light logging slash	2.797	0.365	0.0	0.305	5787	1057.1	15
12 Medium logging slash	8.414	0.972	0.0	0.701	5787	1057.1	20
13 Heavy logging slash	14.130	1.702	0.0	0.914	5787	1057.1	25

type, the most important of characteristics for predicting fire spread rate and intensity are the total fuel load (mass per unit area of the fuel bed), the fuel depth, the proportions of dead fuel mass and live foliage to the total load, and the characteristic surface-to-volume (S-V) ratio of the fuel elements. Anderson detailed 13 standard fuel types, the characteristics of which are summarized in Table 1.

The first theoretical model of ground fire spread through a uniform fuel bed was developed by Frandsen (1971). Assuming conservation of energy and defining a coordinate system relative to a fire front moving in the *–x* direction, Frandsen conceptually framed the problem as a propagating flux through unburned fuel elements ahead of the fire front. In this framework, the spread rate is expressed as the ratio of the energy absorbed by the unburned fuel element (per unit time) to the energy required to ignite the fuel element:

$$R = \frac{I_{xig} + \int_{-\infty}^{0} \left(\frac{\partial I_z}{\partial z}\right)_{z_c} dx}{\rho_{be} Q_{ig}} \quad (2)$$

R is the spread rate (m s^{-1}). The propagating flux (W m^{-2}) is the sum of the horizontal heat flux absorbed by a unit volume of igniting fuel I_{xig} and the vertical radiative flux convergence evaluated within the combustion zone $\left(\frac{\partial I_z}{\partial z}\right)_{z_c}$ integrated along the path the fuel element travels to the fire front. ρ_{be} is the effective bulk density of the fuel (kg/m^3) and Q_{ig} is the heat required to bring a unit weight of fuel to ignition (J kg^{-1}).

Rothermel (1972) developed the most wildly-used mathematical definition of spread rate by building on Frandsen's conceptual framework. From (2), Rothermel

surmised that near-surface winds and topography (i.e. slope) affect fire spread by modifying the vertical radiative flux convergence term as shown in Fig. 1; where strong winds blow across the fire front and/or the ground slopes upward in the direction of spread, the flames at the leading edge are tilted downstream and/or upslope and the flux convergence in the unburned fuel ahead of the fire front is enhanced. Furthermore, stronger winds increase the potential that the fuel will be ignited directly through contact with the flames at the leading edge or burning material lofted ahead of the fire front (hereafter "firebrands").

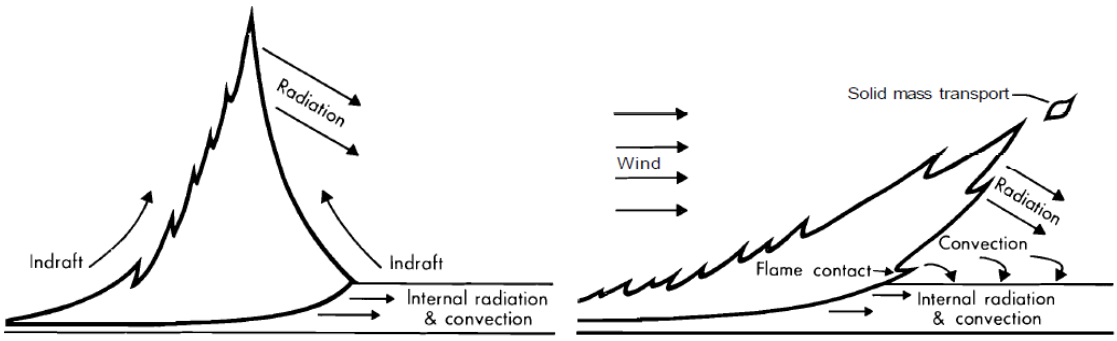

Figure 1: Impact of wind on heating of unburned fuel ahead of the fire front. (from Rothermel, 1972, p. 12)

Rothermel also expanded on Frandsen's model by determining empirical relationships between the terms in (2) and known properties of the fuel element and its environment. For instance, asserting that the zero-wind-zero-slope propagating flux I_{p0} is a function of the reaction intensity at the fire front, Rothermel proposed a relationship for the total propagating flux of the form

$$I_p = I_{p0}\,(1+\phi_s+\phi_w) \tag{3}$$

where φ_s and φ_w are dimensionless wind and slope coefficients tied to the characteristics of the fuel bed. By experimental burns through excelsior beds and cribs of sticks ¼-inch and ½-inch in diameter set on a variety of slopes, Rothermel determined the empirical relationship

$$\phi_s = 5.275\ \beta^{-0.3}\ (\tan\phi)^2 \tag{4}$$

where β is the packing ratio (a dimensionless measure of the amount of empty space present in the fuel bed, equal to the ratio of the total fuel bed density to the density of the individual fuel elements) and ϕ is the slope. For the wind, Rothermel obtained

$$\phi_w = CU^B\ (\beta/\ \beta_{op})^{-E} \qquad \text{where} \tag{5}$$

$$C = 7.47\ \exp(-0.133\ \sigma^{0.55})$$

$$B = 0.02526\ \sigma^{0.54} \tag{6}$$

$$E = 0.715\ \exp(-0.000359\ \sigma)$$

U is the wind speed across the fire front at midflame height (m s^{-1}), σ is the S-V ratio (m^{-1}), and β_{op} is an "optimum" packing ratio derived from further experiments (inversely proportional to the S-V ratio). As expected, these relations show an increase in propagating flux as wind speed or slope increases; they also show enhancement with increased S-V ratio (due to a larger fraction of the fuel element being available for combustion at any given time) and diminishment with increased packing ratio (due to attenuation and lack of ventilation in dense fuel beds).

Furthermore, Rothermel postulated that I_{p0} is proportional to the reaction intensity I_R; through zero-wind-zero-slope experimental burns, an empirical fit for the proportionality constant was found to be

$$\xi = I_{p0}/I_R = (192 + 0.259\sigma)^{-1}\exp[(0.792 + 0.681\sigma^{0.5})(\beta + 0.1)] \quad (7)$$

Thus, when wind and slope are not a factor, packing ratio *increases* the propagating flux for a given reaction intensity; this illustrates the importance of quantitative solutions for real cases where the packing ratio, wind, and slope may be working at cross purposes with respect to their impacts on the propagating flux. The reaction intensity is defined simply as the rate of fuel mass combustion multiplied by the heat content per unit mass of the fuel. The rate of combustion is affected by the fuel load, packing ratio, S-V ratio, and the presence of moisture and impurities in the fuel. Thus, Rothermel expressed the reaction intensity as

$$I_R = \Gamma' w_n h n_M n_s \quad (8)$$

where Γ' is an experimentally-determined optimum reaction velocity (s^{-1}), w_n is the fuel loading (kg m^{-2}), h is the fuel heat content (J kg^{-1}), and n_M and n_S are experimentally-determined dimensionless damping coefficients for moisture and mineral content, respectively.

Finally, the heat of preignition Q_{ig} is also affected by the moisture content of the fuel, formulized by Rothermel as

$$Q_{ig} = c_{pd}\Delta T_{ig} + M_f\,(c_{pw}\Delta T_B + V) \quad (9)$$

c_{pd} and c_{pw} are the specific heats of the dry fuel and the water contained in it (J kg^{-1}), respectively. ΔT_{ig} is the temperature change required to bring the dry fuel to ignition, while and ΔT_B is the temperature required to bring the water to its boiling point (K). M_f is the fractional fuel moisture content (dimensionless) and V is the latent heat of vaporization for water. Thus, the final form of the Rothermel formula for spread rate, with all quantities determined by the fuel characteristics and environment, is

$$R = \frac{I_R \xi (1+\varphi_s+\varphi_w)}{\rho_{be} Q_{ig}} \tag{10}$$

However, it is clear that a wildfire igniting at a specific point does not only spread in directions dictated by the wind and slope. It propagates in all directions due to atmospheric turbulence, radiation, conduction between burning and unburned fuel elements, and so forth. Since it is not feasible to directly model these impacts, the evolution of the two-dimensional shape of the fire front must also be parameterized. As noted by Anderson (1983), observations from test fires in a variety of fuels (e.g. pine litter in Fons, 1940; grass fuels in Cheney and Bary, 1969) suggest an elliptical front shape, with the length-to-width ratio varying according to the slope, the wind speed at midflame height, and the fuel type. Anderson indicated that the best agreement with observations was obtained by splitting the fire front along the line normal to the direction of maximum spread and fitting a semi-ellipse to each side, with hundreds of experimental burns used to derive empirical relationships between the semi-ellipse dimensions and the factors listed above. (See Fig. 2.) Simple elliptical or semi-elliptical parameterizations of this sort form the basis of most operational fire spread models, such as the Fire Area Simulator (FARSITE; see Finney, 1998).

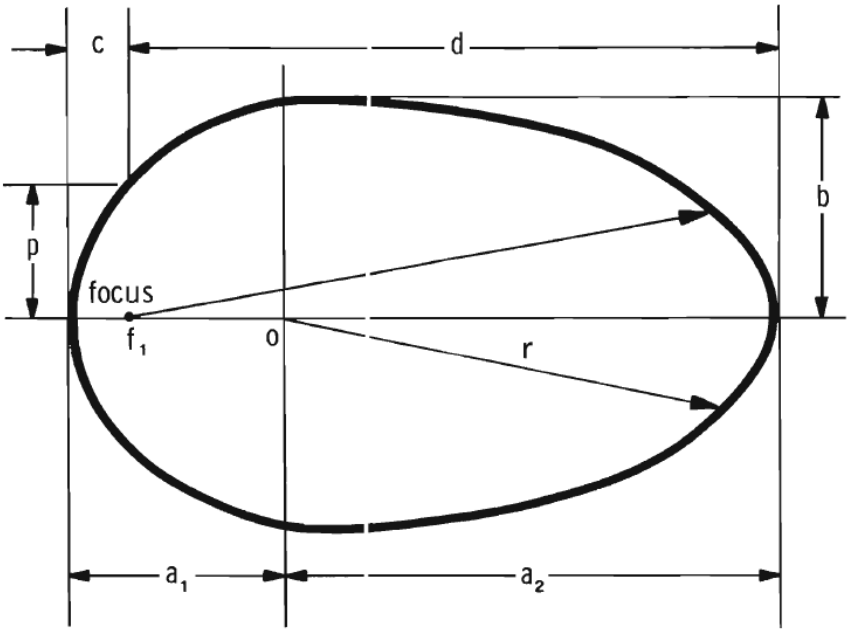

Figure 2: Example of idealized fire front shape obtained by joining semi-ellipses fitted to Rothermel-based spread rates. (from Anderson 1983, p.2)

B. Model Treatment of Fire Spread

The general elliptical or semi-elliptical shape assumes fire spread through uniform fuel beds in uniform weather. However, these conditions clearly are not met in actual wildfires. Even neglecting the certainty of inhomogeneity in the atmospheric conditions, spatial variations in the composition and slope of the fuel bed can produce highly complex fire front shapes. Methods of resolving this complexity in gridded computational models generally fall into two categories: vector-based and raster-based.

Vector-based models operate on the premise of maintaining the fire front as a contiguous entity spanning multiple grid cells. These models treat the fire as a polygon expanding outward from the ignition location. The method of calculating this expansion varies from one model to another. One popular method, used by FARSITE

(Finney, 1998), involves a conceptual variant of Huygen's principle for wave propagation through a medium; essentially, with the slope and fuel variations mapped to the grid, each ignited cell serves as a point source emanating its own elliptical or semi-elliptical burn perimeter based on local spread rate calculations. Therefore, the shape of the fire polygon at a future time is represented by a line circumscribing the perimeters emanating from the current vertices of the fire polygon. (See Fig. 3.)

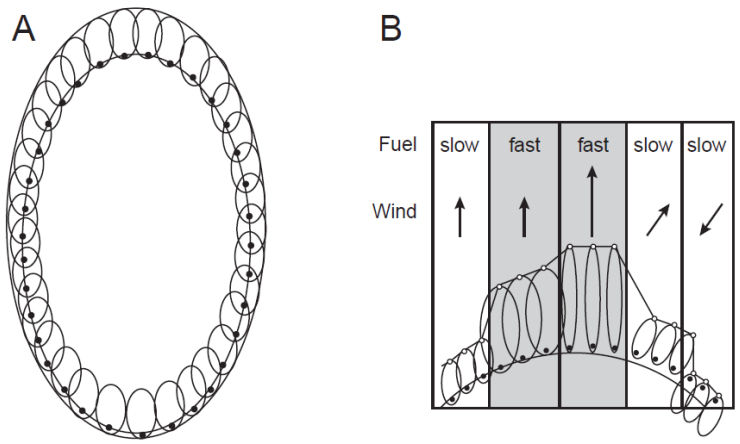

Figure 3: Illustration of Huygen's principle using elliptical wavelets to form a fire polygon. (A) Uniform conditions, with aggregate polygon proportional to individual wavelets. (B) Non-uniform conditions, with variation in wavelets producing a complex front shape. (from Finney, 1998, p. 3)

While this approach is both inexpensive and relatively simple to implement in both single-processor and MPI environments, numerical artifacts may arise due to the assumption of an elliptical fire spread shape as a basis. In an effort to mitigate or avoid such artifacts while maintaining parallelization capability, the Coupled Atmosphere-Wildland Fire Environment model (CAWFE; Clark et al., 2004) employs a "local contour advection" approach in which the spread rate within each cell is tracked using four tracer particles, each contrained to advance toward a specified corner of the cell

after it ignites based on the spread rate components obtained from the Rothermel formula. Once a tracer reaches its specified corner, it is "locked" in place; the fire polygon is then defined using the locations of the remaining ("free) tracers in the cells surrounding the burn area, which enables the evaluation of burned vs. unburned areas for a given cell as well as calculation of spread rate normal to the aggregated fire front. (See Fig. 4.) The method produces realistic fire front shapes and is readily parallelizable due to the localized treatment of the polygon's evolution; however, it is more expensive than the method used in FARSITE, due to more extensive calculations as well as the complex logic required to make the tracers behave realistically. (A similar method is used for the MesoNH-ForeFire model in Filippi et al., 2011.)

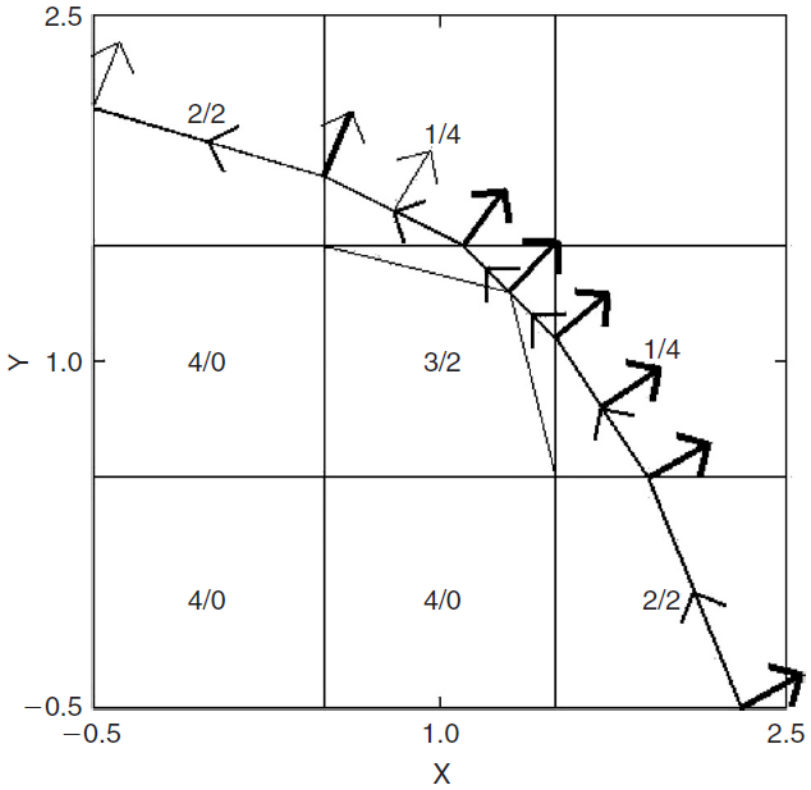

Figure 4: Use of subgrid-scale tracers to construct a fire polygon with associated normal spread vectors. The first number in each cell indicates the number of "locked" tracers, while the second number indicates the total degrees of freedom remaining for the "free" tracers. (from Clark et al., 2004, p. 52)

Another vector-based approach recently developed for use in the WRF-SFIRE model (Mandel et al., 2011) is expansion of the fire polygon using a level-set method. The method defines a level-set function $\psi(x,y,t)$ such that ψ is negative for burning cells and positive for unburned cells; thus, $\psi = 0$ marks the location of the fire front. After defining the initial values of the level-set function at the centers of the fire grid cells, the outside normal vector (i.e. the spread direction) is evaluated at the fire front as

$$\boldsymbol{n} = \frac{\nabla\psi}{\|\nabla\psi\|} \tag{11}$$

By use of the chain rule applied to the value of the level-set function on a point $\boldsymbol{x}$ moving with the fire front (which is zero by definition), the local rate of change of the level-set function is given by

$$\frac{\partial\psi}{\partial t} = -S\|\nabla\psi\| \tag{12}$$

where $S = \boldsymbol{n} \cdot \frac{\partial \boldsymbol{x}}{\partial t}$ is the spread rate obtained from the Rothermel formula. WRF-SFIRE uses central differences to evaluate the gradient of ψ and advances the function in time using a second-order Runge-Kutta method. After obtaining the updated ψ values at the centers of the cells in the fire grid, the new fire front shape is obtained by determining the new locus of points at which $\psi = 0$ using bilinear interpolation. While the logical difficulties associated with the tracer method used in CAWFE are avoided, this method is more expensive still.

Since the reduction of computational expense is paramount in obtaining useful forecasts, numerous efforts have been made to develop raster-based fire spread

prediction tools. In brief, the raster-based approach treats each cell in the fire grid as a discrete entity with a limited number of possible states (e.g. unburned, ignited/burning, smoldering, or burned-out). The main advantage of the raster-based approach over the vector-based approach is that the former is highly cost-effective; it can be implemented as a cellular automaton, with calculations only required on active (i.e. burning) cells and their immediate neighbors. The burn area is then represented as the superposition of the burn perimeters emanating from all of the active cells, in essence employing Huygen's principle as in FARSITE but without specifically defining the fire front as a contiguous entity.

However, numerous studies (e.g. Cui and Perera, 2008) have shown that this approach is prone to producing distorted or unrealistic wildfire shapes due to the fire spread being limited to directions connecting the center of the active cell with the centers of its immediate neighbors. Some improvement has been obtained by introducing an ellipse adjustment factor (as in the HFIRE model described by Peterson et al., 2009) or increasing the number of neighbor cells for which spread rates and directions are calculated as in the Boreal Forest Landscape Dynamics Simulator (BFOLDS) evaluated by Cui and Perera. However, their comparison of the vector-based Prometheus model (Tymstra et al., 2010), the 16-direction raster-based BFOLDS model, and the 8-direction raster-based Wildfire model (Todd, 1999) demonstrates that while the introduction of more spread directions improves the results of the raster-based approach, the potential for substantial distortion is still present, particularly at coarser resolutions. (See Fig. 5.) Furthermore, the discretized treatment of the fire spread is an

additional source of error when considering the fire and the atmosphere as a coupled system; this error source will be discussed later.

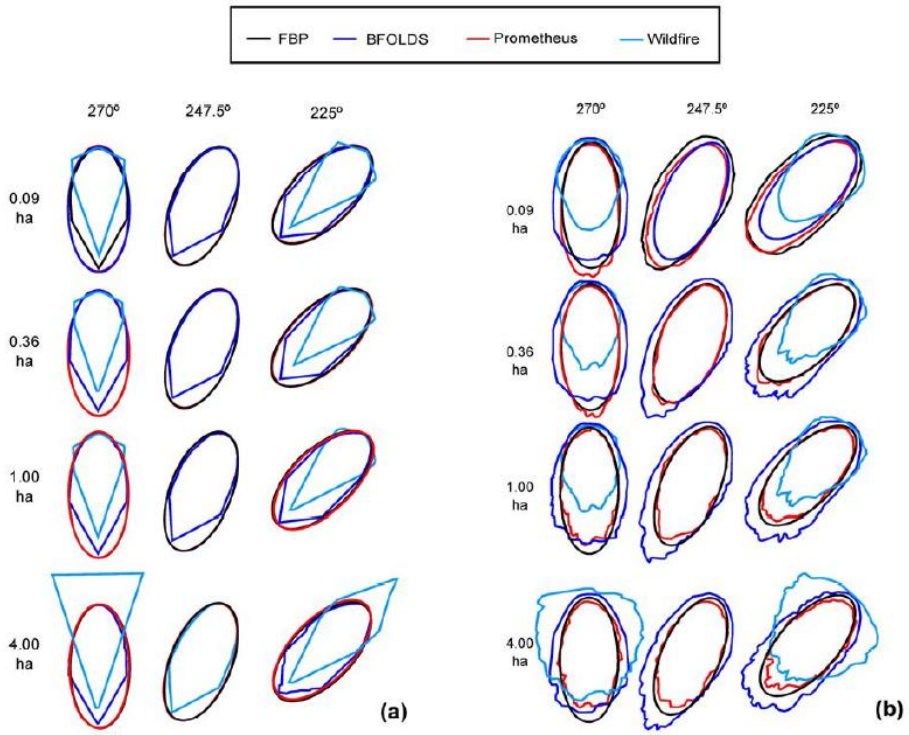

Figure 5: Comparison of burn areas from vector-based (red), 8-direction raster-based (light blue), and 16-direction raster-based (dark blue) fire spread models with expected results (black) for an idealized uniform fuel bed with constant winds (direction indicated at the top of each column). The grid resolution (hectares) is given at left. (a) fuel cells containing a fixed 50-50 mixture of spruce and aspen. (b) randomly-distributed cells containing spruce or aspen only, totaling 50% of the grid each. (from Cui and Perera 2008, p.8)

C. Atmosphere-Wildfire Feedbacks and Coupled Behavior

Current operational models generally rely on the observed ambient wind in their fire spread calculations. This is a serious shortcoming because it assumes that the ambient conditions are representative of the conditions in the immediate vicinity of the fire front. In many instances, the assumption may be justified; as discussed by Clark et

al. (1996a), a stronger background wind or a narrower fire front produces a shorter residence time for parcels traversing the region of intense heating, and a less intense fire front will not heat traversing parcels as much. Clark et al. reasoned that, when the additional buoyancy produced by heat from the fire is weak relative to the pre-existent kinetic energy of the traversing parcels, the wind within the fire will not deviate significantly from the background state and the use of the background wind in the fire spread computation is valid. (Such a case is often referred to as a "wind-driven" fire.)

However, in cases with more intense fire fronts and/or weaker winds (generally referred to as "plume-driven" fires), Clark et al. reasoned that the buoyancy of traversing parcels would be greatly increased and the wind in the vicinity of the fire would be substantially altered from the background state. To complicate matters, the Rothermel formula makes it clear that the initial alteration of the wind over the fire would in turn lead to alteration of the fire spread rate; this, in turn, would alter the rate of fuel consumption within the fire front, and hence the intensity of the fire front. Thus, in cases where the heat released by the fire would cause an increase in the wind speed over the fire front, a positive feedback would exist and the behavior of the fire front would become highly non-linear.

Therefore, Clark et al. argued that wildfire behavior should theoretically depend on the balance between the kinetic energy of the background wind and the buoyancy acquired by parcels traversing the fire front. They quantified this balance using a squared convective Froude number,

$$F_c^2 = \frac{\left(U - S_f\right)^2}{g\frac{\langle \Delta\theta \rangle}{\langle \bar{\theta} \rangle} W_f} \tag{13}$$

U is the wind speed across the fire front, S_f is the rate of spread, g is the acceleration due to gravity, $\Delta\theta/\bar{\theta}$ is the potential temperature anomaly (i.e. buoyancy) with brackets denoting a layer average over the region of intense heating (for which they gave an approximate value of 30 m), and W_f is the width of the fire front. By the above reasoning, a large value for F_c^2 would correspond to a "wind-driven" fire with little modification of the background winds in the vicinity of the fire front, while $F_c^2 \sim 1$ would mark the threshold of significant coupling between the atmosphere and the fire.

A widely-recognized sign of fire-atmosphere feedback is the center of the fire front developing a general parabolic or conical shape, along with more transient protrusions or "fingers." Clark et al. (1996a) distinguished between convective and dynamic contributions to these phenomena. The convective contribution consists of the development of plumes over the fire front which are tilted downstream by the ambient wind, thereby shifting the center of low-level convergence to a position ahead of the fire front. (See Fig. 6.) This would in turn strengthen the low-level wind across the fire front, enhance fire spread, intensify the plume, and produce an amplifying feedback loop as long as the low-level convergence zone remains close to the fire front.

For the dynamical forcing, Clark et al. (1996b) detailed the theoretical evolution of vorticity near the fire front. As shown in Fig. 7, the intense buoyancy gradient near the fire front produces horizontal vorticity in the ambient flow coming up from behind. When that vorticity encounters an along-line variation in vertical velocity, such as might arise due to enhanced spread rate and flame intensity from a convective feedback at the center of the fire front, it is tilted and stretched to produce a pair of "bookend"

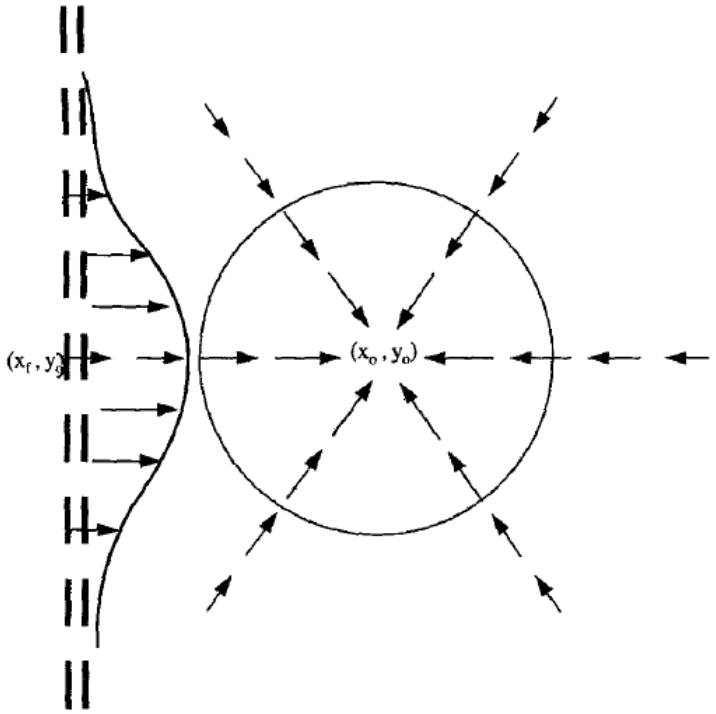

Figure 6: Idealized structure of the near-surface convergence pattern resulting from a fire-driven plume carried downstream by the background wind. (from Clark et al., 1996a, p. 883)

vertical vortices that act in concert to strengthen the wind traversing the fire front between them. As with the convective feedback, this process further enhances the spread rate and flame intensity, which amplifies the protrusion in the fire front as long as the vertical vorticity remains in phase with it instead of being swept downstream by overly-strong ambient winds.

In addition to theoretical discussion, Clark et al. (1996b) performed several tests of a primitive coupled model on an initially-straight fire front. In doing so, they noted that the simulated fire behavior often remained stable even when the convective Froude number indicated coupling (i.e. $F_c^2 \leq 1$) and asserted from this that other factors were required for coupled feedbacks to be realized. This view is supported by a survey

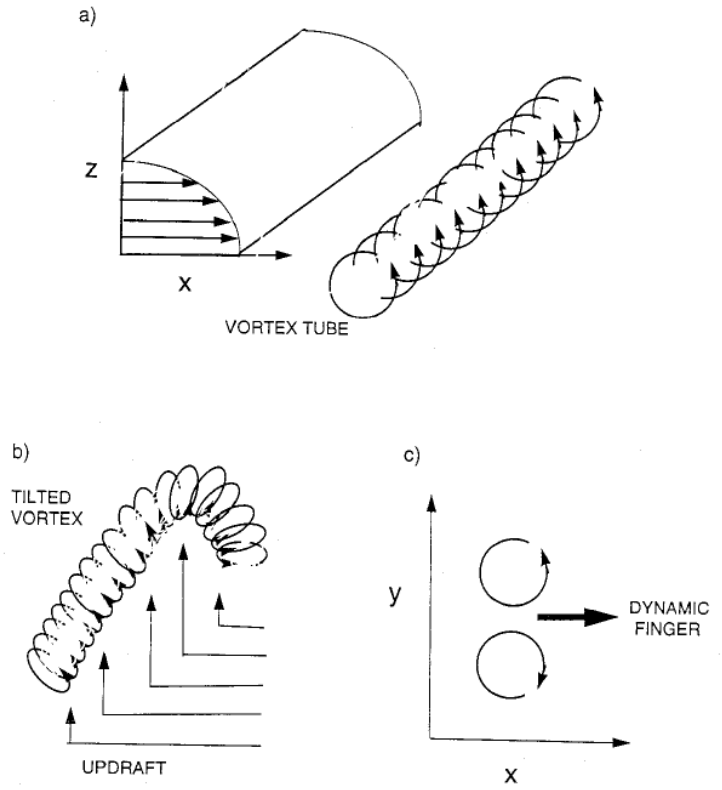

Figure 7: Role of tilting and stretching of fire-generated vorticity in the development of a dynamic "finger" in the front. (from Clark et al., 1996b, p. 179)

of controlled burns by Sullivan (2007), which indicates a lack of one-to-one correlation between the observed Froude number and the observed maximum spread rate or other fire behaviors indicative of coupling. On this basis, Sullivan concluded that the simple classification of wildfires as "plume-driven" or "wind-driven" is not appropriate.

Clark et al. (1996b) suspected that vertical wind shear is a key component of the feedback process, a suspicion bolstered by the lone instance of dynamic "finger" development in their test simulations. However, their discussion was limited to vertical shear in the first few decameters above the ground, arising from fire-induced downdrafts entering the combustion zone. A more intensive study of the impacts of the vertical wind profile was conducted by Kiefer et al. (2008). Using two-dimensional

ARPS simulations in which the fire position was represented by a localized, externally-forced surface sensible heat flux, Kiefer et al. illustrated the utility of negative vertical shear (i.e. winds across the fire front decreasing with height) in maintaining upright, more intense plumes with more potential for spread enhancement through the convective feedback discussed earlier.

Furthermore, Kiefer et al. demonstrated the possible role of shear instability in generating fire vortices and other extreme fire behavior. The growth of waves due to shear instability is contingent on the following condition being met for the Bulk Richardson number:

$$0 \leq \left[Ri_b = \frac{g(\Delta\bar{\theta})(\Delta z)}{\bar{\theta}(\Delta\bar{U})^2} \right] < 0.25 \quad (14)$$

$\Delta\bar{U}$ is the ambient vertical shear and $g(\Delta\bar{\theta})/\bar{\theta}$ is the environmental stratification over a layer with thickness Δz. Essentially, waves will grow in cases of weak stable stratification and strong shear, and if these waves reach the ground and interact constructively with the low-level dynamics near the fire front, extreme fire behavior can result. For example, the profile shown in Fig. 8 was taken on the morning of a prescribed burn in eastern Ontario that produced a large, intense vortex (McRae and Flannigan, 1990); a critical level containing a wind reversal is evident roughly 2 km AGL, which Kiefer et al. theorized to have contributed significantly to the intensification of the plumes responsible for the vortex.

To test this premise, Kiefer et al. performed an array of ARPS simulations with varying wind reversal heights, shear magnitudes, and boundary layer depths. The

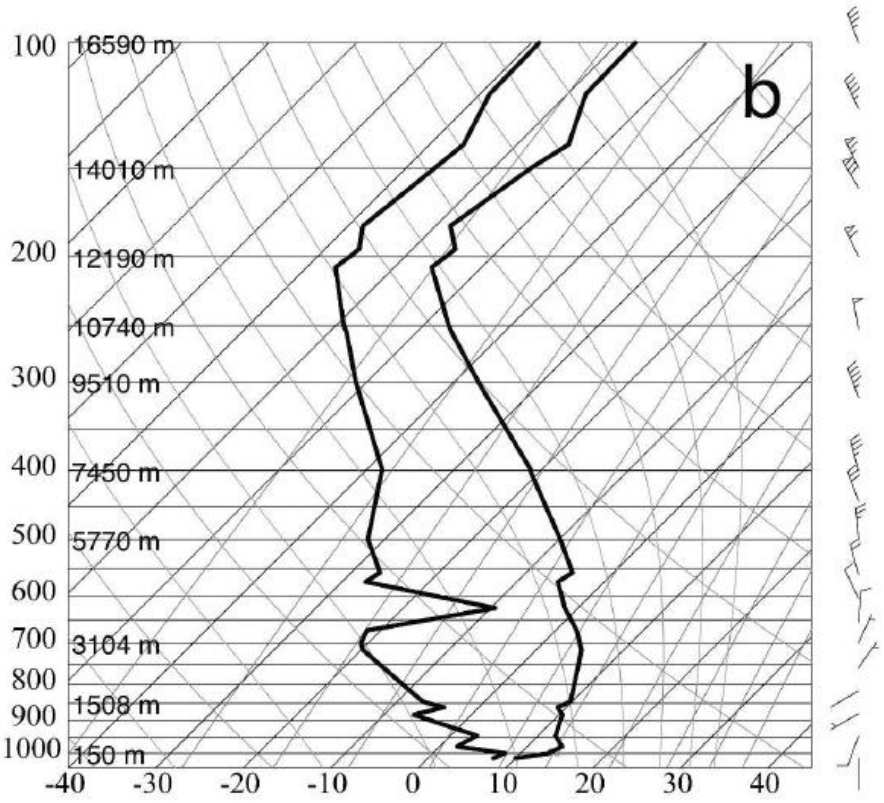

Figure 8: Observed sounding of temperature, dewpoint, and wind from Moosonee, ON, 1200 UTC 1 Aug 1987. (from Kiefer et al., 2008, p. 450)

results demonstrated that all three of these factors significantly influenced the intensity and structure of fire-generated plumes. In particular, the growth of Kelvin-Helmholtz waves from the wind reversal layer was crucial to the development of single intense plumes centered on the fire front as opposed to a string of smaller convective cells propagating downstream. (See Fig. 9.) While intensive examination of these convective structures is beyond the scope of the current research, these results serve as evidence of the need to consider evolving atmospheric conditions, not only near the ground extending beyond the top of the boundary layer, when seeking to predict fire behavior.

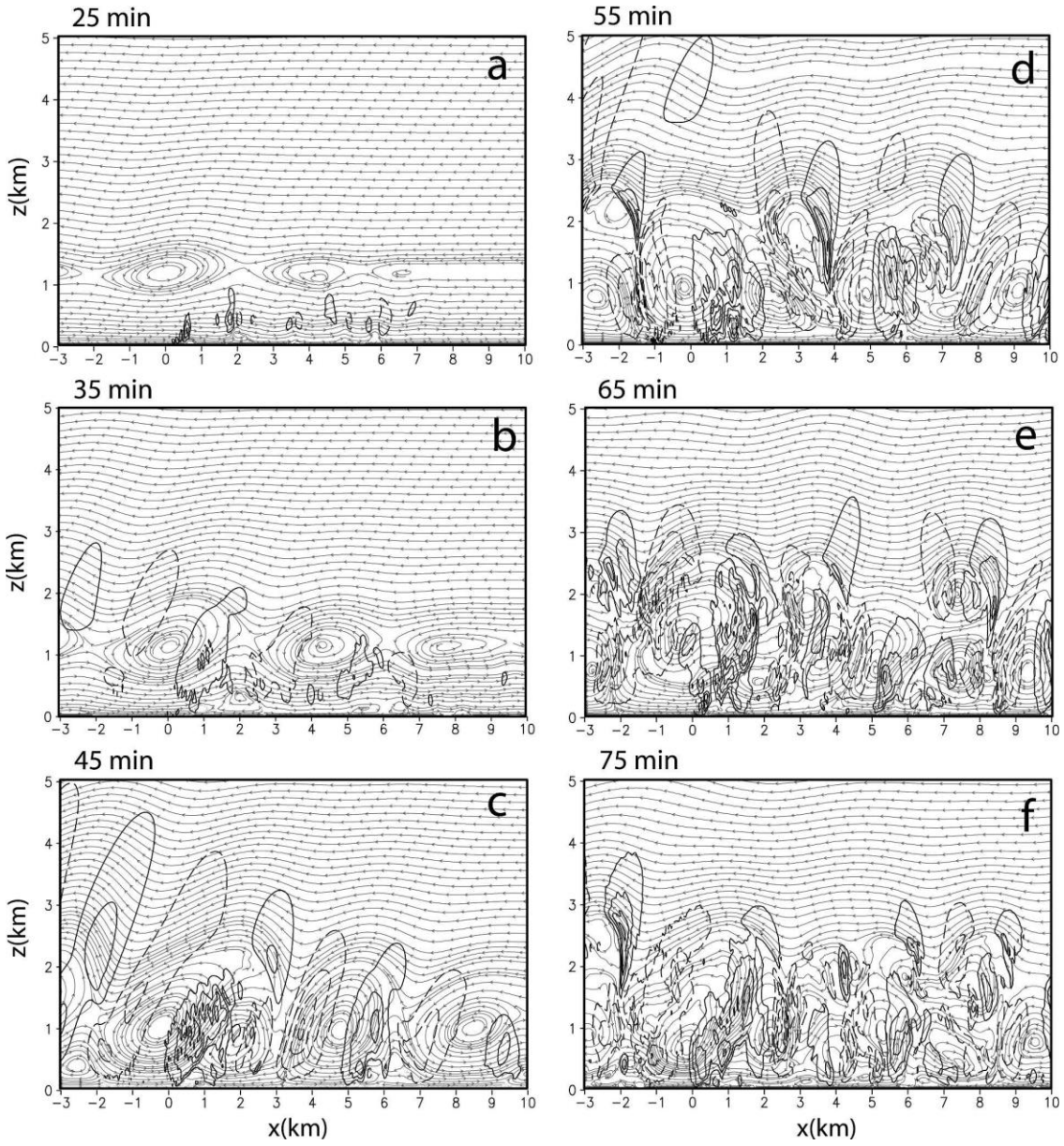

Figure 9: Development of an intense plume associated with an idealized two-dimensional fire front (located at x=0) due to the amplification of Kelvin-Helmhotz waves centered on a critical shear layer at an initial altitude of 1.2 km. (from Kiefer et al., 2008, p. 465)

D. Atmosphere-Wildfire Coupling Methods

Accurate representation of the heat released by the wildfire into the atmosphere is a key component of coupled modeling. The complexity of the heat release calculation

varies from one coupled model to the next. For example, along with its relatively intensive treatment of the combustion process (discussed previously), FIRETEC calculates the temperature of the burning fuel through an internal energy balance equation that accounts for the energy of combustion, evaporation, and radiative and convective heat exchange with adjacent gases. It couples with the HIGRAD fluid dynamics model (Smith et al., 2002) by using this temperature, the resolved low-level resolved velocity strain rates and mass conservation of the relevant gas species (accounting for production or removal in the combustion reaction as well as transport and diffusion) to calculate surface sensible, latent, and radiative fluxes as well as turbulent kinetic energy at multiple scales, which are then fed into HIGRAD. The benefit is that this model is completely self-determining (i.e. not reliant on experimentally-derived parameterizations that may not be valid in a given situation); unfortunately, it is also too computationally expensive to produce true forecasts. Therefore, the FIRETEC/HIGRAD model is generally limited to hypothetical examination or reanalysis of wildfire behavior (e.g. Cunningham and Linn, 2007).

As with fire spread, coupled models must currently rely on empirical relationships between heat flux and bulk fuel characteristics in order to run faster than real-time. Coupling is generally obtained by having the fire model calculate the heat sources and then inject them into the appropriate locations in the atmospheric model as lower boundary conditions. However, the method of approximating the heat sources varies. In MesoNH-ForeFire (Philippi et al., 2011), the fire model provides the atmospheric model with sensible and latent heat fluxes as well as an effective radiant temperature for the fuel, but the method is entirely empirical, with the fluxes and temperature for

each cell obtained through scaling of experimentally-derived "nominal" values according to the fractional burning area of the cell. For example, treating the surface as a blackbody and applying the Stefan-Boltzmann Law, the effective radiant temperature in MesoNH-ForeFire is given by

$$T_e = \sqrt[4]{(1 - R_b)T_s^4 + R_b T_n^4} \tag{15}$$

where R_b is the fractional burning area of the cell (ranging from 0.0 to 1.0), T_s is the background soil temperature of the cell, and T_n is the "nominal" burn temperature for the fuel type occupying the cell.

CAWFE (Clark et al., 2004) and WRF-SFIRE (Mandel et al., 2011) employ a semi-empirical algorithm that falls between the two previous examples; starting from a simplified energy conservation assumption in which the energy of the fuel combustion is entirely released into the atmosphere, these models estimate the time-averaged surface sensible and latent heat fluxes for a given cell in the fire model as

$$\phi_h = \frac{F(t-\Delta t)-F(t)}{\Delta t}\frac{1}{1+M_f} w_l h \tag{16}$$

$$\phi_q = \frac{F(t-\Delta t)-F(t)}{\Delta t}\frac{M_f+0.56}{1+M_f} w_l L \tag{17}$$

This formulation accounts for the latent heat content of both the moisture evaporated from the fuel and the additional water vapor created by the combustion reaction, which is estimated from (1) to be 56% of the initial dry fuel mass. This combined latent heat content is estimated for each fuel type and subtracted from the total heat of combustion of the dry fuel (~ 20 MJ kg^{-1}) to provide the "adjusted" heat content h (J kg^{-1}) used in

(16); thus, the calculated fluxes sum to the total energy released per unit time by the combustion reaction. $F(t)$ is the fraction of unburned fuel in the cell at time t, Δt is the time step interval (s), M_f is the fuel moisture fraction (dimensionless), w_l is the fuel load per unit surface area (kg m^{-2}), and L is the latent heat of vaporization for water.

For the unburned fuel fraction, CAWFE and WRF-SFIRE rely on a simplification of the BURNUP model described by Albini and Reinhardt (1995). Based on the approximation of a fuel element as a cylinder and equating the rate at which fuel mass is raised to its burning temperature to the combined heating rate from conduction, convection, and radiation from the immediate surroundings, Albini and Reinhardt expressed the fractional fuel mass loss over time as

$$\frac{M_0 - M(t)}{M_0} = 1 - \left(1 - \frac{t}{\tau_c}\right)^2 \quad (18)$$

where M_0 is the initial unburned fuel mass, $M(t)$ is the unburned fuel mass at time t, and τ_c is a decay coefficient determined through experimental burns. Rearranging terms and simplifying (possibly by treating the term in parenthesis as a first-order Taylor expansion, although this is not clarified in the literature), Clark et al. (2004) obtained exponential-decay fits to the experimental data for specific fuel types, such that the local unburned fuel fraction $f(t) = f(t)/M_0$ is now expressed as

$$f(t) = \exp\left(\frac{-t}{W}\right) \quad (19)$$

W is the e-folding time for the unburned fuel, i.e. the time required for it to be reduced to 36.9% of its original mass. (The approximate e-folding burn times for the standard

fuel types described in Anderson, 1982, are shown in the far right column of Table 1.) Thus, the evolution of the fuel bed is empirically-based, but the heat outputs used in the coupling process are theoretical derivations based on the experimental results.

This burn model applies only to an idealized, infinitesimal particle of fuel. However, CAWFE and WRF-SFIRE use fire grid resolutions on the order of 10 m. In order to evaluate the fractional fuel change averaged over a grid cell, the fractional ignited area of the cell must first be estimated based on the position of the fire polygon. In WRF-SFIRE, this is done by dividing the cell C into four sub-cells and interpolating the value of the level-set function to the corners $\boldsymbol{x}_k$ of each sub-cell. (See Fig. 10.) The fractional area β in each sub-cell is then estimated as

$$\beta \approx \frac{1}{2}\left(1 - \frac{\sum_{k=1}^{4} \psi(\boldsymbol{x_k})}{\sum_{k=1}^{4} |\psi(\boldsymbol{x_k})|}\right) \tag{20}$$

The unburned fuel fraction is then evaluated by computing the double integral

$$F(t) = \frac{1}{\text{area}(C)} \iint\limits_{\substack{\boldsymbol{x} \in C \\ \psi(x,t) \leq 0}} 1 - \exp\left(-\frac{t - t_i(\boldsymbol{x})}{W}\right) d\boldsymbol{x} \tag{21}$$

where $t_i(\boldsymbol{x})$ is the ignition time at location $\boldsymbol{x}$ within the cell. Setting $t_i = t$ for every point outside the fire polygon (i.e. every $\boldsymbol{x}$ for which $\psi(\boldsymbol{x}) > 0$) and assuming a roughly linear expansion of the polygon, WRF-SFIRE approximates this integral as

$$F(t) \approx \beta\left(1 - \exp\left(-\frac{1}{4}\sum_{k=1}^{4} \frac{t_i(\boldsymbol{x}_k) - t}{W}\right)\right) \tag{22}$$

According to Mandel et al., this approximation asymptotically approaches the true value of the integral for slow spread rates as the fractional area approximation β approaches the exact value.

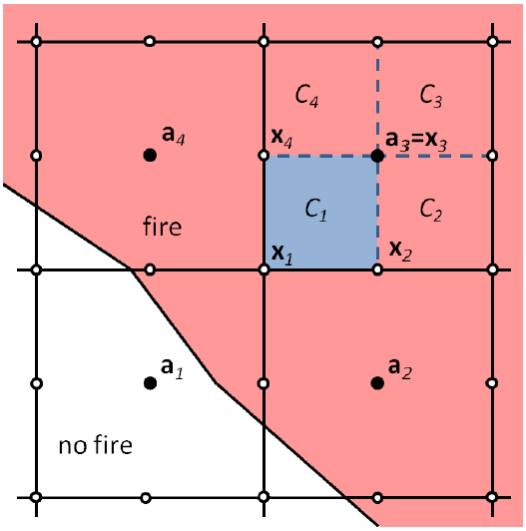

Figure 10: Division of fire mesh into subcells for fuel fraction calculation from interpolated level-set function values. (from Mandel et al., 2011, p. 597)

It should be noted that this method neglects the pre-heating and drying of the fuel ahead of the fire front, instead putting all of the energy from combustion into the atmosphere; essentially, the fuel moisture content is eliminated in proportion to (and at the same time as) the burning dry fuel. Furthermore, this method makes no explicit treatment of the fuel temperature or, consequently, the surface radiant flux. Instead, the atmospheric temperature is increased purely through the surface sensible heat flux represented by (16), and the presence of the radiant flux is treated tangentially by introducing a flux profile in which the sensible heat flux from the fire decays exponentially from its surface value with height. (It should also be noted that there is no defined method for obtaining the extinction depth of this profile, although the flame

length estimation method from Byram, 1959, has been suggested as a possibility; see Mandel et al., 2011.)

Finally, every one of these coupled models involves a vector-based fire spread methodology. A search of the literature fails to find a published instance of a raster-based fire spread model being coupled to an atmospheric model. This is not surprising; in simple qualitative terms, a raster-based fire model seems unappealing for coupling purposes due to its discretization of fire spread. Instead of a smoothly-varying perimeter such as one would find in a vector-based model, current raster-based methodologies are forced to ignite an entire cell all at once and inherently limit the number of directions the fire can spread.

Therefore, the utility of coupling such a fire spread model to an atmospheric model is uncertain. On the one hand, the error growth inherent in numerical weather prediction suggests that the error sources described above may have far-reaching impacts on the reliability of such a coupled model. On the other hand, such impacts have not previously been quantified, and the adaptability and efficiency of the raster-based approach provide motivation to investigate what those impacts may be and whether they can be mitigated or eliminated. That is the purpose of this study.

CHAPTER 3

EXPERIMENTAL DESIGN AND METHODS

A. The Advanced Regional Prediction System (ARPS)

ARPS is a nonhydrostatic three-dimensional numerical weather prediction model developed by the Center for Analysis and Prediction of Storms. The initial purpose was to model storm-scale phenomena, particularly those associated with intense convection. However, it has been expanded to handle atmospheric phenomena at a wide range of scales. Much of this expanded capability is outside the scope of the current topic; for a comprehensive overview, see Xue et al. (2000), Xue et. al. (2001) and Appendix A.

The initial emphasis on small-scale convection rooted in the boundary layer makes ARPS a prime candidate for coupling to a wildfire spread model. The fully-compressible momentum equations are solved for the perturbation mass and momentum variables (defined about a hydrostatic base state) using leapfrog-in-time-centered-in-space discretization, which maintains higher-order accuracy while avoiding an overly-stringent stability constraint on time step size. Acoustic waves are addressed using the mode-splitting method of Klemp and Wilhelmson (1978), which enables a numerically-stable treatment of fast wave modes without requiring expensive computation of slower processes (e.g. advection, diffusion) over small time steps. Furthermore, the vertical propagation of acoustic waves is addressed implicitly, which enables the model to run at very high vertical resolution (on the order of meters if desired) without being restricted to an impractically-small time step size to maintain compliance with the CFL criterion. Thus, the model is able to run faster than real-time

at high resolution without sacrificing accuracy (e.g. in the form of an anelastic approximation).

As noted in the previous chapter, the atmosphere-fire feedback process can extend several kilometers above the surface; thus, there is a lower limit on the average vertical resolution that may be employed in the atmospheric model while still obtaining timely results. However, as stated in Clark et al. (1996a), lack of vertical resolution near the surface artificially hinders heat transport due to smoothing of gradients and consequent under-estimation of flux divergence and advection. This in turn produces inflated temperatures immediately over the fire front, eventually resulting in destabilization and a "blowup" fire. Furthermore, the turbulence closure parameterizations available for this study (see Appendices A and C) are highly resolution-dependent in their determination of turbulence length scales and mixing coefficients.

Fortunately, ARPS offers a hyperbolic tangent function to stretch the grid vertically over a user-specified interval, which enables a high-resolution treatment of the near-surface feedbacks while affording a domain with sufficient vertical extent to capture the crucial processes higher up in the boundary layer. Furthermore, ARPS is suited for operation in complex terrain because it employs Jacobian transformations to produce a curvilinear grid that conforms to the local topography at lower levels. (See Fig. 11.) The geological survey data used to define the terrain for the ARPS grid are available at resolutions ranging from ~20 km down to 100m or less, which allows flexibility in specifying the horizontal resolution as well.

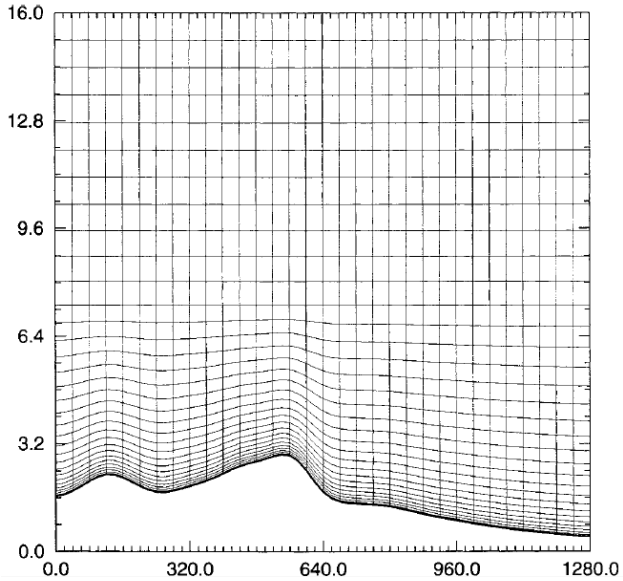

Figure 11: Illustration of an example terrain-following curvilinear grid with hyperbolic vertical stretching employed in ARPS. (from Xue et al., 2000, p.165)

To focus on microscale disturbances produced by wildfires, ARPS was generally run within the large-eddy simulation (LES) regime for this research; the horizontal resolution varied as described in section D of this chapter, but was typically on the order of 100 m, with a time step of 0.02 seconds specified to maintain numerical stability. The vertical resolution stretched from 4 m at the surface to an average grid spacing of 50-100 m aloft. 4^{th}-order flux-corrected transport (Zalesak, 1979) was used for advection of scalar quantities. Subgrid-scale turbulence was generally parameterized using the 1.5-order turbulence kinetic energy (TKE) closure scheme described by Moeng (1984) and Wyngaard and Brost (1984; hereafter the "Moeng and Wyngaard TKE scheme"). To reduce the amount of small-scale noise arising from sharp temperature gradients at the edges of the burn areas, 4^{th}-order monotonic computational mixing was specified with mixing coefficients generally increased by two orders of magnitude from the default ARPS values (i.e. variables cfcm4h and

cfcm4v were set to 0.05 in the ARPS NAMELIST files). Any deviations from these settings are noted in section D.

Wildfires substantially increase the amount of water vapor in the atmosphere, both by evaporating fuel moisture and by producing additional water in the hydrocarbon combustion reaction shown in (1). While condensation was not expected for any of the cases presented here due to exceptionally dry conditions throughout the troposphere, correct specification of model microphysics was still crucial; in early tests employing only a saturation adjustment or the warm-rain microphysics scheme formulized by Kessler (1969), spurious development of cloud water immediately above the fire location resulted in runaway latent heating and model failure within the first few time steps. (It is speculated that the error resulted from the model temperature exceeding the range of the lookup table used to calculate the latent heat of evaporation for simple saturation adjustment in ARPS, although a detailed examination was deemed outside the scope of this work.) Use of the 5-species (two liquid, three ice) microphysics scheme developed by Lin et al. (1983) averted this problem, possibly due to the iterative relaxation technique used to maintain energy balance.

As a stand-alone model, ARPS has been extensively verified against both theoretical solutions and observational data, and it is currently used to model atmospheric phenomena ranging from isolated convection (e.g. Xue et al., 2001) to stratospheric gravity waves over Greenland (Limpasuvan et al., 2006). However, in order to be coupled to a fire model, ARPS required additional modifications. Those modifications are described in section C of this chapter.

B. The Discrete-Event Specification Fire Spread Model (DEVS-FIRE)

DEVS-FIRE is being developed as a joint effort between the Texas A&M Department of Industrial and Systems Engineering and the Georgia State University Department of Computer Science. (Ntaimo et al., 2008) It is intended to provide a platform integrating wildfire spread prediction and containment resource optimization, with the eventual goal of serving as an operational decision-making tool for firefighting and emergency response personnel. The current system envisions an interface passing information on the predicted fire spread to a stochastic resource optimization model, which then simulates the impact of containment procedures on the fuel bed (e.g. establishment of firebreaks) and passes them back to the fire spread model. (See Fig. 12.) However, the optimization model is still under development and played no role in this research.

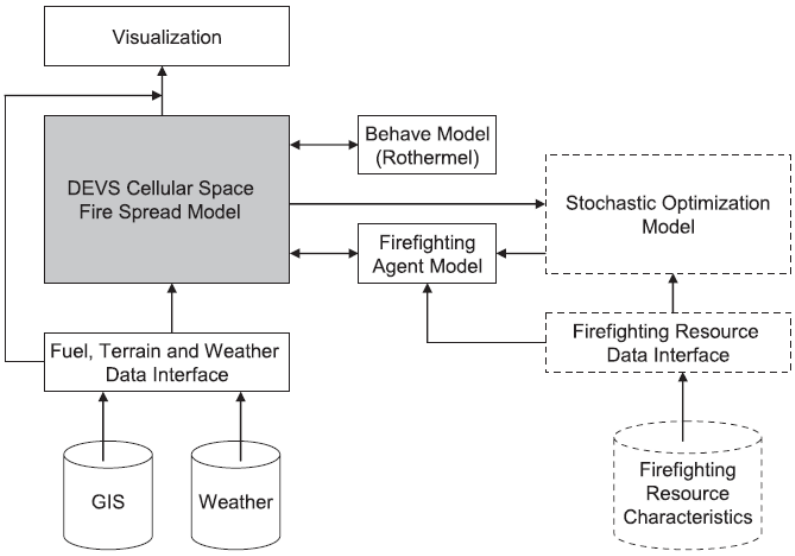

Figure 12: DEVS-FIRE system architecture. (from Ntaimo et al., 2008, p. 140)

Most dynamic modeling applications (including ARPS) are based on time discretization, i.e. updating the model state based on discrete time steps. The discrete event specification (DEVS) used in DEVS-FIRE reverses this perspective, updating the model time based on changes in the model state, as described by Ziegler (1976). In addition to potentially avoiding truncation error associated with time discretization, this method is ideally suited for raster-based fire spread modeling because each individual cell in the raster can be designated as an "agent" with a very limited number of possible states. When combined with a dynamic structure cell space model in which only "active" (i.e. burning or smoldering) cells are included while "passive" (unburned, burned-out, or non-flammable) cells are removed, the DEVS formalization is an extremely efficient option.

DEVS-FIRE starts from a user-specified set of ignition cells and predicts fire spread based on the Rothermel formulas and Huygen's principle. Specifically, the agent corresponding to each active cell computes its own maximum spread rate and direction based on the wind speed, wind direction, slope, terrain aspect, and fuel bed characteristics using the Rothermel equations described in Chapter 2. An ellipse is fitted to this spread rate and direction based on the empirical relations given in Anderson (1983); the ellipse is subsequently decomposed to find the spread rate in the directions of each of the cell's eight neighbors as shown in Fig. 13. Based on imported changes in wind speed and direction, the agent updates these spread rates and the expected time of the next change in state, i.e. the ignition of a neighbor cell. When that time is reached, the agent sends a message igniting the neighbor cell (unless its moisture content is above the extinction value given in Table 1) and the process repeats.

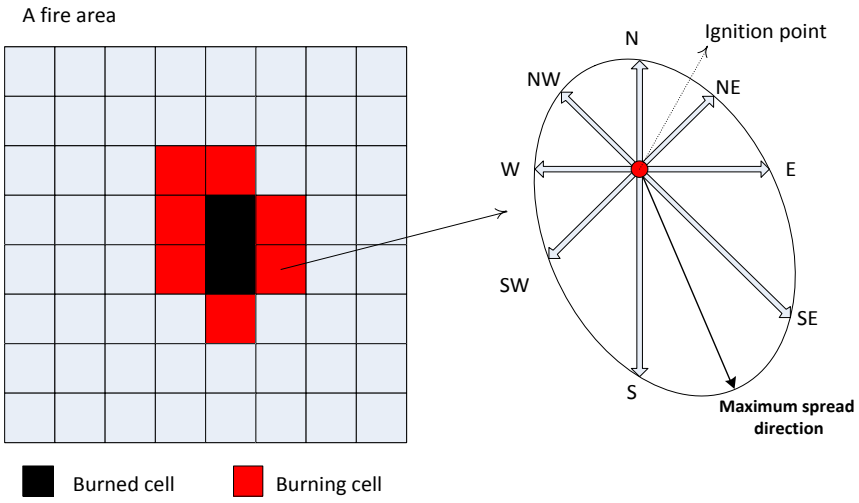

Figure 13: Example calculation of neighbor spread rates for DEVS-FIRE cells burning on flat terrain in north-northwesterly wind. (courtesy of Haidong Xue)

The question of fire model validation is complicated by uncertainties regarding the actual composition and moisture content of the fuel bed as well as a general dearth of detailed observations of the evolving wildland fire spread rate and burn area dimensions over time. Therefore, the initial validation of the uncoupled DEVS-FIRE model (Gu et al., 2008) relied on comparison of idealized test results with those produced by previously-validated models like FARSITE. The initial test consisted of both models predicting fire spread from a single ignition point in uniform weather and fuel conditions for 10 hours. As shown in Fig. 14, while the extent of the spread in the eight "neighbor" directions in DEVS-FIRE matches the dimensions of the FARSITE ellipse, the distorting effect of the raster grid is evident after 10 hours in the unnaturally angular perimeter as well as underprediction of the total burn area.

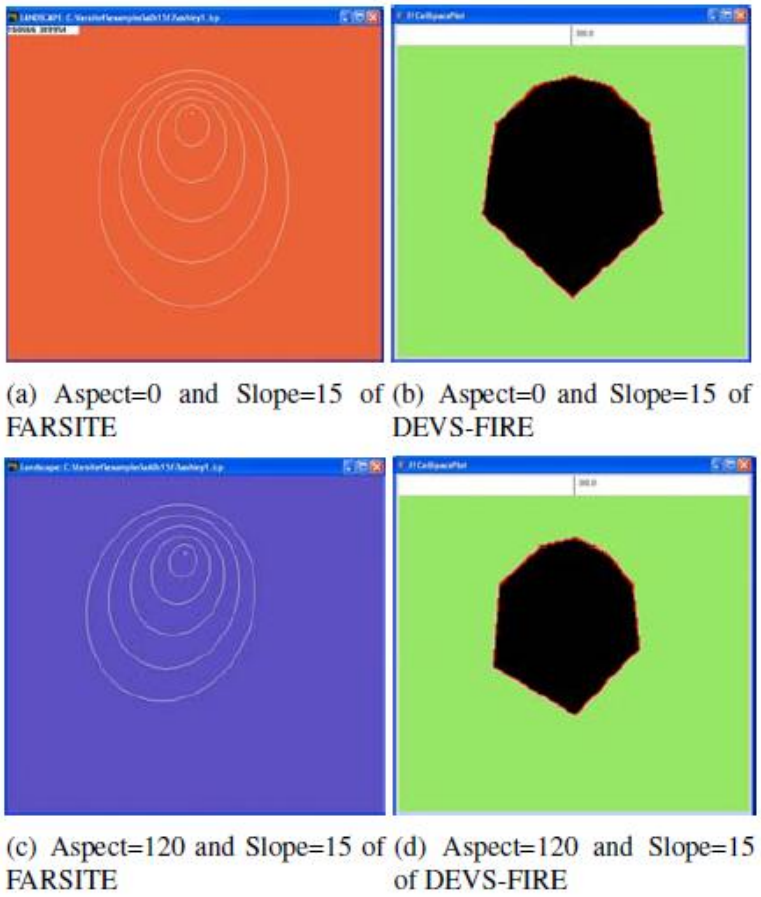

(a) Aspect=0 and Slope=15 of FARSITE

(b) Aspect=0 and Slope=15 of DEVS-FIRE

(c) Aspect=120 and Slope=15 of FARSITE

(d) Aspect=120 and Slope=15 of DEVS-FIRE

Figure 14: 10 –hour burn areas for FARSITE (left, outermost white contours) and DEVS-FIRE (right, black regions) for uniform fuel bed, northerly 5 m/s wind, and terrain aspect of 0° (top) and 120° (bottom). (from Gu et al., 2008, p. 358.)

However, DEVS-FIRE performed better in non-uniform conditions. A subsequent test split the fire grid into three uniform regions: a northern region of tall grass with a 15° slope facing north; a central region of dormant brush and hardwood slash on level terrain; and a southern region of timber with a 15° slope facing south. In other words, the domain was centered on a ridgeline oriented east-to-west, with progressively slower-burning fuel to the south. As shown in Fig. 15, the resulting DEVS-FIRE and FARSITE burn areas were quite comparable, a fact confirmed by the

burn area and perimeter data listed in Table 2. When heterogeneous fuel and terrain derived from actual GIS data were used in conjunction with time-varying winds as shown in Fig. 16, the DEVS-FIRE and FARSITE burn areas also matched closely. This suggests that the complexity of fuel and terrain and the rapidly-evolving atmospheric conditions that exist for real-life wildfires may help mitigate the theoretical deficiencies of a raster-based model, lending support to the idea of using such a model in coupled fire spread forecasting.

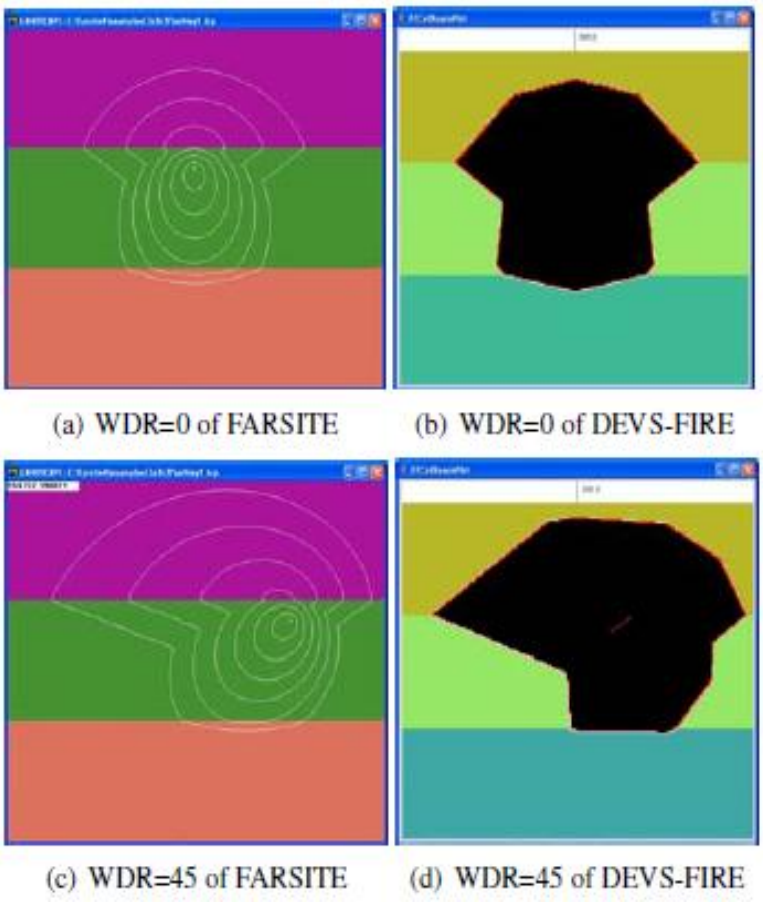

Figure 15: As in Fig. 14, but fuel and slope vary by color in uniform 5 m/s northerly (top) and northeasterly (bottom) winds. (from Gu et al. 2008, p. 359)

Table 2: Comparison of DEVS-FIRE and FARSITE idealized, non-uniform test results (from Gu et al., 2008, Table 4)

Wind Dir			T + 5 hrs	T + 6 hrs	T + 7 hrs	T + 8 hrs	T + 9 hrs
0	Perimeter (km)	FARSITE	4.4	5.8	7.5	9.3	11.2
		DEVS-FIRE	5.4	6.8	8.2	9.6	11.1
	Area (ha)	FARSITE	147.9	238.1	373.7	555.6	788.7
		DEVS-FIRE	174.8	278.2	408.9	561.3	739.5
45	Perimeter (km)	FARSITE	4.9	6.8	9.1	11.5	14.0
		DEVS-FIRE	5.6	7.9	10.1	12.2	14.2
	Area (ha)	FARSITE	164.9	296.3	507.8	804.9	1174.2
		DEVS-FIRE	229.1	387.5	599.4	864.1	1159.7

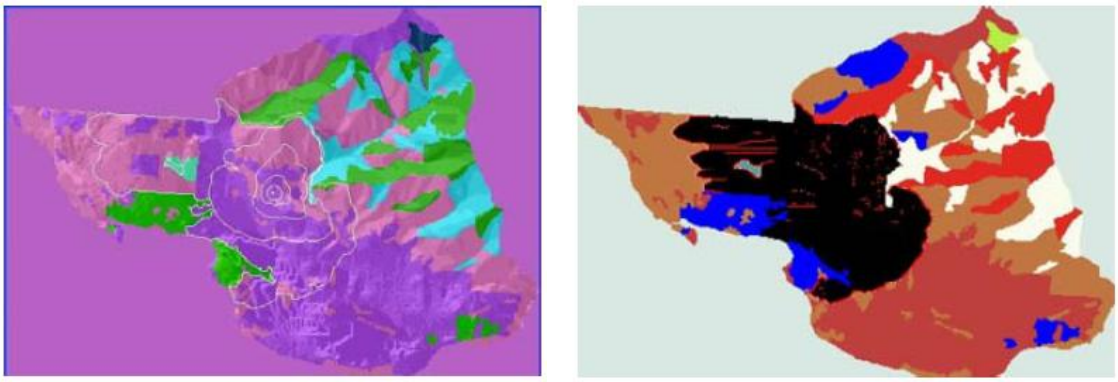

(a) FARSITE (b) DEVS-FIRE

Figure 16: Comparison of 10-hour burn areas for FARSITE (left, outermost white contour) and DEVS-FIRE (right, black area) using actual GIS terrain (shading) and fuel (color fields) data. (from Gu et al., 2008, p. 360)

C. Coupling ARPS to DEVS-FIRE

i. Geolocation and grid mapping

The coupled models previously described combine the fire model and the atmospheric model together as two facets of an integrated program, with the fire model and its corresponding grid treated embedded within the weather model and its corresponding grid. In this framework, coupling is achieved purely through internal

data exchange. However, this was not possible in this research because ARPS is programmed in Fortran and must be parallelized whereas DEVS-FIRE is programmed solely in Java and is not yet equipped to operate in MPI mode.

Therefore, a method of grid mapping and external data exchange was developed to couple ARPS to DEVS-FIRE. First, the wildfire could not be allowed to spread to the lateral boundaries of the ARPS grid, since the resulting clash between the local conditions produced by the fire and the lateral boundary conditions imposed on ARPS would produce rapidly-accumulating numerical instability and model failure. Therefore, the first step was to ascertain the geographic extent of the fire grid and select an ARPS domain that would fully contain it. (Failure to completely contain the fire grid within the weather grid triggered an error message and immediate abort.) Furthermore, for the experiments described here, the ARPS domain surrounded the fire grid with a "buffer zone" at least 0.5 km wide in an effort to allow any upstream-propagating fire-induced disturbances to smooth out at least partially before encountering the ARPS lateral boundaries behind the fire front.

Properly mapping one grid onto the other required the geographic coordinates of a common "anchor" point. In the idealized experiments described here, this was accomplished simply by collocating the center points of both grids. For the experiments using real data, the latitude and longitude of the southeastern-most cell in the DEVS-FIRE grid were mapped to the ARPS grid; the rest of the DEVS-FIRE grid was mapped within the ARPS domain using the pre-defined horizontal resolutions of both models and the assumption that the axes of both domains were oriented along lines of constant latitude and longitude. Since the wildfire and associated local feedbacks

were assumed to occur over a fairly small geographic area (~10 km^2 for large fires), possible distortions due to differences in map projection between the ARPS grid and DEVS-FIRE grid were ignored.

ii. Data transfer procedure

Because the state in ARPS is too complex to advance using discrete event specification, the coupled model was structured to advance over a series of discrete time updates. Each of these updates entailed the transfer of heat release data from DEVS-FIRE to ARPS as well as the transfer of low-level weather conditions from ARPS to DEVS-FIRE. However, selection of the time interval between updates was subject to practical considerations: while internally-coupled models like WRF-SFIRE are able to update at every weather model time step (on the order of a tenth of a second or less when operating at high spatial resolutions) without significant extraneous cost, the current version of ARPS/DEVS-FIRE is forced to couple externally. Therefore, each update requires external files to be written and read by both models, a process that greatly reduces the speed of the coupled model as the update interval is reduced. Accordingly, the significance of the truncation error introduced by an increased update interval became a topic of study, and the update interval was designed as an arbitrary value specified by the user prior to initialization.

One dilemma of coupling the separate systems together stems from the fact that a truly coupled process happens in both systems simultaneously, whereas time-discretized explicit numerical coupling requires one model to precede the other. In essence, for an update interval Δt, the state of Model A at time t is used to advance

Model B from time t to time $t+\Delta t$, and then the updated state of Model B is used to advance Model A from t to $t+\Delta t$. The question therefore concerns which model would respond less severely to the expected difference between the states of the other model at t and $t+\Delta t$; in other words, the model that is expected to be less affected by a feedback time lag of Δt should be designated as Model A. Since the DEVS-FIRE state was expected to be more robust to changes in the ARPS state than vice versa, and since the update interval must be an integer multiple of the time step used in ARPS, advancing the coupled model in time was accomplished as shown in Fig. 17.

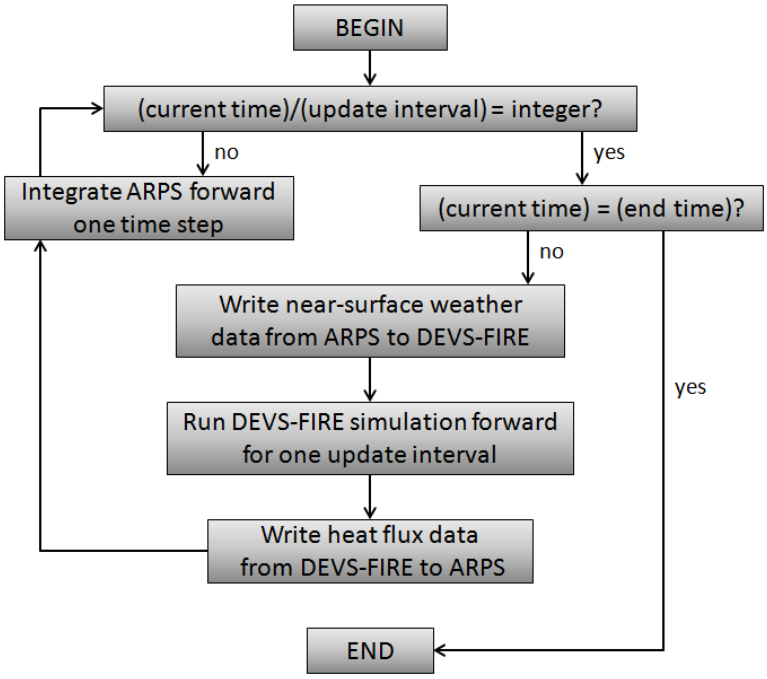

Figure 17: Time integration algorithm for ARPS/DEVS-FIRE coupled model

With its parallelization capability, ARPS was tasked with mapping the pertinent data from each model to the grid used by the other. Since simulating fire spread is less expensive, and since the accuracy of the raster-based approach is particularly dependent on grid resolution (see Cui and Perera, 2008), the ARPS grid was generally coarser than

the DEVS-FIRE grid, with multiple DEVS-FIRE cells contained within a single ARPS cell. Therefore, in order to ensure conservation of energy, heat from DEVS-FIRE was transferred to the ARPS grid through simple spatial averaging; the "representative" heat flux value for an ARPS grid cell of resolution Δx was the mean of the heat flux produced by all DEVS-FIRE cells with centers located within a zonal and/or meridional distance $\Delta x/2$ from the center of the ARPS cell. Meanwhile, bilinear interpolation was used to map the temperature, relative humidity, and 6m AGL u and v wind components (which were then combined to calculate interpolated wind speed and direction) from the respective locations on the ARPS Arakawa-C grid to the centers of the cells in DEVS-FIRE grid. (See Fig. 18.)

It should be noted that the current version of DEVS-FIRE does not have a method of evolving fuel moisture or heat content in unburned cells over time; therefore, the only updated weather data that were factored into the DEVS-FIRE calculations for these experiments were the 6 m AGL wind speed and direction in and immediately around the burn area. It should further be noted that the 6m wind altitude was designated because of existing, widely-used empirical relationships estimating the "effective" fire model wind speed from the 6 m AGL wind speed using a fuel-type-dependent wind adjustment factor (Andrews, 2012). In order to avoid errors from vertical interpolation of the horizontal wind components (since a log wind profile predicted by similarity theory was not expected to apply near the fire front), the ARPS grid dimensions were specifically chosen to ensure that the desired altitude corresponded exactly to the center of a grid cell for each vertical column in the domain.

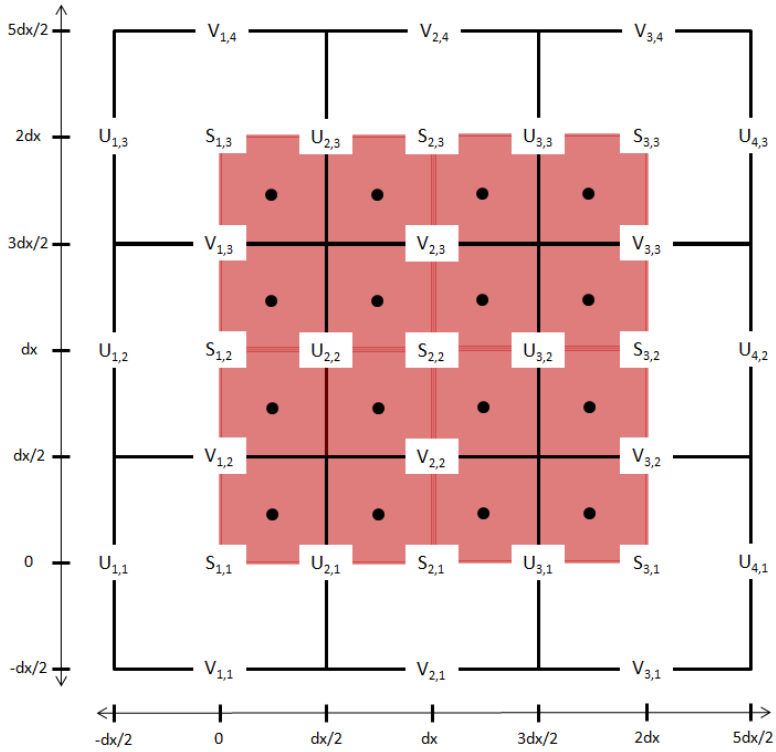

Figure 18: Model grid map for a 4x4 DEVS-FIRE grid of resolution dx/2 centered within a 3x3 ARPS domain of resolution dx. *U*, *V*, and *S* denote the computational locations for *u* wind components, *v* wind components, and scalar quantities (e.g. temperature and dewpoint) respectively for the Arakawa-C grid used by ARPS. Subscripts denote the *x* and *y* indices of the ARPS cells, while each DEVS-FIRE cell is represented as a pink box with a dot at its center.

iii. Calculating heat output from DEVS-FIRE

The heat released by fuel combustion as a function of time is not explicitly treated in the uncoupled version of DEVS-FIRE. It is not needed there because, from the Rothermel formula given in (10), the only aspect of the combustion that affects the uncoupled spread of the fire is the reaction intensity *at the fire front*, which is an instantaneous value determined by the terrain, local wind, and characteristics of the fuel bed. Therefore, it was necessary to select a method for estimating the temporal

evolution of the heat output for each ignited cell in order to provide sufficient input to represent the burn area appropriately in ARPS.

As stated in Chapter 2, experimentally-derived functions are used to estimate different aspects of the heat release in other coupled models. For example, as shown by (19), the change in unburned fuel fraction is modeled in WRF-SFIRE as a simple exponential decay adapted from the BURNUP model (Albini and Reinhardt, 1995), with the e-folding time determined entirely by the fuel type. Recognizing that the combustion rate should be substantially increased by stronger winds (due to an enhanced supply of fresh oxygen in the combustion zone), the initial intent for ARPS/DEVS-FIRE was to use the full version of the BURNUP model to calculate the fuel loss and associated energy fluxes. From Albini and Reinhardt (1995), the time scale for the mass loss used in (16) may be given by

$$\tau_c = \frac{T_F' - T_C'}{T_F - T_C} \frac{\rho_0}{\rho_o'} \frac{D(0)}{h_{eff}} (a' + b'M) \tag{23}$$

T_F is the "fire environment temperature" (a function of burn intensity), T_C is the peak pyrolysis temperature of the fuel, ρ_0 is the ovendry density of the fuel, $D(0)$ is the initial diameter of the fuel elements, M is the fuel moisture content, and T_F', T_C', ρ_0', a', and b' are scale values determined from experiments. From Eqns. 2 through 5 in Albini and Reinhardt , the effective heat transfer coefficient h_{eff} is given by

$$h_{eff} = \left[\frac{0.344 k_a}{\nu^{0.56} D^{0.44}} (T_F^3 + T_F^2 T_s + T_F T_s^2 + T_s^3) \right] V^{0.56} \tag{24}$$

k_a and v are the thermal conductivity and kinematic viscosity of hot air (respectively), T_s is the surface air temperature, and V is the wind speed over the fuel elements. Thus, a faster wind speed would produce a higher value for h_{eff}, meaning a lower value for the fuel loss time scale, faster combustion, and more intense heat release.

Unfortunately, this method could not be implemented due to difficulties in obtaining a good rule for approximating T_F and v (which has a strong temperature dependence). Furthermore, the values for *a'* and *b'* are only available for a few selected (primarily woody) fuel types. Therefore, it became necessary to ignore the impact of wind on local combustion rate and instead use the same exponential fuel decay model employed in WRF-SFIRE, described by (19). Since the initial ("fully-discrete") version of DEVS-FIRE ignites an entire grid cell at once, the local unburned fuel fraction *f(t)* and the integrated fuel fraction for the cell *F(t)* are equal. Thus, for a cell ignition time t_i,

$$F(t) = \begin{cases} 1, & t < t_i \\ \exp\left(\frac{t_i - t}{W}\right), & t \geq t_i \end{cases} \quad (25)$$

The time-averaged sensible and latent heat fluxes valid at time t are found by solving for F at t and $t - \Delta t$ and using the results in (16) and (17).

Here, the impact of full discretization on the coupled model becomes even more uncertain. At the limit of infinitesimal grid resolution, the fully-discrete ignition of entire grid cells would converge to the "true" solution (assuming the exponential decay function is an accurate representation of the fuel combustion). However, at computationally-feasible resolutions (~10 m), there is a delay between the immediate

ignition of a "parent" cell and the immediate ignition of its neighbors. Thus, there is a discontinuous increase in heating when the parent cell ignites, a lull period in which the heat release in the parent cell decreases rapidly, and then another discontinuous increase when a neighbor cell ignites. This produces a series of "spikes" in the spatially-averaged heat flux received by ARPS, which increase in size and decrease in duration for faster-burning fuels.

For a given pairing of ARPS and DEVS-FIRE grids, there are two obvious options for combating the heat flux discontinuity. The first is simply to increase the amount of temporal smoothing by lengthening the update interval Δt. However, this risks additional truncation error, particularly when the coupling between the fire and the atmosphere is strong and feedbacks operating on time scales smaller than Δt contribute significantly to the overall fire spread.

The second option is to incorporate an aspect of the polygon-based method into the raster treatment of the fire by estimating the progress of the fire front within the cell and applying an integral similar to the one in (21) for the unburned fuel fraction $F(t)$. Since this approach treats the fire spread as a continuous process within the cell while maintaining a discrete approach for spreading the fire from one cell to another, it is hereafter referred to as the "quasi-discrete" heat release model. For DEVS-FIRE, this approach requires the "parent" cell to relay its relative position (and, hence, the effective direction θ of fire spread) to a neighbor cell at the time the latter ignites. The effective spread rate R is in the direction θ is then calculated by the neighbor cell using the elliptical decomposition shown in Fig. 13. If this rate is assumed constant over time

within the cell, the ignition time $t_i(\boldsymbol{x})$ at a location $\boldsymbol{x} = x\boldsymbol{i} + y\boldsymbol{j}$ within the cell (with the origin $\boldsymbol{x_o}$ taken to be the side or corner bordering the "parent" cell) is

$$t_i(\boldsymbol{x}) = t_i(\boldsymbol{x_o}) + \frac{x\cos\theta}{R} + \frac{y\sin\theta}{R} \tag{26}$$

where $t_i(\boldsymbol{x_o})$ is the time the neighbor cell ignites in the fire spread model. Substituting (26) for t_i in (21) and applying over the entire grid cell (i.e. Area(C) = $(\Delta x)^2$) gives

$$F(t) = 1 - \frac{1}{(\Delta x)^2}\iint_B 1 - \exp\left(\frac{t_i(\boldsymbol{x_o}) + \frac{x\cos\theta}{R} + \frac{y\sin\theta}{R} - t}{W}\right) dx\, dy \tag{27}$$

B is the burning portion of the cell, i.e. the set of all points $\boldsymbol{x}$ for which $t_i(\boldsymbol{x}) > 0$. In DEVS-FIRE, the spread direction is limited to either $\theta = 0$ ("straight") or $\theta = \pi/4$ ("diagonal"). The integral transitions from a "growing" phase (with the limits expanding as the fire front moves through the cell) to a "static" phase after the fire front leaves the cell. For "straight" spread, the transition occurs at elapsed time $t_f = \Delta x/R$. For "diagonal" spread, it occurs at $t_f = \Delta x\sqrt{2}/R$. Moreover, for "diagonal" spread, the geometry of the cell is a factor, since the shape of the burn area transitions from triangular to pentagonal at time $t_c = \Delta x/R\sqrt{2}$. The advantage of the exponential decay function in this instance is that it is easily separable (in terms of the independent variables) and the solution is straightforward once the dimensions of B are obtained as functions of time. Defining the time since ignition as $t_e = t - t_i(\boldsymbol{x_o})$, the final solution set for "straight" fire spread is as follows:

$$F(t_e) = \begin{cases} 1, & t_e < 0 \\ 1 + \left(\frac{R\,W}{\Delta x}\right)\left[1 - \frac{t_e}{W} - \exp\left(\frac{-t_e}{W}\right)\right], & 0 \le t_e < t_f \\ \left(\frac{R\,W}{\Delta x}\right)\exp\left(\frac{-t_e}{W}\right)\left[\exp\left(\frac{\Delta x}{R}\right) - 1\right], & t_e \ge t_f \end{cases} \quad (28)$$

For "diagonal" spread, the solution involves four cases instead of three:

$$F(t_e) = \begin{cases} 1, & t_e < 0 \\ 1 - \left(\frac{R t_e}{\Delta x}\right)^2 + 2\left(\frac{R\,W}{\Delta x}\right)^2\left[\frac{t_e}{W} + \exp\left(\frac{-t_e}{W}\right) - 1\right], & 0 \le t_e < t_c \\ \left(\frac{R t_e}{\Delta x} - \sqrt{2}\right)^2 + 2\left(\frac{R\,W}{\Delta x}\right)^2\left[1 + \frac{\frac{\Delta x\sqrt{2}}{R} - t_e}{W} + \left[\exp\left(\frac{-t_e}{W}\right)\right]\left[1 - 2\exp\left(\frac{\Delta x}{R\,W\sqrt{2}}\right)\right]\right], & t_c \le t_e < t_f \\ 2\left(\frac{R\,W}{\Delta x}\right)^2 \exp\left(\frac{-t_e}{W}\right)\left[1 + \exp\left(\frac{\Delta x\sqrt{2}}{R\,W}\right) - 2\exp\left(\frac{\Delta x}{R\,W\sqrt{2}}\right)\right], & t_e \ge t_f \end{cases} \quad (29)$$

For an initial cell (i.e. a cell representing the fire front at model initialization), the treatment is augmented slightly. Theoretically, the fire should start at the center of this cell and spread outward in all directions. However, since the above derivation treats the spread of the fire front as edge-to-edge, this would incur an artificial delay of $\Delta x/2R$ ("straight" spread) or $\Delta x/R\sqrt{2}$ ("diagonal" spread) in the heat release of a neighbor cell, relative to its theoretical beginning time. Furthermore, determining the shape of the initial fire front within the cell (i.e. a point at the center, a straight line through the cell, or a line segment terminating at the midpoint of the cell) is not easy in a cellular automaton approach. As a simplified initial treatment, the heat release from initial cells is obtained by defining *R1* as the maximum of the eight spread rates obtained from the elliptical decomposition, defining *R2* as the spread rate in the opposite direction from

R1, and then evaluating (28) or (29) for both spread rates and taking the mean as the representative value of $F(t)$. (For the full derivation of (28) and (29), see Appendix 2.)

A quasi-discrete version of DEVS-FIRE was developed to calculate the sensible and latent heat fluxes at time t by solving the above equation set for F at times t and $t - \Delta t$ and using the results in (16) and (17). The fully-discrete and quasi-discrete versions were then tested for simple cases of constant "straight" and "diagonal" fire spread through a 5x5 DEVS-FIRE grid of resolution 10 m containing tall grass (fuel type 3 in Table 1), with the heat fluxes averaged on to a single 50-m ARPS grid cell. As shown in Fig. 19, the quasi-discrete method improves upon the fully-discrete method in at least two ways. First, the heat release from an individual cell is continuous and piecewise-smooth over all times, and therefore the spatial average avoids the "sawtooth" character of the spatial average produced by the fully-discrete solution. Second, it depicts the relationship between spread rate and heat release rate more reasonably, increasing the combustion rate of individual cells experiencing more rapid spread whereas the fully-discrete formulation employs only a static curve that is not at all influenced by the behavior of the fire front; any increase in heat flux due to cells igniting more frequently deteriorates rapidly between ignition times (while the spread rate is unchanged) and, obviously, disappears in the case where spatial averaging is not applied (e.g. if ARPS and DEVS-FIRE are run at identical resolution).

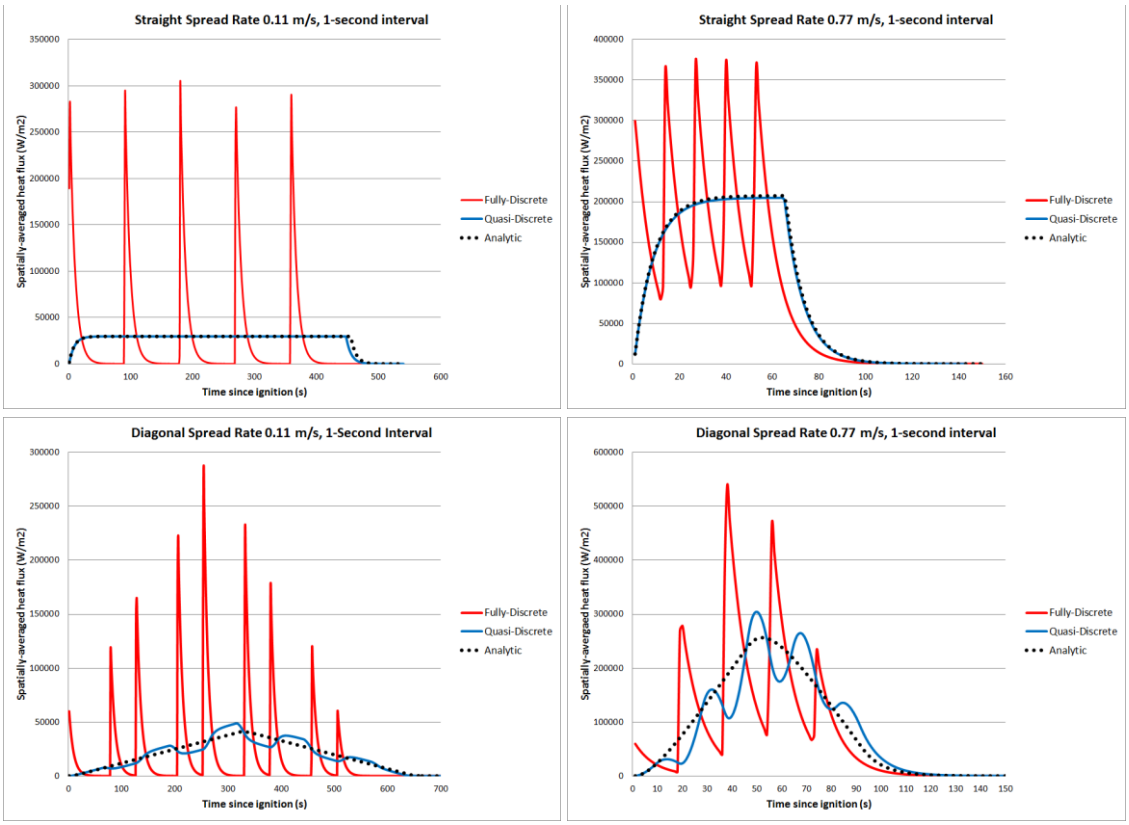

Figure 19: Spatially-averaged sensible heat flux averaged over one-second intervals for fully-discrete (red) and quasi-discrete (blue) DEVS-FIRE simulations of a straight fire front spreading at 0.11 m s^{-1} (left) and 0.77 m s^{-1} (right) at spread directions of 0° (top) and 45° (bottom). Black dotted lines denote analytic solutions.

It should also be noted from Fig. 19 that, while the quasi-discrete version of DEVS-FIRE matches the analytic solution for "straight" spread almost perfectly (with a very small difference due to rounding error), it is less ideal for "diagonal" spread. There is an evident periodic fluctuation about the analytic solution, the amplitude of which is greater at the faster spread rate. This is another manifestation of distortion due to the geometry of the DEVS-FIRE grid; essentially, since the cells are rectangular, it is impossible to represent a diagonal fire front perfectly on the grid. Since the spread of the fire front is represented as a series of discrete ignitions rather than a continuous

front propagating through the grid, this inaccurate representation of the initial line means that subsequent ignitions are mistimed. (See Fig. 20.) On the other hand, this error is still substantially less than that produced by the fully-discrete method (particularly at slower spread rates), and it may not be possible to develop a method for eliminating it that does not undermine the fundamental concept of the raster-based model. Therefore, it was regarded as a "necessary evil" when the quasi-discrete version of DEVS-FIRE was used in this research.

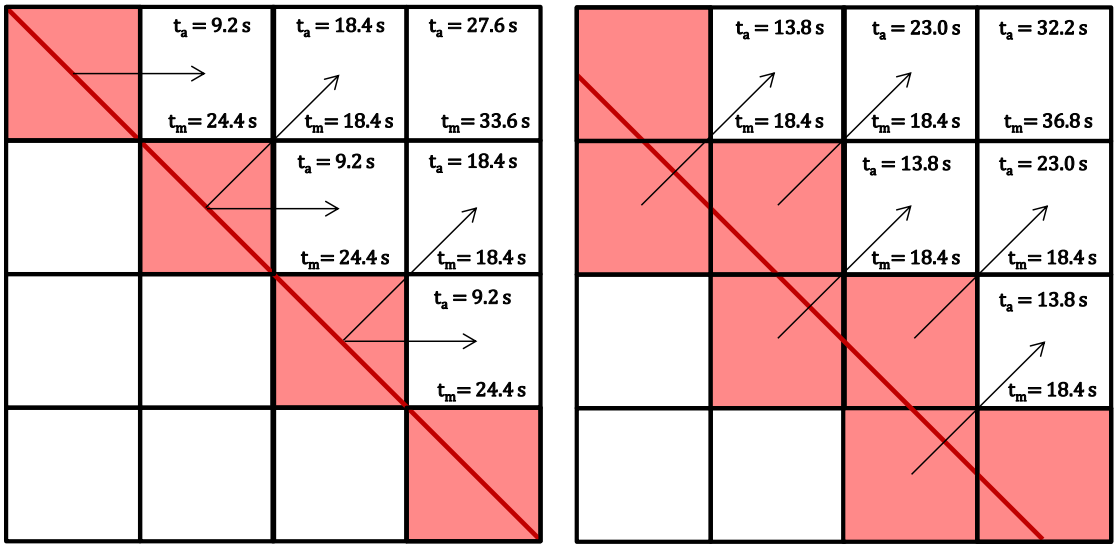

Figure 20: Comparison between analytic ignition times t_a and DEVS-FIRE model ignition times t_m for different initial representations of a diagonal fire front propagating to the northeast at a rate of 0.77 m s^{-1}. The red line marks the initial analytic position of the fire front, the shaded cells are the initial representation of the fire front in DEVS-FIRE, and the arrows show the ignition path between initial cells and their neighbors. (The representation on the right was used for the heat flux calculations plotted in Fig. 19.)

As in WRF-SFIRE, the preceeding methods do not attempt to either distinguish between sensible heat flux and radiant flux or explicitly account for heat flux into the ground. The main reason for this is that both the radiant flux and the ground flux

depend on the temperature of the burning fuel, which is difficult to estimate reliably due to the complexity of the combustion process and the simplifications already espoused by the model. However, a scaling analysis of measurements from experimental crib fires given in Emori and Saito (1983) provides a basis for obtaining at least a crude approximation of a combustion temperature consistent with the behavior of the model. Specifically, the measurements in Emori and Saito indicated a rough proportionality between combustion rate and surface radiative flux, which is in turn proportional to the fourth power of the reaction temperature. Furthermore, the mass loss rate at ignition (i.e. focusing solely on pyrolysis) is related to the reaction temperature by an Arrhenius equation like the one provided in Chan and Krieger (1982) for cellulosic fuels:

$$\left(\frac{dM}{dt}\right)_0 = -(M_0)A\exp\left(\frac{-E}{RT}\right) \tag{30}$$

A zero subscript denotes a value at ignition, M is the ovendry fuel mass, R = 8.314 J mol^{-1} K^{-1} is the Universal Gas Constant, T is the reaction temperature, and A and E are experimentally-derived coefficients for wood pyrolysis. (This derivation uses the values given by Chan and Krieger, $A = 1.3 \times 10^8$ s^{-1} and $E = 1.44 \times 10^5$ J mol^{-1}.) Since locally $f \equiv M/M_0$ and $f_0 = 1$, the fuel fraction loss at ignition is simply obtained by dividing through by M_0:

$$\left(\frac{df}{dt}\right)_0 = -A\exp\left(\frac{-E}{RT}\right) \tag{31}$$

This can be equated to the local fraction loss rate at ignition in the fire model. Differentiating (19) with respect to time and setting $t = 0$ gives

$$\left(\frac{df}{dt}\right)_0 = -\frac{1}{W} \tag{32}$$

Simply setting (31) and (32) equal to each other and solving for T is not accurate; the local combustion model treats ignition as a discontinuous leap from no combustion to maximum combustion at $t = 0$, and the temperature clearly should not be regarded as a constant during the leap. To find the temperature at the end of the leap (at which point the exponential decay curve takes effect), a "zero-order jump" approach (similar to the method for calculating boundary layer entrainment developed by Fedorovich, 1995) was employed in which the temperature shifts linearly from the ambient fuel temperature T_i to the ignition temperature T_f over an infinitesimally-small interval δt:

$$T(t) = T_i + (T_f - T_i)\frac{t}{\delta t} \tag{33}$$

The procedure now integrates (31) and (32) over the interval δt, obtains the limit as $\delta t \longrightarrow 0$, and solves for T_f. Integration of (31) from $t = 0$ to $t = \delta t$ for the fire model is trivial:

$$\frac{\Delta f}{\Delta t} = -\frac{\delta t}{W} \tag{34}$$

Substituting (33) into (31), applying the substitution $u = (T_f - T_i)\, t/\delta t$, and integrating for the fuel loss rate from the Arrhenius equation gives

$$\frac{\Delta f}{\Delta t} = -\left(\frac{\delta t}{T_f - T_i}\right)\int_0^{T_f - T_i} A \exp\left[\frac{-E}{R(T_i + u)}\right] du \tag{35}$$

Finally, setting (34) and (35) equal to each other and rearranging terms gives

$$T_f - T_i = W \int_0^{T_f - T_i} A \exp\left[\frac{-E}{R(T_i + u)}\right] du \tag{36}$$

Unfortunately, a general analytical solution to this form of integral does not exist. At this point, T_i = 300 K was selected as a generalization for the expected ambient fuel temperature and brute-force iterative methods were used to obtain ignition temperatures for all of the standard fuel types listed in Table 1. The results are shown in Table 3.

Table 3: Estimated DEVS-FIRE temperature at ignition for standard fuel types

Fuel Type Number	Description	Estimated Temperature at Ignition (K)
1	Short grass	928
2	Timber (grass and understory)	928
3	Tall grass	928
4	Chaparral	790
5	Brush (2 ft)	812
6	Dormant brush, hardwood slash	812
7	Southern rough	812
8	Closed timber litter	735
9	Hardwood litter	735
10	Timber (litter and understory)	735
11	Light logging slash	735
12	Medium logging slash	735
13	Heavy logging slash	735

Finally, based on the rough proportionality observed by Emori and Saito, the ratio between the net radiative flux (approximating the fuel as a blackbody) and the integrated fuel fraction decrease within the cell at any time *t* after ignition was set equal

to the ratio between the initial net radiative flux and the initial fuel loss rate from the fire model:

$$\frac{\sigma\left(T(t)^4 - T_i^4\right)}{\left[\frac{F(t)-F(t-\Delta t)}{\Delta t}\right]} = \frac{\sigma\left({T_f}^4 - T_i^4\right)}{\left(\frac{df}{dt}\right)_0} \tag{37}$$

Substituting (32) and solving for $T(t)$ gives

$$T(t) = \sqrt[4]{T_i^4 + \frac{F(t-\Delta t)-F(t)}{\Delta t} W\left({T_f}^4 - T_i^4\right)} \tag{38}$$

A third version of DEVS-FIRE was developed to calculate and report this estimated fuel temperature to ARPS for each active cell. ARPS was then modified to read the fuel temperatures, calculate the spatially-averaged radiative flux for each ARPS cell, obtain the "representative" surface temperature from this flux (again using a blackbody approximation), and then use this value as the surface temperature for calculating the ground flux. To ensure conservation of energy, the resulting radiative and ground fluxes were subtracted from the "bulk" sensible heat flux obtained from (16). (The evaporation rate is inextricably tied to the combustion rate in the model; therefore, the latent heat flux was not modified from the value given by (17).)

D. Description of Experiments

i. Uncoupled ARPS tests

Before the models were coupled, ARPS was subjected to various tests in order to gauge its ability to handle extreme surface fluxes in a realistic manner. To assess the

basic question of numerical stability, a 300-meter-wide region of 1 MW m^{-2} surface sensible heat flux was centered in a two-dimensional ARPS domain with a calm, neutrally-stratified base state. (Occasionally, instantaneous sensible heat fluxes over 2 MW m^{-2} are observed in wildfires. However, values averaged over intervals of one second or more are generally lower, as stated by both Clements et al., 2007, and Kiefer et al., 2008.) To evaluate the LES treatment of turbulence, ARPS was then run twice for ten minutes, once using the Moeng and Wyngaard TKE scheme and once using the non-local treatment developed Sun and Chang (1986). The results were examined for indications of unstable growth, and the potential temperature and wind fields were qualitatively evaluated in light of observed behavior described by previous studies (e.g. Clark et al., 1995).

Additional tests focused on the impact of vertical wind shear and fire front motion on atmospheric response in ARPS, similar to the experiments detailed in Kiefer et al. (2008). Since this response includes circulations that cannot be replicated in a two-dimensional simulation (see Fig. 7), a region of enhanced surface heat flux with a zonal line of symmetry was placed in a three-dimensional ARPS environment. The heated region was designed to replicate a sinusoidal fire front, either stationary or amplifying from an initially-straight segment; thus, the heat flux along the front was varied from a minimum of 0.125 MW m^{-2} on the flanks to 1 MW m^{-2} in the center. Furthermore, the heat flux was forced to decay exponentially in a smolder region behind the front, which also varied in depth with a maximum along the line of symmetry (i.e. the presumed location of fastest spread). The governing equations for the heat flux H in the burn region are

$$H(x,y) = (1\ \mathrm{MW\ m^2})\left[0.125 + 0.4375\left(1+\cos\theta_y\right)\right]\exp\left[S\left(x - x_c - 0.5A\cos\theta_y\right)\right]$$
$$\theta_y = \frac{2\pi(y-y_c)}{W} \qquad\qquad S = \frac{B}{\Delta x + C\left[A\left(1+\cos\theta_y\right)\right]} \tag{39}$$

θ_y is the advance phase angle of the fire front, S is the exponential decay parameter for the smolder region, x_c and y_c are the center coordinates of the fire front, A is the current amplitude of the fire front, A_f is the user-defined final amplitude of the fire front, W is the user-defined width of the fire front (i.e. the diameter perpendicular to the line of symmetry), and B and C are user-defined dimensionless constants determining the depth of the smolder region with a larger B indicating a smaller smolder region and a larger C indicating a greater variation in smolder region depth between the center and the flanks of the fire front. (To give a final e-folding depth of 100 m behind the center of the fire front diminishing to 20 m on the flanks, B was set to 2.5 and C was set to 0.125 for these tests.) For the stationary tests, the amplitude A was set equal to A_f at all times; for the amplifying tests, it was made to increase linearly from zero at initialization to A_f at the end of the simulation. The equation was only evaluated for regions behind the fire front (i.e. $x \leq x_c + A\cos\theta_y$ and $|y - y_c| \leq W/2$); otherwise, H was set equal to zero.

The initial ARPS environment was characterized by weak static stability ($\partial\theta/\partial z = 0.1\ \mathrm{K\,km^{-1}}$) below 5 km, moderate static stability ($\partial\theta/\partial z = 5\ \mathrm{K\,km^{-1}}$) above that, a westerly surface wind of 5 m s^{-1} (i.e. directed along the line of symmetry), purely zonal vertical shear within the lower 5 km, and an absence of Coriolis deflection. The

magnitude of the 0-5 km vertical shear was varied at increments of 10 m s^{-1} from easterly at 20 m s^{-1} to westerly at 20 m s^{-1}, producing a set of ten simulations (five for the stationary fire front, five for the amplifying fire front). The maximum vertical velocity and vertical vorticity were then plotted as functions of time for each simulation to compare plume strength and stability as well as the presence and persistence of fire vortices (as an indicator of "extreme" behavior).

ii. Symmetric coupled tests

Because detailed observations of actual wildfire behavior and atmospheric response are sparse, the coupled model was initially subjected to idealized tests where the expected qualitative behavior was well-established. As discussed in Chapter 2, tilting and stretching of fire-generated vorticity should cause an initially straight fire front to assume a symmetric parabolic shape over time in the absence of other factors (e.g. fuel bed irregularities). Even without a means of quantitative verification, the ability of the coupled model to replicate such behavior provides at least a partial basis for validating the model.

To keep this validation as simple as possible, a uniform, flat fuel bed consisting of tall grass was specified for the DEVS-FIRE grid. Likewise, the ARPS initial conditions were simplified from those used in the uncoupled tests by removing the vertical shear and variations in static stability (i.e. to avoid possible feedbacks from shear instability as described in Kiefer et al., 2008). Instead, a neutral profile with uniform zonal winds up to 2.5 km AGL was specified for each test. To account for surface friction, this profile was integrated forward for 30 minutes on a coarse (2-km horizontal resolution)

"background" grid and the results were interpolated to provide initial and boundary conditions for the fine-scale (90 m horizontal resolution) test grid. The DEVS-FIRE grid was then centered in the ARPS grid and an initial fire front 2 km in length was specified as a meridional set of ignition points centered on the zonal line of symmetry through both grids.

Multiple aspects of the coupling process were tested by varying the initial conditions and operational parameters of the models. In light of Clark et al. (1996b), the wind speed in the initial ARPS sounding was varied widely from simulation to simulation (ranging from 3 m s^{-1} up to 20 m s^{-1}) in order to test the impact of background wind speed on the significance of coupled feedbacks. Furthermore, simulations for each background wind speed were performed with DEVS-FIRE grid resolutions of 10, 30, and 90 m in order to assess any deleterious effects from the discrete-event treatment of fire spread on coarser grids. (ARPS was run at 90 m resolution for each of these tests.) Finally, after a series of tests was run with an update interval of 60 seconds, another set was run with an update interval of 1 second in order to test the simulated impact of feedbacks operating at finer time scales.

Each resulting burn area was compared with the analytically-expected parabolic shape described in the literature. In order to gauge the relative impact of coupled feedbacks at different wind speeds, the results were also compared with the burn areas produced by uncoupled simulations in which ARPS was allowed to update DEVS-FIRE but not vice versa. (In other words, the heat output from DEVS-FIRE was not mapped to the ARPS grid in the uncoupled tests.) Additionally, the normalized asymmetry of

the heat output from each simulation was calculated to provide a partial evaluation of error growth due to truncation:

$$\text{Asymmetry} = \frac{2\sum_{k=1}^{k=N}\sum_{i=1}^{i=nx}\sum_{j=1}^{j=\frac{ny}{2}-1}\frac{|H(i,j,k)-H(i,ny-j+1,k)|}{\max[H(i,j,k),H(i,ny-j+1,k)]}}{\sum_{1}^{k=N}P(k)} \qquad (40)$$

N is the total number of coupled model updates (equal to the total simulation time divided by the update time interval), *nx* and *ny* are the dimensions of the DEVS-FIRE grid, *i* and *j* are the coordinates of a given grid cell, *H* is the heat flux from cell (*i*,*j*) at update *k*, and *P* is the total number of active (burning) DEVS-FIRE cells at update *k*. While the initial, fully-discrete version of DEVS-FIRE was subjected to all the tests, the quasi-discrete version was also subjected to the final set as well; both sets of results were then compared to evaluate any benefits of the quasi-discrete treatment.

iii. Verification using FIREFLUX data

Historically, atmospheric conditions above wildfires are even more poorly-sampled than the spread and intensity of the wildfires themselves. FIREFLUX (Clements et al., 2007) was conducted to combat this data scarcity by providing local weather observations within the surface layer above a propagating controlled burn. The burn was conducted in a level field of tall grass, with the ignition coordinates of the fire tracked using GPS. Furthermore, a detailed survey of fuel loading and moisture content was conducted in advance of the burn, providing details not generally available to operational fire models. The observational network included infrared cameras, marking stakes, a radiosonde launched on the morning of the burn, a tethersonde with instruments at five fixed heights (3, 10, 50, 80, and 130 m AGL) at the southern edge of

the field, and two instrumentation towers located within the burn area. (See Fig. 21.) The towers provided high-frequency observations (1 Hz or better) of conditions both within and above the fuel before, during, and after the passage of the fire front; a partial list of the instrumentation deployed on the main tower (focused on in this study) is provided in Table 4.

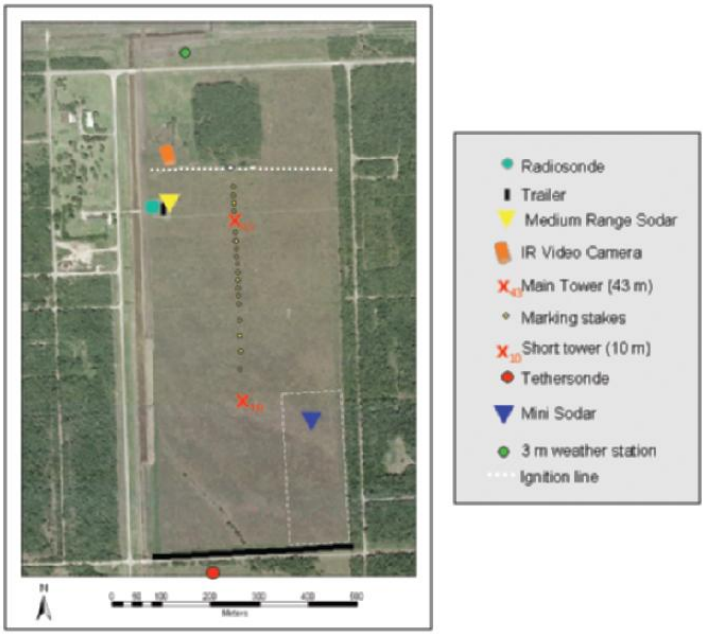

Figure 21: Map of burn site and instrumentation layout used for the FIREFLUX experiment. Ignition line is represented by white dots, and fire spread proceeded north-to-south. (from Clements et al. 2007, p. 1372)

Table 4: Large tower instrumentation used in FIREFLUX (from Clements et al. 2007, p. 1373)

Type	Variables	Measurement height m AGL)	Sampling frequency (Hz)
3D sonic anemometers (R.M. Young 81000)	u, v, w, sonic temperature	2.1, 10, 28.5, 42	20
Ceramic thermocouples (Omega, Inc., XC-24-K-12)	Fuel temperature	2.1, 1.73, 1.47, 0.6, 0.13	1
R.M. Young 5103 anemometer	Mean wind speed and direction	2, 10, 20, 42	1
CSI CS-500 temperature/RH probes	Mean temperature, RH	2, 10, 20, 42	1

The FIREFLUX dataset is currently considered the "gold standard" for coupled fire model validation (Craig Clements and Jan Mandel, personal communication) and has already been used to evaluate WRF-SFIRE (Mandel et al., 2011) and MesoNH/ForeFire (Filippi et al., 2012). The evaluation of ARPS/DEVS-FIRE proceeded in a similar manner to that employed for WRF-SFIRE in Mandel et al.; data from the morning sounding (launched at 0655 CST) were merged with the tethersonde and large tower observations at the time of ignition (12:43:30 CST) to provide a background atmospheric profile, which was then integrated forward on a coarse grid and interpolated to provide initial and boundary conditions for the coupled model.

The tabulated fuel loading and moisture properties for the standard "tall grass" fuel type (see Table 1) were altered to reflect the average values obtained by the survey conducted before the burn, with the dry fuel load increased to 1.08 kg m^2 and the moisture content increased from 3% to 18.5%. This modified fuel type was then mapped to the DEVS-FIRE grid. With terrain negligible and fuel heterogeneities generally ignored, extremely high resolution was used for both DEVS-FIRE (1 m grid spacing) and ARPS (10 m grid spacing). The ignition process was progressively mapped to the grid using the spatiotemporal coordinates from the FIREFLUX GPS record and a delayed ignition routine installed in DEVS-FIRE specifically for this case.

The ensuing fire spread was modeled five times: twice with the "bulk" heat fluxes specified at the surface only (once for the fully-discrete version, once for the quasi-discrete version); twice with the heat fluxes distributed quadratically through the lowest 10 m of the atmosphere (similar to the distribution used in WRF-SFIRE; see Mandel et al.); and once with radiant and ground fluxes separated from the "bulk" sensible heat

flux from the quasi-discrete version using the flame temperature estimate described in section C. In hopes of resolving fine-scale plumes and sharp gradients in the lowest 50 m of the atmosphere (i.e. the level observed by the main tower), computational mixing in ARPS was reduced by a factor of 10 from values used in the idealized experiments. ARPS was also modified to write out text files containing the surface temperature as well as the temperature, specific humidity, and three-dimensional wind components at 2 m, 10 m, 28 m, and 42 m AGL at the location of the large tower. The time series of observed and simulated conditions were then plotted using a 3-second rolling average to evaluate the realism of the atmospheric response depicted by ARPS.

iv. Case studies: the Moore Branch and Rock House fires

Along with the idealized simulations, the September 2000 Moore Branch Fire and the April 2011 Rock House Fire were selected as historical cases to test the performance of the coupled model in situations with real fuel and weather data. These wildfires were selected based on the availability of pre-event fuel and terrain surveys from the Texas Forest Service. The Texas Forest Service also produced GIS maps of the observed burn areas at regular intervals, which provided a basis for quantitative verification of the fire spread predicted by the coupled model.

The Moore Branch Fire was a multi-day event that consumed approximately 65 km^2 southeast of Newton, TX. (See Fig. 22.) Simulating the entire event was not feasible, due to both the computational expense and the expected accumulation of errors due to various sources of uncertainty; for example, the weather conditions in the area were poorly-sampled, the burn area was only mapped once every 24 hours, and the

impacts of firefighting activities were not quantified. Therefore, only the burn area from September 5th (hereafter "Day 5," when the fire became completely unmanageable according to Bean 2000) was re-created in this study.

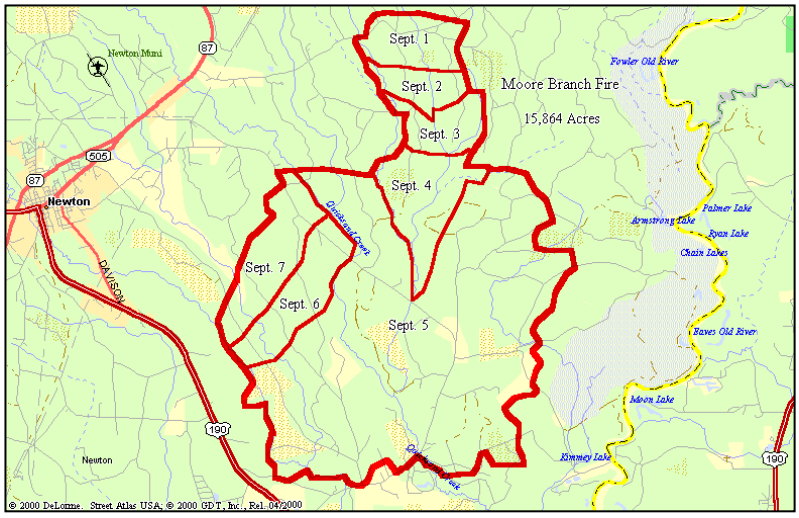

Figure 22: Approximate delineation of daily burn areas for the Moore Branch fire. Map extends roughly 16 km north-south and 26 km east-west (Bean 2000, p.6)

The fuel and terrain data from the Texas Forest Service survey were mapped to a 30 m resolution DEVS-FIRE grid, and the initial fire front position was translated from the Day 5 GIS burn area polygon to a set of ignition points in the DEVS-FIRE grid. In light of the uncertainty in the local weather conditions, two uncoupled simulations were performed, one using interpolated time-varying conditions from the 32 km North American Regional Reanalysis provided by the National Center for Environmental Prediction and the other using the daily maximum wind speed and direction (held constant) from an observing station at Kirbyville, roughly 16 miles south-southwest of the fire.

In addition, four coupled simulations were run at various ARPS resolutions (60 m, 150 m, 300 m, and 1.2 km) to test the impact of interpolation and unresolved feedbacks on the 24-hour burn area, with computational mixing specified the same as for the FIREFLUX tests. Along with qualitative comparison of the predicted and observed Day 5 burn areas, the false alarm rate (FAR), Critical Success Index (CSI), and Heidke Skill Score (HSS) were calculated for each burn area to provide rudimentary assessments of forecast skill. Scores were calculated using a purely binary ("burned" or "unburned") point-by-point assessment of hits (H), misses (M), false positives (F), and true negatives (N), with formulas as follows:

$$FAR = \frac{F}{F+N}$$

$$CSI = \frac{H}{H+F+M} \tag{41}$$

$$HSS = \frac{H+N-E}{H+M+F+N-E} \quad \text{where} \quad E = \frac{(H+M)(H+F)+(M+N)(F+N)}{(H+M+F+N)}$$

It should be noted that most of the northern portion of the DEVS-FIRE grid for this case would not have been forecasted to burn on Day 5 under any circumstances, either because it was marked as burned on previous days or simply because the general northerly wind throughout the day made substantial spread in that direction highly unlikely. In order to mitigate contamination of the above metrics by a large number of correct point forecasts purely due to chance, the northern third of the grid was not included in the skill calculations.

The wind speeds for the Moore Branch Fire were comparatively modest, with a maximum of 9.9 m s^{-1} observed at Kirbyville and generally much weaker winds

indicated by the reanalysis data. (See Table 5.) The Rock House case was selected in part because it occurred in a much more dynamic environment, with sustained winds near 15 m s^{-1} and gusts up to 25 m s^{-1} observed in the hours immediately following ignition. Furthermore, a previous set of uncoupled FARSITE simulations substantially underpredicted the initial fire spread for this case (described in Martin, 2011; see Fig. 23), suggesting the possibility of significant improvement using a coupled method.

Table 5: North American Regional Reanalysis surface wind speed and direction interpolated to the location of the Moore Branch Fire on 5 September 2000

Time (CDT)	Wind Speed (m s^{-1})	Wind Direction (degrees)
12:00 a.m.	0.188	105
3:00 a.m.	1.835	22
6:00 a.m.	2.135	29
9:00 a.m.	5.569	42
12:00 p.m.	6.908	48
3:00 p.m.	4.775	49
6:00 p.m.	1.386	9
9:00 p.m.	2.48	16

Examination of the Rock House case was also motivated by the data limitations of the Moore Branch case. Whereas hourly *in situ* weather observations were not available near the Moore Branch Fire, the Rock House Fire ignited only a few km south-southwest of the Marfa, TX ASOS station. Furthermore, only 32 km reanalysis data were available for the Moore Branch boundary conditions, whereas a 12 km operational NAM analysis was available for the Rock House boundary conditions at essentially the time of ignition (near 1800 UTC). Finally, the firefighting activities and vigorous initial spread of the Rock House Fire were documented more thoroughly, with the burn area outlined at 6-hour intervals. Therefore, coupled and uncoupled

simulations of the first 12 hours of the Rock House fire were performed using the fully-discrete version of DEVS-FIRE with fuel and terrain mapped from Texas Forest Service survey data to a 30 m grid as before. (The quasi-discrete version of DEVS-FIRE was not tested here due to limited computational resources and the evaluation of the fully-discrete results detailed in the next chapter.)

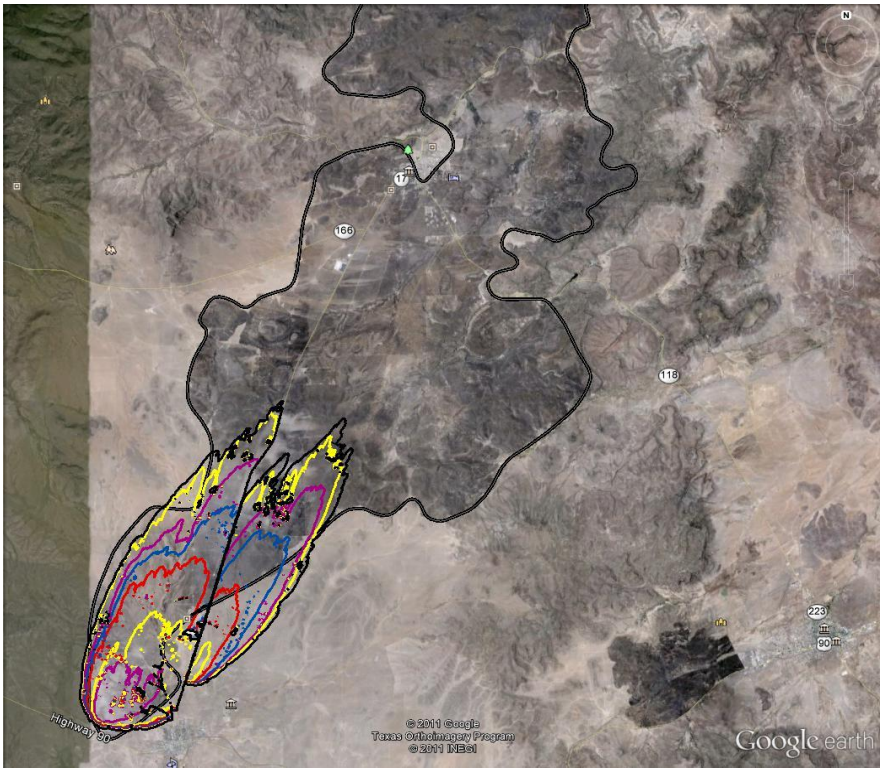

Figure 23: Comparison between FARSITE simulated burn area (colored contours at hourly intervals) and actual burn area (grey shaded region) for the first six hours of the April 2011 Rock House Fire. Map extends roughly 40 km north-south and 48 km east-west. (from Martin 2011, p.5)

CHAPTER 4

RESULTS AND DISCUSSION

A. Uncoupled ARPS Tests

The vertical cross section of perturbation potential temperature and wind vectors from the two-dimensional stationary simulation using the Moeng and Wyngaard TKE scheme is shown in Fig. 24. In agreement with observed behavior (e.g. as detailed in Clark et al., 1995), initial lack of mixing produced a thin layer of extremely hot air (approaching 1500 K) immediately above the ground. Shortly thereafter, explosive autoconvection produced a well-formed, initially- symmetric plume. After ten minutes of simulation, there was no indication of unstable error growth trending toward model failure. However, Fig. 24 also shows an onset of obvious asymmetry due to accumulated truncation error after a few minutes, which should be borne in mind when interpreting later results.

To test the sensitivity of the model results to the choice of TKE parameterization, a subsequent run was performed using the Sun and Chang 1986 scheme. However, it rapidly became clear that the non-local approach was both ill-suited to coping with such extreme temperatures and highly sensitive to changes in vertical resolution. As shown in Fig. 25, the Sun and Chang scheme produced a rapid buildup of TKE and eventual model failure, even when the near-surface vertical resolution was decreased to 25 m in an effort to damp the TKE buildup by artificially increasing the mixing length scale. Since accurate high-resolution treatment of near-surface feedbacks is crucial to model

success, the Moeng and Wyngaard TKE scheme was used for all subsequent simulations.

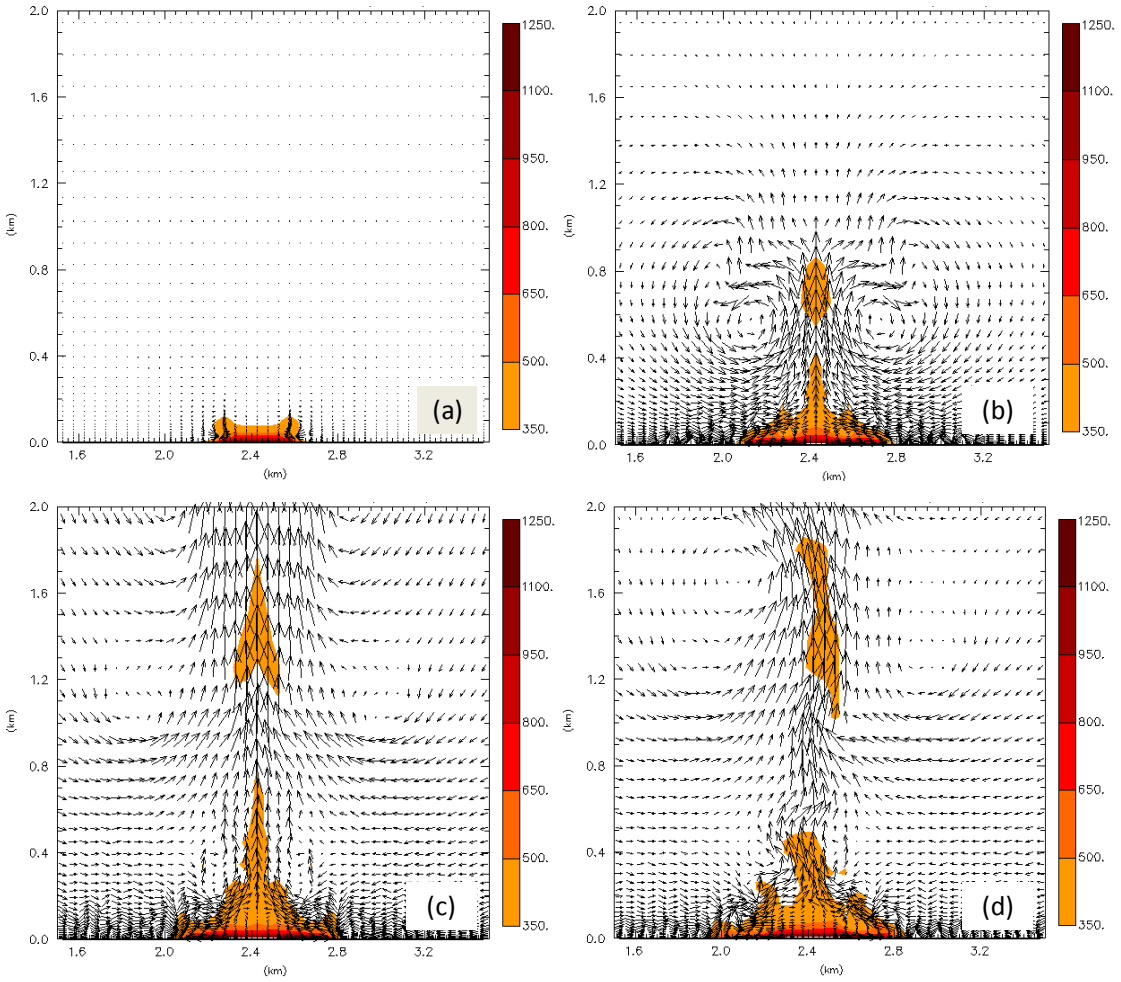

Figure 24: Two-dimensional ARPS test centered over an externally-forced sensible heat flux of 1 MW m^{-2} at elapsed times of (a) 30 seconds, (b) 120 seconds, (c) 210 seconds, and (d) 300 seconds. Colors indicate positive perturbation potential temperature, while vectors indicate perturbation winds in the x-z plane.

The symmetry of the initial plume in Fig. 24 is due not only to the symmetry of the background atmospheric conditions (windless and thermodynamically uniform), but also to the uniformity of the surface heat flux; the magnitudes of the buoyancy gradients on the left and right sides of the fire are equal, so both sides generate horizontal vorticity of equal magnitude and opposite sign. In actual wildfires, on the

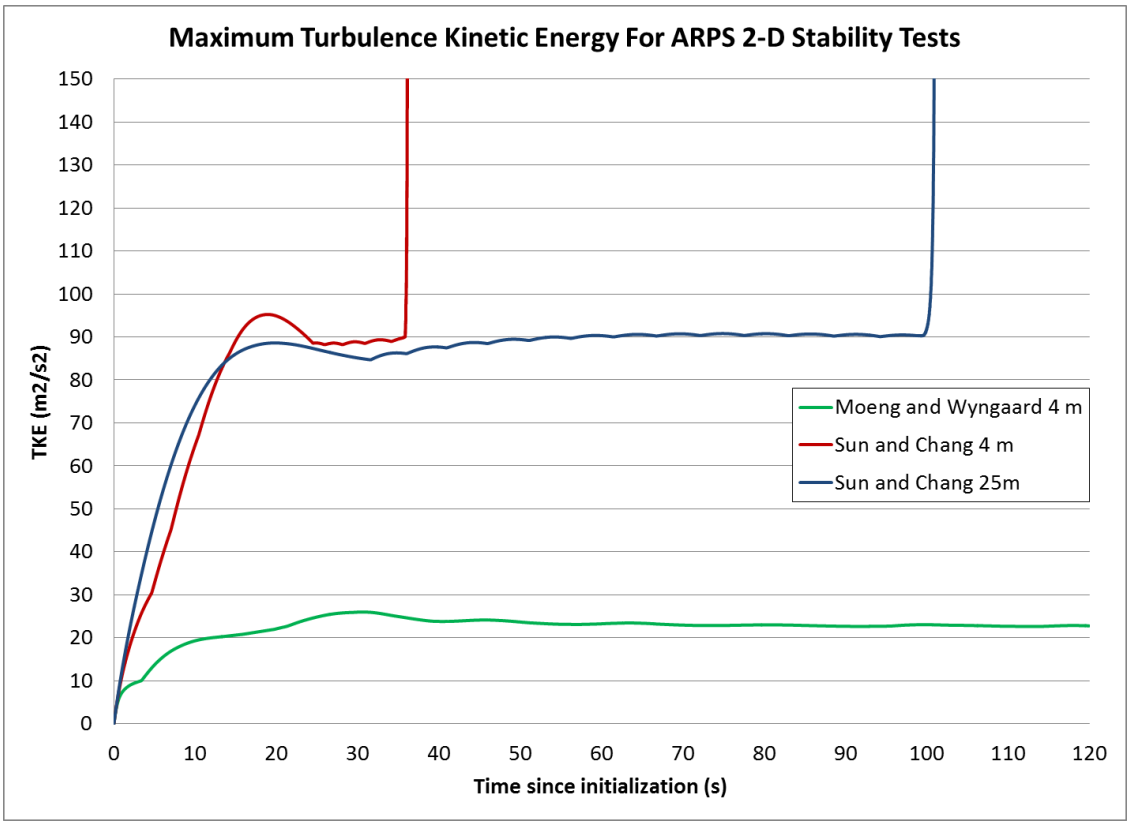

Figure 25: Maximum turbulence kinetic energy for ARPS 2-D stability tests using the Moeng and Wyngaard TKE scheme at 4 m surface vertical resolution (green) and the Sun and Chang scheme at vertical resolutions of 4 m (red) and 25 m (blue)

.

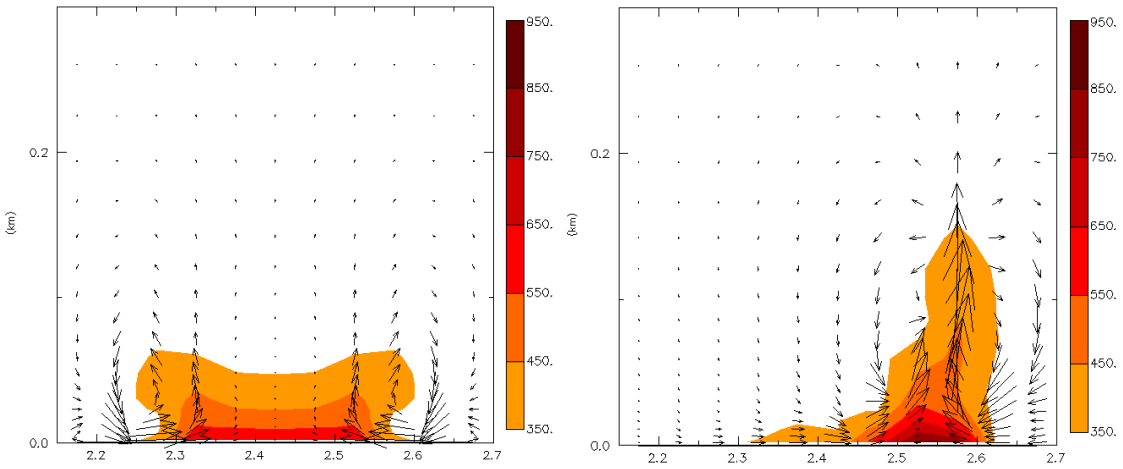

Figure 26: Same as Figure 24, but zoomed on the fire at t = 30 seconds for constant heat flux (left) and heat flux decaying exponentially from right to left (right).

other hand, the heat flux is strongest at the fire front and decays gradually in the smolder region. As shown in Fig. 26, this produces stronger horizontal vorticity ahead of the fire front and weaker vorticity behind, tilting the plume in a direction forward of the fire front even without the influence of ambient winds.

Naturally, if the ambient wind in the boundary layer is in the same direction as the fire spread, the tilt of the plume is increased. However, the subsequent behavior of the plume depends on the magnitude and direction of the vertical wind shear in the initial phase, even before waves from shear instability can amplify enough to have a significant influence as described in Kiefer et al. (2008). The time series of perturbation potential temperature, maximum vertical velocity, and maximum vertical vorticity for the stationary and amplifying ARPS fire fronts are shown in Fig. 27. Each case is designated by the behavior of the fire front ("stat" for stationary, "amp" for amplifying) as well as the initial magnitude and direction of the vertical shear ("B" for backward from the fire front position, "F" for forward, and "zero," "10," or "20" for the amount of vertical shear in m s^{-1}). Whether the fire front was stationary or amplifying, the presence of backward shear (i.e. in the "B10" and "B20" cases) implies a wind reversal, and it is clear from Figs. 27 and 28 that this reversal helped maintain a coherent, upright updraft structure whereas the presence of forward shear (i.e. in the "F10" and "F20" cases) broke the plume into a series of smaller cells propagating rapidly away from the fire front. Thus, the backward-shear cases develop solitary, intense plumes with updraft speeds approximately double those of the forward shear cases. (See panels C and D of Fig. 27.)

Figure 27: Maximum perturbation potential temperature, vertical velocity, and vertical vorticity for stationary (a,c,e) and amplifying fire fronts (b, d, f). Ambient vertical shear in the lowest 5 km varies by simulation: backward at 20 m s^{-1} (blue), backward at 10 m s^{-1} (green), no shear (black), forward at 10 m s^{-1} (orange), and forward at 20 m s^{-1} (red).

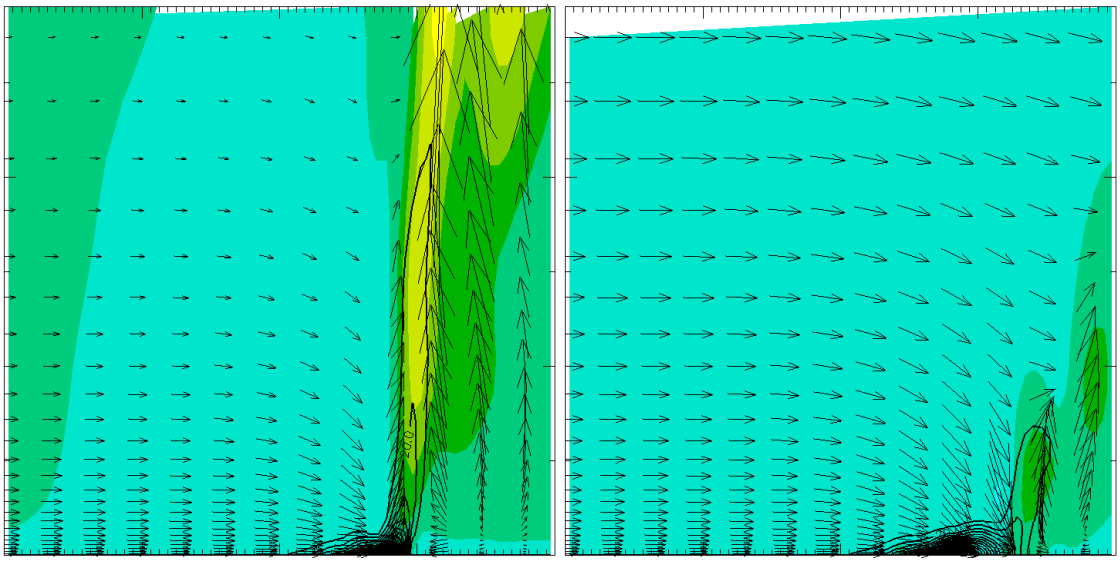

Figure 28: 2-km-by-2-km vertical cross-section of perturbation potential temperature (black contours), vertical velocity (color fills), and two-dimensional wind (arrows) through amplifying fire front center for 20 m s^{-1} backward shear (left) and forward shear (right) over the lowest 5 km at t = 600 seconds.

The generation of vortices on the fire front depends on the tilting and stretching of horizontal vorticity from either environmental shear, fire-induced buoyancy gradients, or both. Therefore, one would theoretically expect a higher magnitude of vorticity to correspond to a stronger updraft. However, Fig. 27 shows that this was not necessarily true for the amplifying fire front cases; while the intense plumes produced by both of the backward-shear cases are apparent in the vertical velocity time series in panel D, panel F does not generally show corresponding increases in vertical vorticity magnitude. This appears to be at least partially attributable to the motion of the fire front, for two reasons. First, Fig. 29 shows that the amplifying fire front had a tendency to overtake the vortices, thereby removing them from the region of maximized tilting and stretching on the leading edge. This is particularly clear in the "B20" case, in which the vortices move slowly due to weaker layer-averaged winds near the ground.

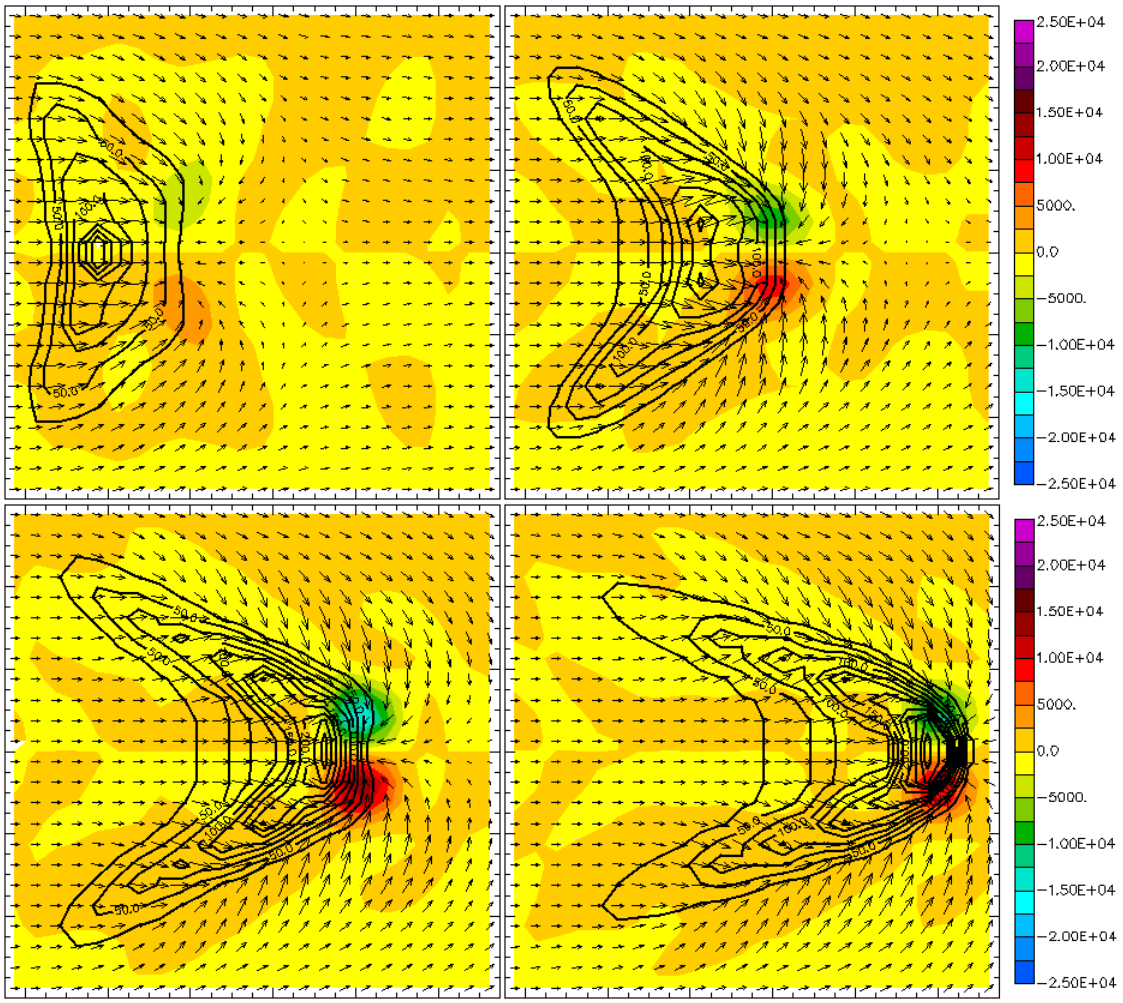

Figure 29: 1.2-km-by-1.2-km plots of 2m AGL perturbation potential temperature (black contours), horizontal wind (arrows), and vertical vorticity (color fills in units of 10^5 s^{-1}) at t = 120 s (upper left), 360 s (upper right), 600 s (lower left) and 840 s (lower right) for the case of backward vertical shear of 20 m s^{-1} over the lowest five km.

Second, the potential temperature time series in panel B of Fig. 27 shows a much more pronounced fluctuation compared with the time series for the static cases shown in panel A; since a 50 m grid resolution was used for these simulations and the leading edge of the fire front was forced to move at a speed of slightly over 1 m s^{-1}, the periodicity of the fluctuations corresponds closely to the frequency with which the leading edge of the fire front passed between adjacent cells. Since the heat flux was

simply a point value assigned to the Arakawa-C scalar location (rather than a spatial average) for a given ARPS cell in these tests, there was not necessarily a smooth transition in which the cooling of one cell meshed with the warming of its neighbor as the fire front passed between them. Rather, there was a time lag during which the first cell cooled while the neighbor cell remained "dormant" due to the fact that the fire front had not yet reached its center. The resulting fluctuation disrupted the updraft structure (and thus the intensification of vortices) in the lowest levels of the atmosphere, although the structure aloft remained intact. (This result emphasizes the importance of the spatial averaging methods developed for the coupled model, as described in section 3C.)

For the stationary fire front cases, the expected correlation between updraft speed and generation of vertical vorticity is largely borne out by Fig. 27. However, it should be noted from Fig. 29 that the sense (cyclonic or anticyclonic) of the vortices on the leading edges of the fire fronts is opposite that depicted in Clark et al. (1996b) for the development of "dynamic fingers," with an anticyclonic vortex to the north and a cyclonic vortex to the south. (Compare with Fig. 7.) This may be traced to the fact that neither the stationary nor the amplifying fire front is truly coupled to the atmosphere; since the spread rates are fixed, the dynamic feedback loop responsible for these vortices is not completed and they do not persist. The dominant factor in these cases appears to be the development of streamwise vorticity along the flanks of the fire front and its subsequent advection toward the intense plume in the center, where tilting and stretching occurs. Specifically, Fig. 29 shows that convergence from the initial convection causes the surface wind near the flanks to turn inward (anticyclonically on

the northern flank and cyclonically on the southern flank); as the fire front amplifies, this wind is directed increasingly parallel to its leading edge. In this area, the sense of the vorticity arising from the buoyancy gradient is opposite that depicted in Fig. 7 since the latter emphasizes vorticity generated behind the fire front and increasingly advected over it due to the strengthening of the winds associated with the dynamic feedback. Therefore, the generated streamwise vorticity is anticyclonic on the northern flank and cyclonic on the southern flank, producing the observed vortex pair near the center.

Along with stronger plumes producing more tilting and stretching, the greater vorticity in the backward-shear cases may be attributed simply to the residence time of the vortices over the region of peak heating. As shown in Fig. 30, the frequent splitting of the plumes in the forward-shear cases into smaller cells propagating away from the fire fronts coincides with an increased tendency of the vortices to move away from the fire front as well. This tendency is demonstrated in panels A and F of Fig. 27; beginning around t = 450 seconds, fluctuations in the potential temperature time series for the forward-shear cases increase steadily in amplitude, coinciding with increased breakup of the plume. At the same time, the maximum vorticity in both cases decreases markedly. On the other hand, the fluctuations of the surface potential temperature are much more muted for the backward-shear cases (coinciding with a continuous plume), and the vertical vorticity is better maintained.

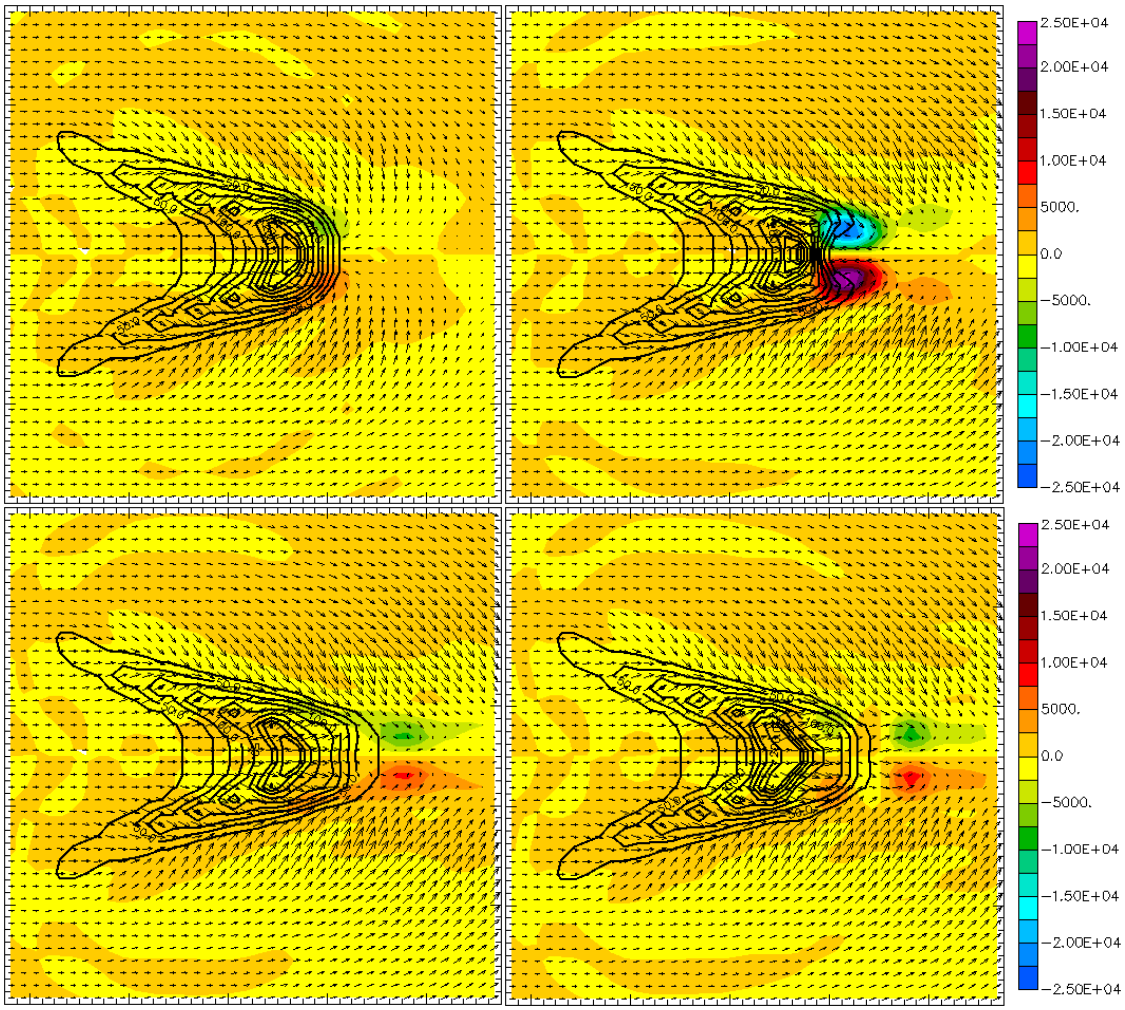

Figure 30: Same as Fig. 29, but for a stationary fire front with forward shear of 20 m s^{-1} at t = 180 s (upper left), 420 s (upper right), 660 s (lower left), and 900 s (lower right)

While these simulations do not precisely conform to recognized fire behavior in all respects, the behavior is reasonable considering the lack of full coupling at this stage. Moreover, ARPS demonstrated the ability to remain numerically stable in the presence of intense surface heat fluxes as long as lateral boundary conditions were externally forced by a coarse-grid background simulation; it should be noted that failure to do so (for example, initializing the model directly from a sounding and applying

radiation lateral boundary conditions) produced results (not shown here) that were heavily contaminated by spurious perturbations arising from the contrast between the near-surface boundary conditions and the frictionally-altered wind field within the domain. Thus, when correct initialization practices are employed, these test results justify coupling ARPS to DEVS-FIRE.

B. Symmetric Coupled Tests

The coupled tests run with an update interval of 60 seconds illustrated the value of coupling the models. Figure 31 shows the outlines of the coupled and uncoupled burn areas for wind speeds of 3 m s^{-1} and 12 m s^{-1} after 30 minutes. While the degree to which the small protrusions interspersed along the flanks were influenced by model artifacts (e.g. raster-based distortion) as opposed to realistic mechanisms (e.g. fire vortices) was uncertain, they were generally transient. Furthermore, coupling ARPS and DEVS-FIRE at high resolution mitigated the unrealistically blunt, angular character of the fire fronts produced by DEVS-FIRE acting alone on a homogeneous initial state.

Overall, the shapes of the fire fronts conformed to theoretical expectations in a manner comparable to that observed in similar tests using other coupled models (e.g. CAWFE, as detailed in Clark et al., 2004). The lone exception was the 3 m s^{-1} test performed at 10 m resolution, which developed a pair of bookend vortices on the flanks (similar to those shown in Figures 29 and 30) that became unrealistically intense and persistent. However, it should be noted that disruption of the fire front by flank vortices was also reported for symmetric tests in Clark et al. (2004), albeit to a lesser

degree; this difference may be attributed to the narrower initial fire front and slower-burning fuel (chaparral) employed there.

The influence of DEVS-FIRE resolution is obvious from both the plots in Fig. 31 and the statistical evaluation in Table 6. Additional truncation error is evident as the resolution decreases, both in the smaller uncoupled burn area and in the gradual increase in asymmetry. Furthermore, the discontinuous nature of the heat release at coarse resolutions (see Fig. 19) has a clearly deleterious effect on the coupled feedbacks for the 90 m DEVS-FIRE resolution, particularly in the slower-spreading 3 m s^{-1} case. However, the 30 m results are comparable to the 10 m results, suggesting that a 30 m resolution was sufficient to resolve the essential processes when the longer update interval was used.

Figure 31: Burn areas at t=1800 seconds for idealized uncoupled (black) and coupled (red) simulations for initial surface winds of 3 ms_{-1} (left) and 12 ms_{-1} (right) and DEVS-FIRE grid resolutions of 10 m (top), 30 m (middle, and 90 m (bottom). Thin lines denote east-west lines of symmetry, and the images are zoomed to the burn areas.

Table 6: Comparison of coupled (C) vs. uncoupled (UC) 30-minute burn areas from idealized symmetric simulations with a 60 second update interval

DEVS-FIRE resolution (m)	Background wind speed (m s^{-1})	UC burn area (km^2)	Burn area difference (C – UC, km^2)	Normalized Difference (%)	Coupled Asymmetry (%)
10	3	2.07	3.71	179.2	0.22
30	3	2.01	3.61	179.9	0.79
90	3	1.96	1.39	71.1	2.95
10	12	10.91	0.63	5.8	0.16
30	12	10.77	0.97	9.0	0.54
90	12	10.48	0.73	7.0	0.86

Unfortunately, the tests using a 1-second update interval revealed a serious shortcoming of the model. Specifically, whereas deviations from the expected fire front shape in the previous tests were generally brief, the later tests developed large, unrealistic protrusions both at the head of the fire and along the flanks. As shown in Fig. 32, these fingers were increasingly robust for higher wind speeds. Furthermore, Fig. 33 demonstrates that the deviations began almost immediately after initialization, before errors (e.g. from truncation) in ARPS would be expected to play a role.

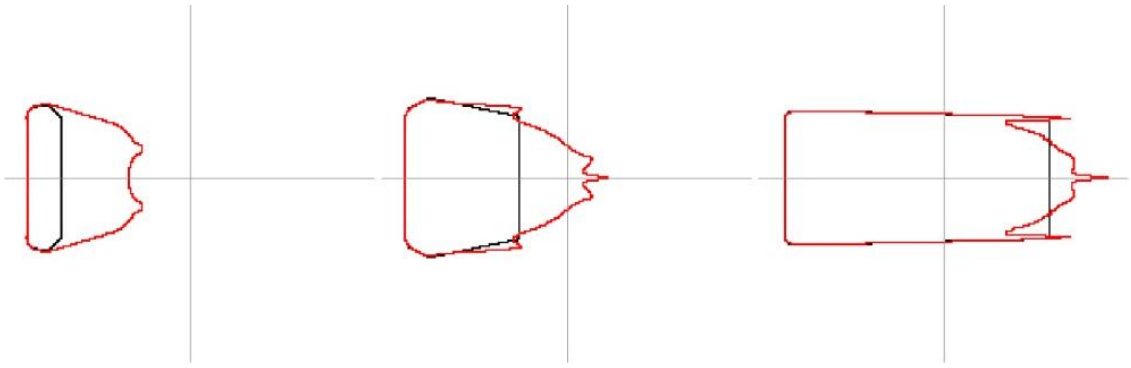

Figure 32: As in Figure 31, but for DEVS-FIRE resolution of 10 m, update interval of 1 second, and background winds of 3 (left), 10 (center) and 20 m s^{-1} (right)

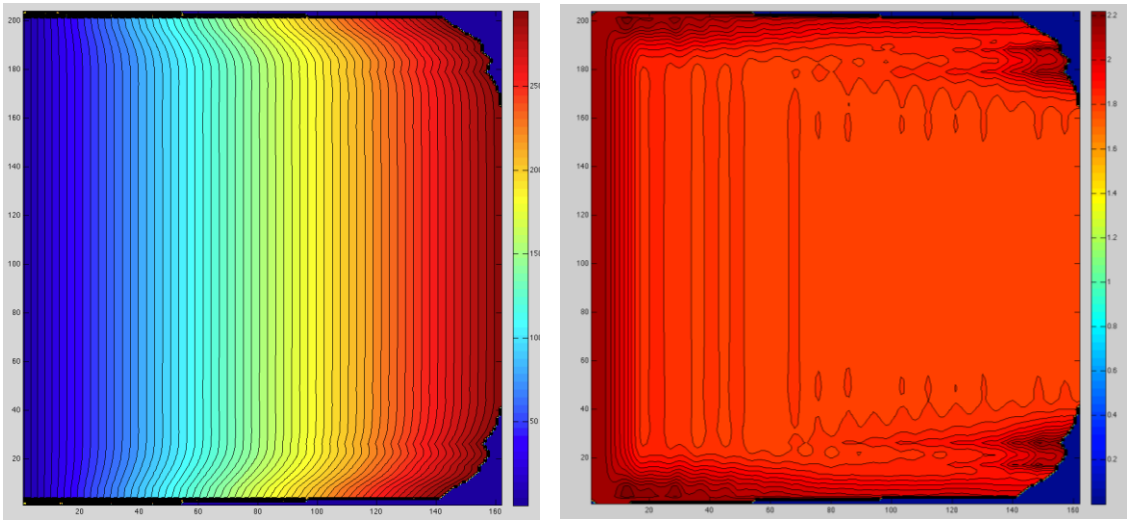

Figure 33: Contour plots of ignition time (left) and ignition delay between successive cells in the x-direction (right) within the burn area up to t = 300 seconds for the fully-discrete symmetric test with a background westerly wind of 20 m s^{-1}. (Deep blue region on the right edge of each panel is outside the burn area.)

Therefore, these artifacts appear to be tied to the distortion inherent in the fire front representation in DEVS-FIRE; the tendency to produce angular fire front shapes with unnatural "kinks" precipitates the development of strong localized vorticity in ARPS just upstream of the kinks (anticyclonic north of the line of symmetry, anticylonic south of the line of symmetry; see Fig. 34.) The main reason for this appears to be linked to the linear dynamic perturbation pressure

$$p_L' \propto \frac{d\vec{V}}{dz} \cdot \nabla_h w \tag{42}$$

where $\vec{V}$ is the horizontal wind vector and $\nabla_h w$ is the horizontal gradient of the vertical velocity. As shown in Fig. 7, convergence underneath the plume produces enhanced surface wind speeds and negative shear upstream of the fire front. Thus, the value for p_L' on the upstream side of the combustion zone is negative, indicating a drop in

pressure. When the background flow is perpendicular to the fire front (e.g. the center segment of the angular front in Fig. 34), this pressure drop is comparatively large; when the fire front is oriented at a substantial angle to the background flow, it is smaller. Therefore, sharp angles of the sort shown in Fig. 34 result in a component of the perturbation pressure gradient acting along the fire front at the location of the kinks, as shown in Fig. 35. Since the density gradient is largely perpendicular to the fire front due to the extreme heat, baroclinic vertical vorticity generation is maximized in these areas, producing the vortex pair shown in Figure 34.

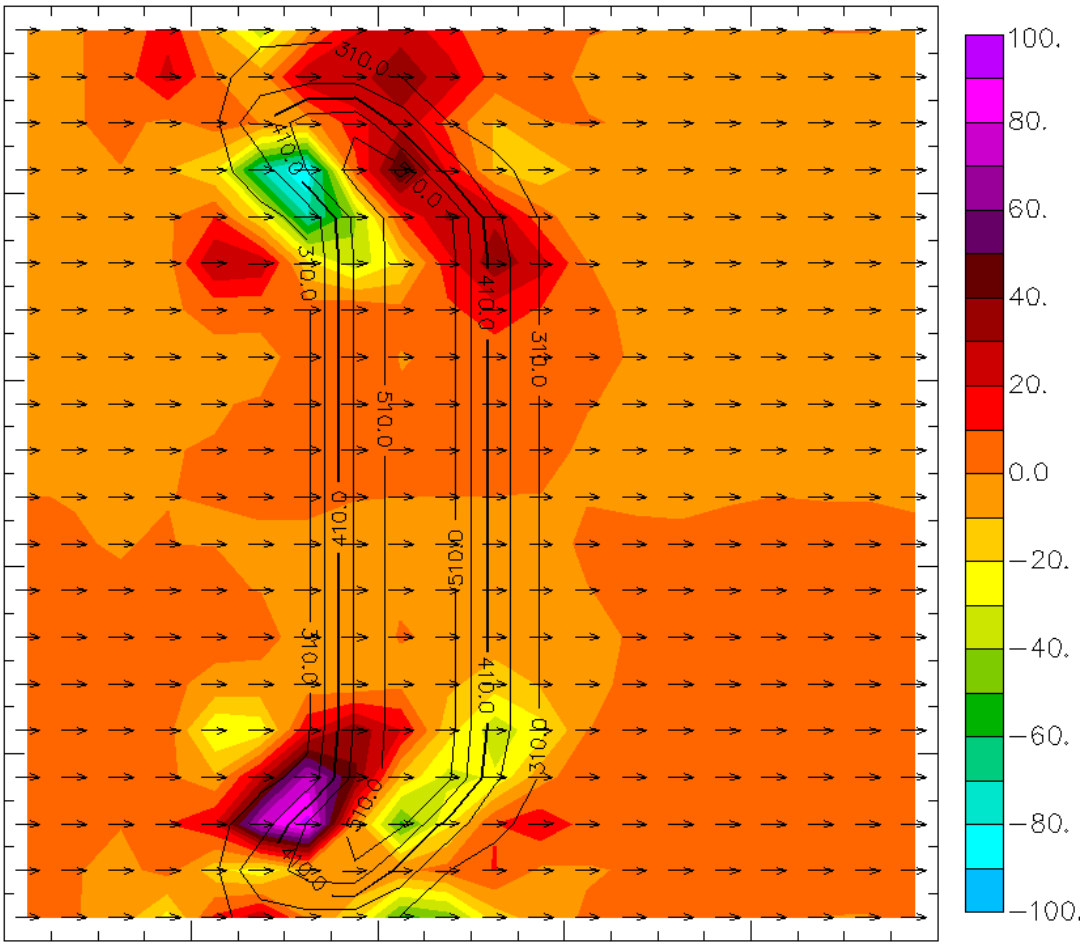

Figure 34: Surface temperature (contours), wind (vectors), and vertical vorticity (color fills, units of 10^5 s^{-1}) at 2m AGL for stationary angular fire front imposed on shear-free ARPS grid at t = 1.5 s.

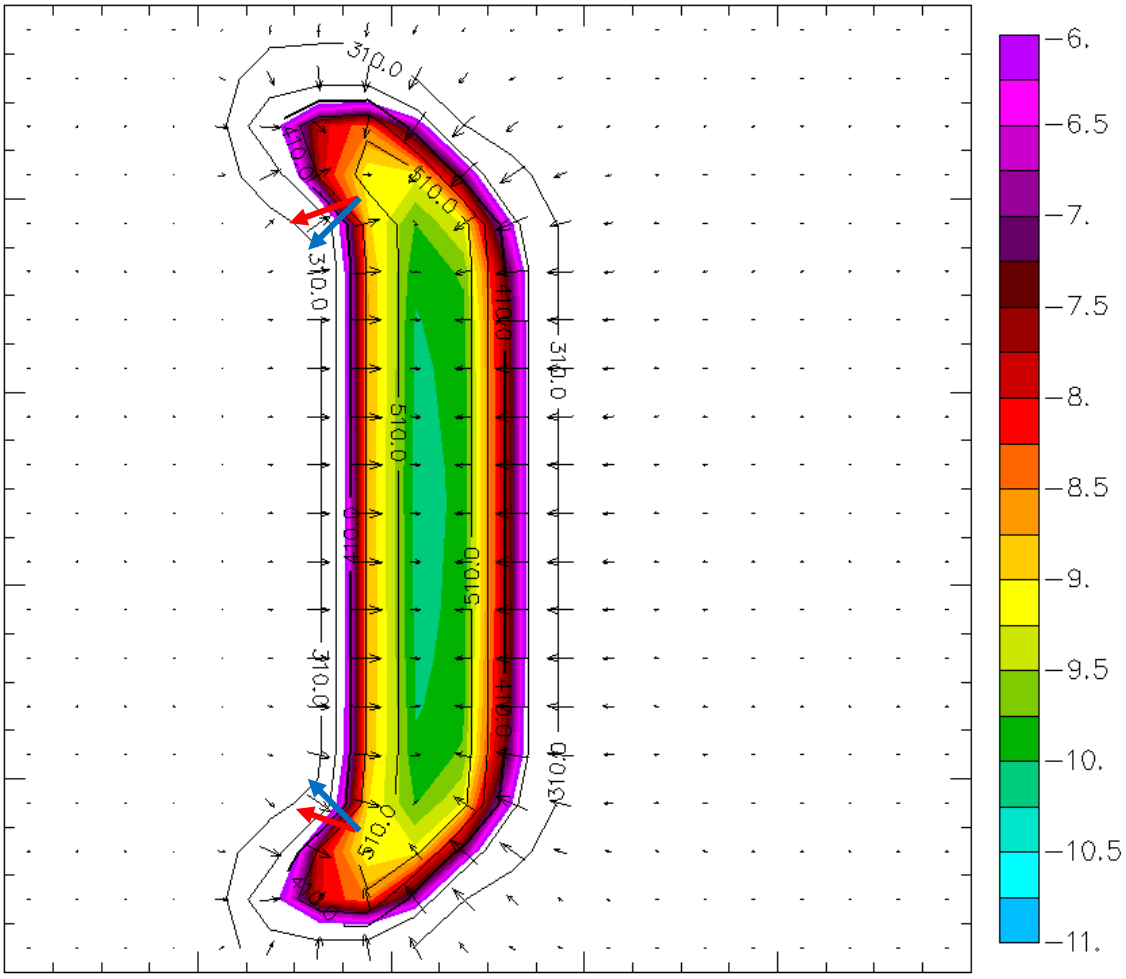

Figure 35: Potential temperature (contours), perturbation winds (vectors) and perturbation pressure (color fills, units of Pa) at 2 m AGL for stationary angular fire front imposed on shear-free ARPS grid at t = 1.5 s. Red and blue arrows show approximate alignment of horizontal pressure gradient and horizontal density gradient, respectively.

The generated vorticity is of a sense that strengthens the surface wind and the spread rate on the outward side of the kinks. In turn, this faster spread produces "hot spots" along the flanks; ARPS responds by further strengthening the local wind, producing a further increase in spread rate and a continuation of the feedback until spurious "fingers" develop and amplify away from the line of symmetry. These

perturbations were apparently smoothed out when a longer update interval was employed (with surface heat fluxes reduced due to greater temporal averaging), mitigating the feedback and forestalling the development of obvious errors.

As shown in Fig. 36, increasing the resolution in DEVS-FIRE by more than a factor of three failed to appreciably refine the fire front shape, reduce the "hot spots" on the flanks, or modify the initial response of the ARPS wind field to the fire before fingers began to develop. It was hoped that applying quasi-discrete heat release formulas (28) and (29) would smooth the error sufficiently without the need for for applying a longer update interval. However, Fig. 37 shows that the difference between the fully-discrete and quasi-discrete treatments was minimal, becoming essentially indistinguishable for a 20 m s^{-1} background wind.

In summary, the representation of general coupled behavior by ARPS/DEVS-FIRE largely conforms to theoretical expectations in idealized tests. However, the current model is clearly unable to resolve finer-scale feedbacks reliably, and the raster-

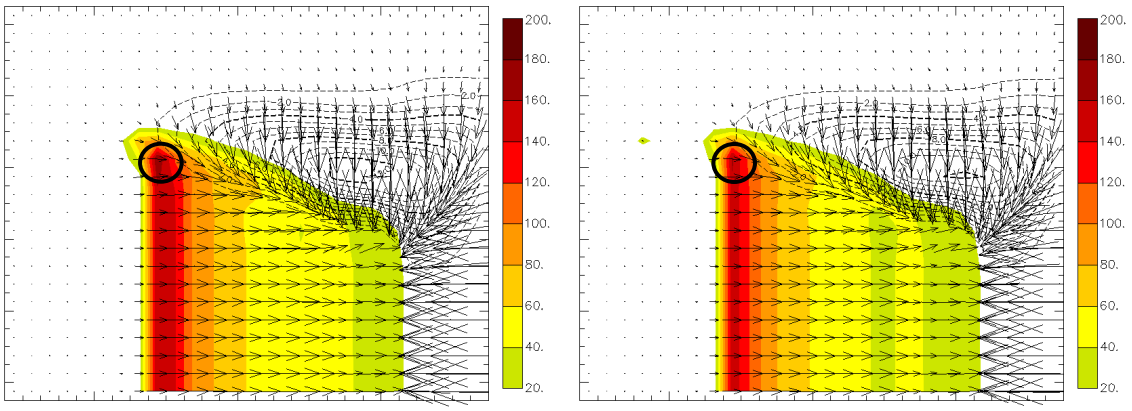

Figure 36: Perturbation potential temperature (color fills), perturbation meridional wind (contours) and wind vectors for fully-discrete idealized tests with background 20 m s^{-1} westerly wind using DEVS-FIRE resolutions of 3 m (left) and 10 m (right). Erroneous "hot spots" are marked by black circles.

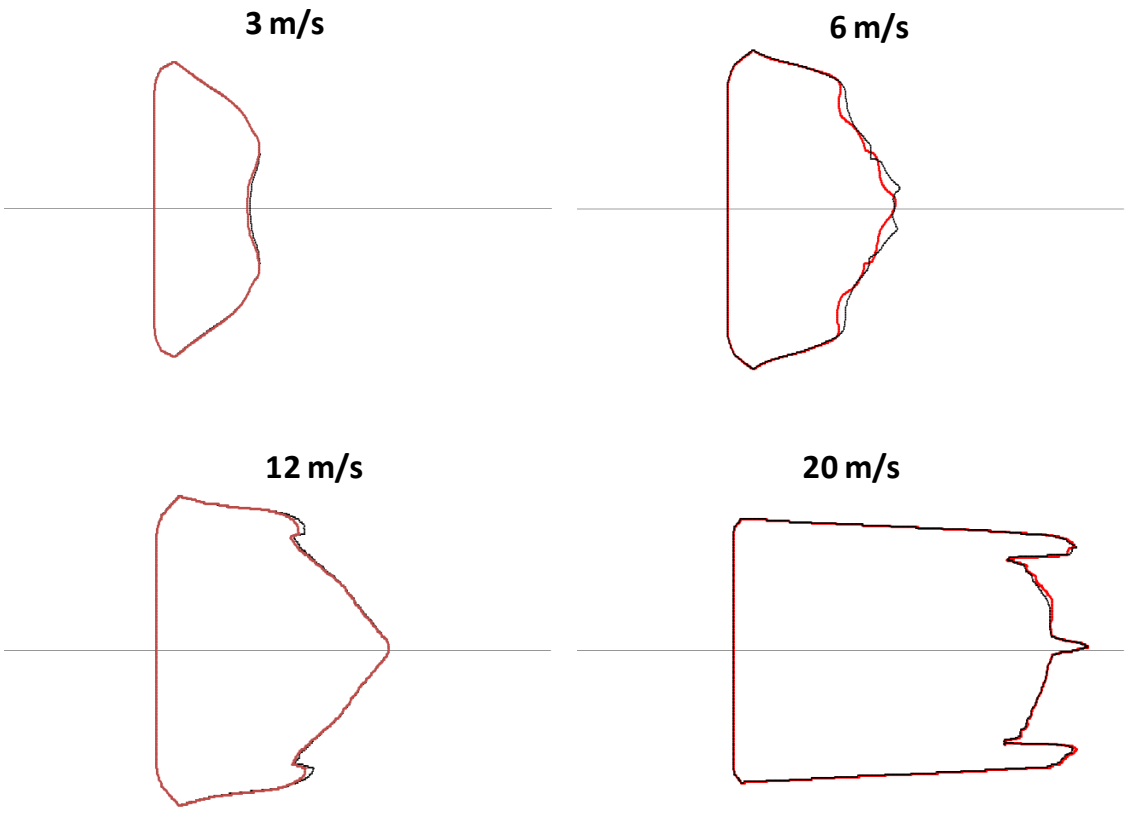

Figure 37: Comparison of fully-discrete (black) and quasi-discrete (red) burn areas at t = 1200 s at varying background wind speeds.

based nature of the fire model appears to be the primary culprit. Whereas a time step reduction is often required to stabilize the output of an atmospheric model acting alone, the opposite was true for ARPS/DEVS-FIRE in these tests because of the need to smooth errors resulting from distortion of the fire front in DEVS-FIRE. The implications of this finding are discussed in Chapter 5.

C. Verification using FIREFLUX data

Validation focused on the observations obtained from the 42 m main tower in the minutes following ignition. The observed and simulated 2 m and 10 m temperature time series are plotted in Fig. 38. All of the simulations did well at forecasting the arrival time of the combustion zone at the tower, with the quasi-discrete method improving the timing slightly. However, success at predicting temperature fluctuations was more mixed; distributing surface fluxes vertically resulted in substantial underprediction of the maximum temperatures observed over the fire front, while failing to do so resulted in substantial overprediction of the temperatures in the post-frontal zone.

Prediction of temperatures aloft was similarly mixed; Fig. 39 shows that applying the heat fluxes only at the surface improved the temperature forecast at 28 m somewhat but entirely failed to predict the impact of the main plume on the temperature 42 m, whereas vertical flux distribution contributed to overprediction of 28 m temperatures but was generally adequate at handling the timing and intensity of the plume at 42 m. This is confirmed by the 28 m and 42 m vertical velocities plotted in Fig. 40; while not distributing the surface fluxes produced marginally superior results at 28 m, the corresponding 42 m vertical velocity essentially oscillated around zero while the simulations employing vertical flux distribution approximated the average vertical velocity of the plumes fairly well.

Because quality-controlled measurements of specific humidity from the main tower are only available at 28 m AGL, vertical mixing of the latent heat from the fire

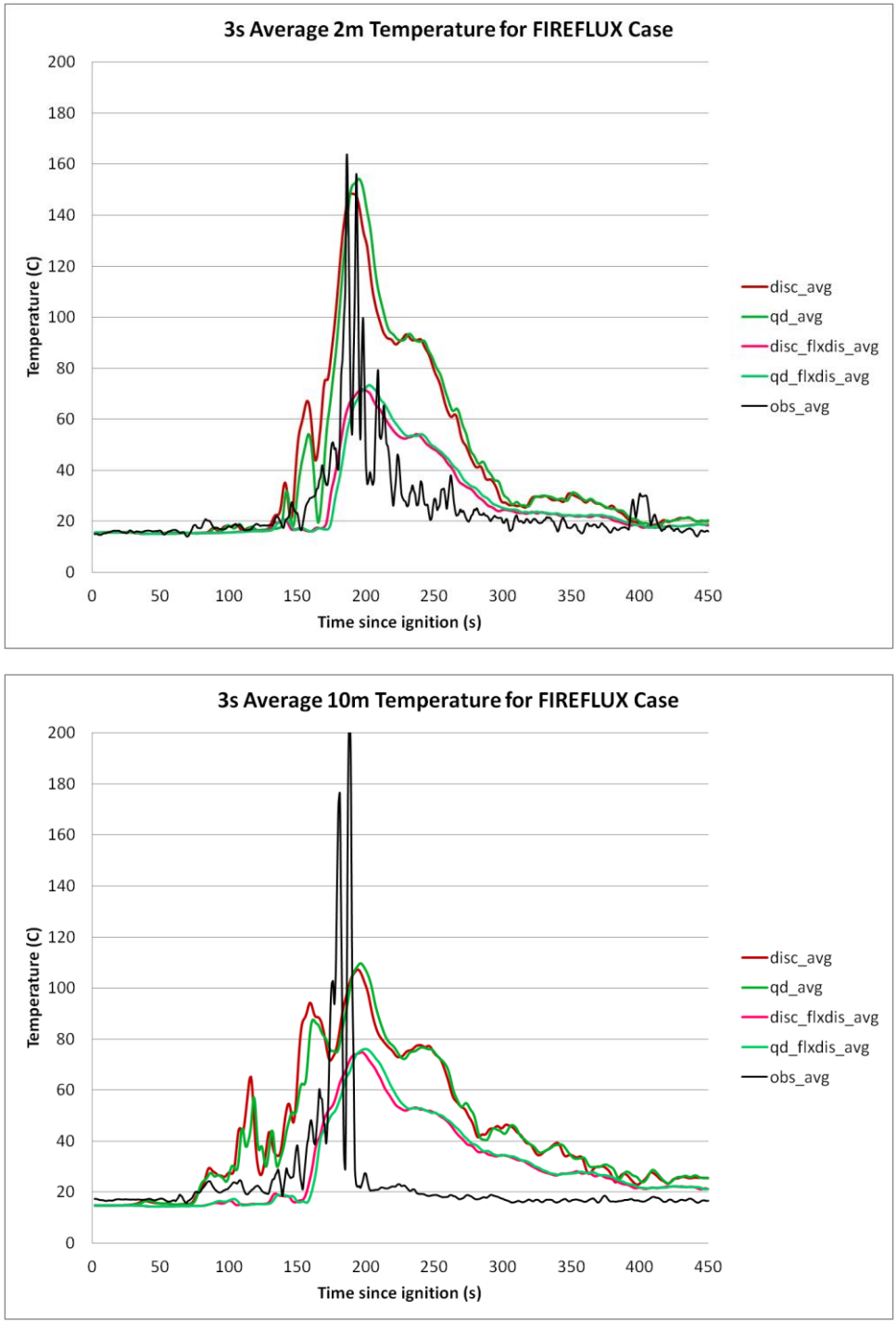

Figure 38: Observed and predicted 3-second average 2m (top) and 10 m (bottom) temperatures at the location of the main tower. "disc" denotes a fully-discrete simulation, "qd" denotes a quasi-discrete simulation, and "flxdis" indicates vertical disctribution of surface fluxes.

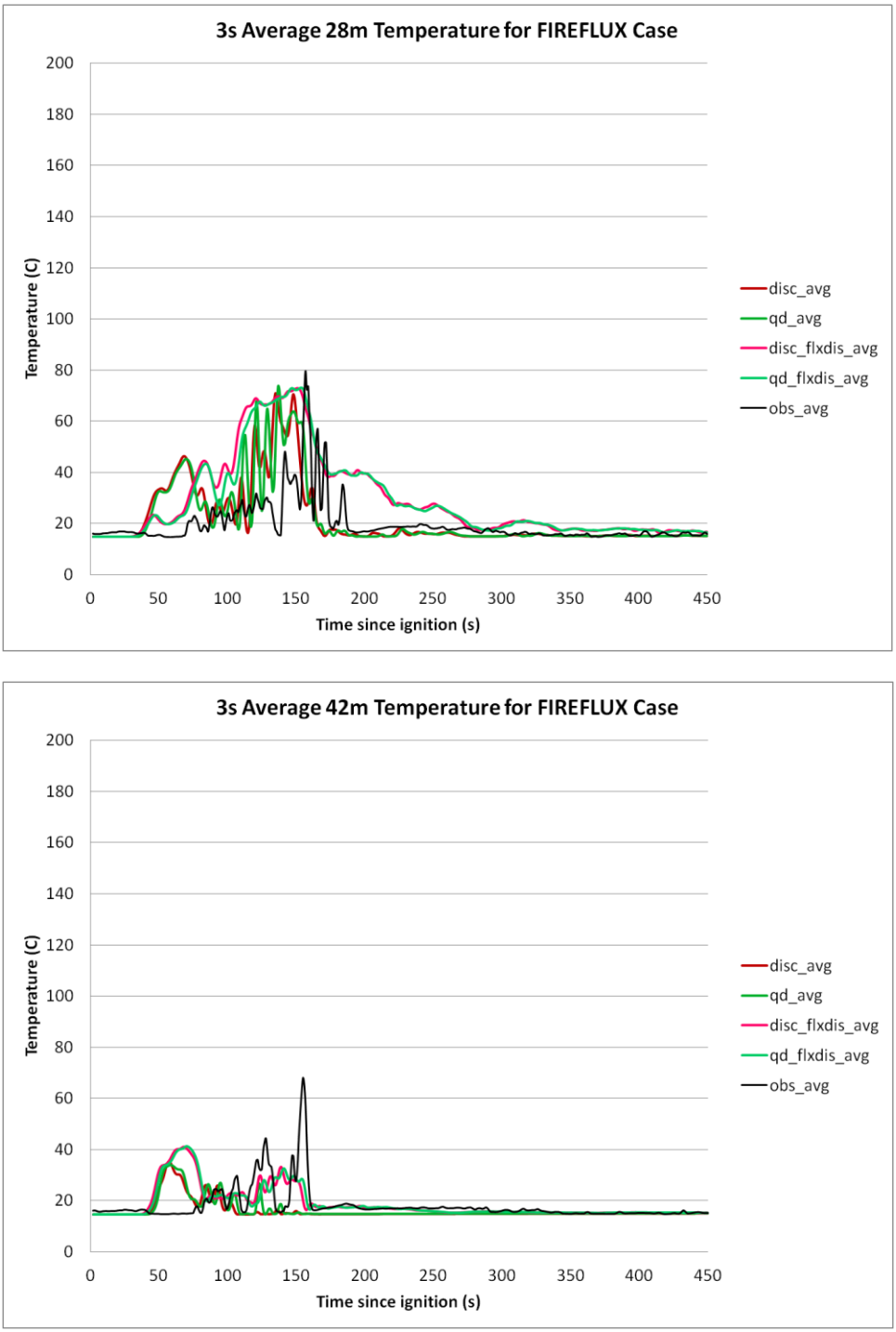

Figure 39: Same as Fig. 38, but at 28 m (top) and 42 m AGL (bottom) at the location of the main tower.

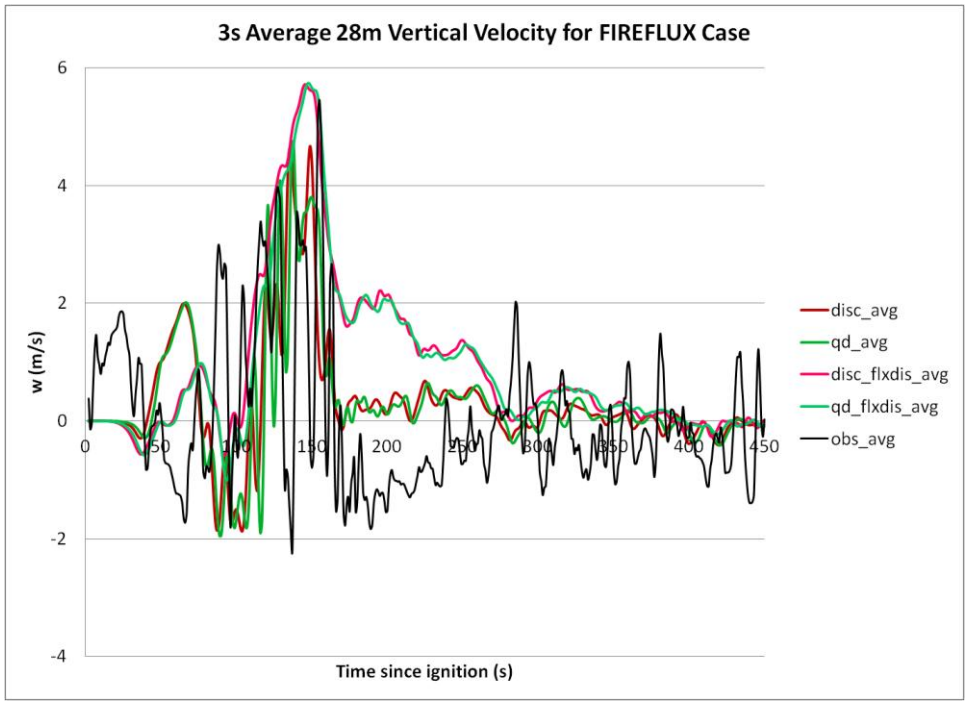

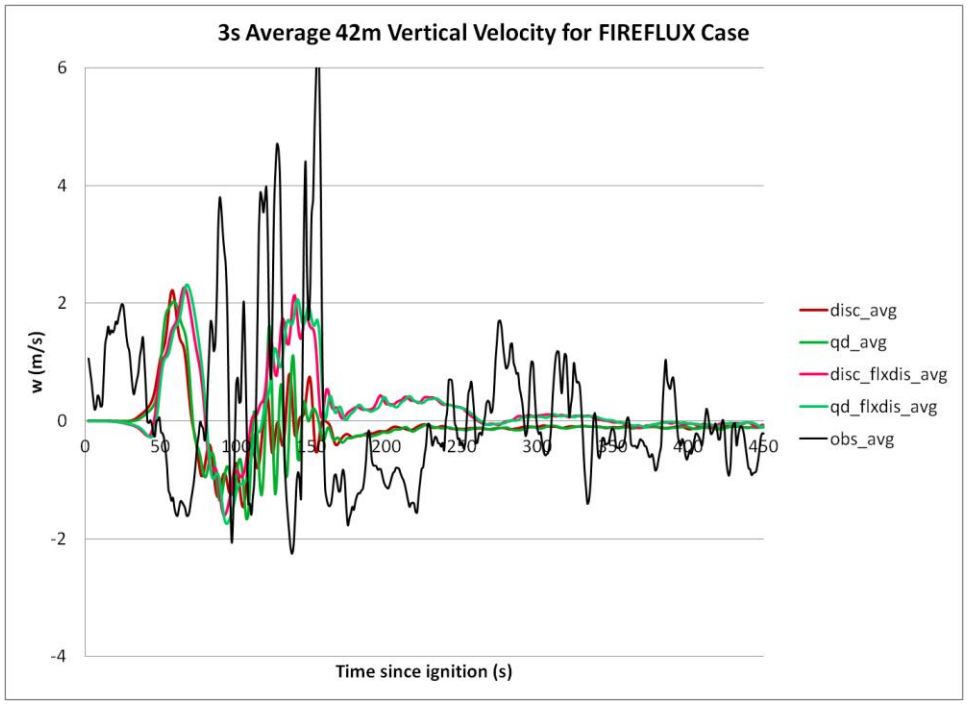

Figure 40: Same as Fig. 38, but for vertical velocity at 28 m (top) and 42 m AGL (bottom) at the location of the main tower.

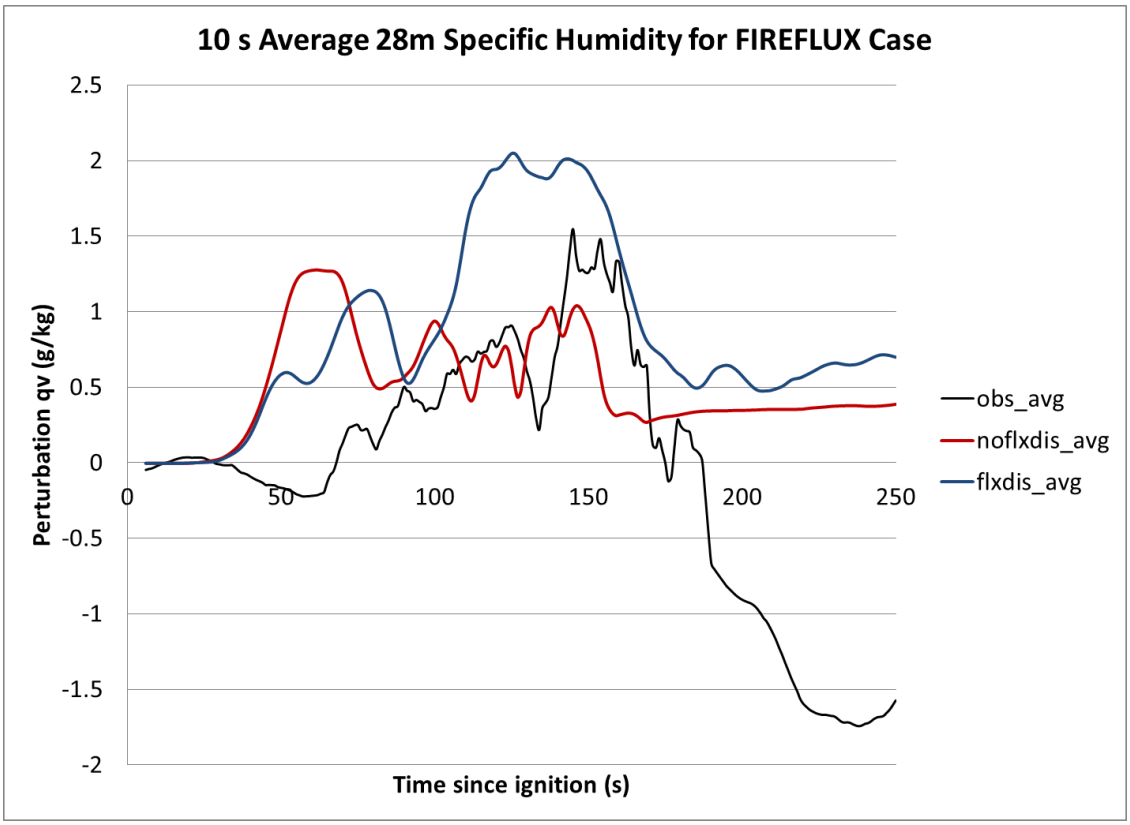

Figure 41: Observed (black) and simulated specific humidity with (blue) and without vertical surface flux distribution (red) at 28 m AGL at the main tower location for the FIREFLUX experiment.

cannot be evaluated as rigorously. Figure 41 shows the rolling 10-second average of observed perturbation specific humidity along with the simulated averages from the fully-discrete simulations with and without surface flux distribution. (The quasi-discrete results are not plotted due to their general similarity to the fully-discrete results, as shown in earlier figures.) It appears that the general magnitude and timing of the increased moisture within the plumes near the fire front were approximated rather well by the simulations without flux distribution but overestimated by the simulations with flux distribution, similar to the 28 m temperature results in Fig. 39. Given the association between temperature, moisture, and updraft speed shown in these figures, it

is speculated that the model depictions of moisture transport to 42 m AGL would reflect more favorably on the method employing vertical flux distribution; unfortunately, this cannot be verified because the main tower humidity observations from levels other than 28 m AGL were considered useless due to infrared contamination. The 28 m measurements also showed signs of contamination (e.g. the apparent rapid local drying to below ambient moisture levels depicted in Fig. 41 in the wake of the main plume), although the observations ahead of and within the main plume generally conformed with observations from the downstream tethersonde system (Craig Clements, personal communication) and were therefore deemed adequate for obtaining at least an approximation of the actual conditions.

It should be noted that these plots indicate a predicted plume structure tilted downstream from the fire front, with peak temperatures/updraft speeds observed earlier at higher altitudes. Qualitatively, this matches the observations as well as the uncoupled simulations detailed in section A. The coupled behavior associated with the tilted plume is illustrated by the fluctuations in horizontal wind speed at 2 m and 10 m AGL plotted in Fig. 42, with pronounced strengthening coinciding with the arrival of the fire front. However, it is also clear from Fig. 42 that all of the simulations chronically overpredicted the 2 m and 10 m wind speeds before and after fire front passage (although, interestingly, the predicted wind speeds during passage agreed well with observations). The most likely cause of this is not a deficiency of the coupled model, but rather a misspecification of the roughness length used in ARPS. (As in Mandel et al., 2011, a roughess length z_o = 0.02 m was specified based on the background wind profile; however, with a fuel bed depth in excess of 1 m, this is likely

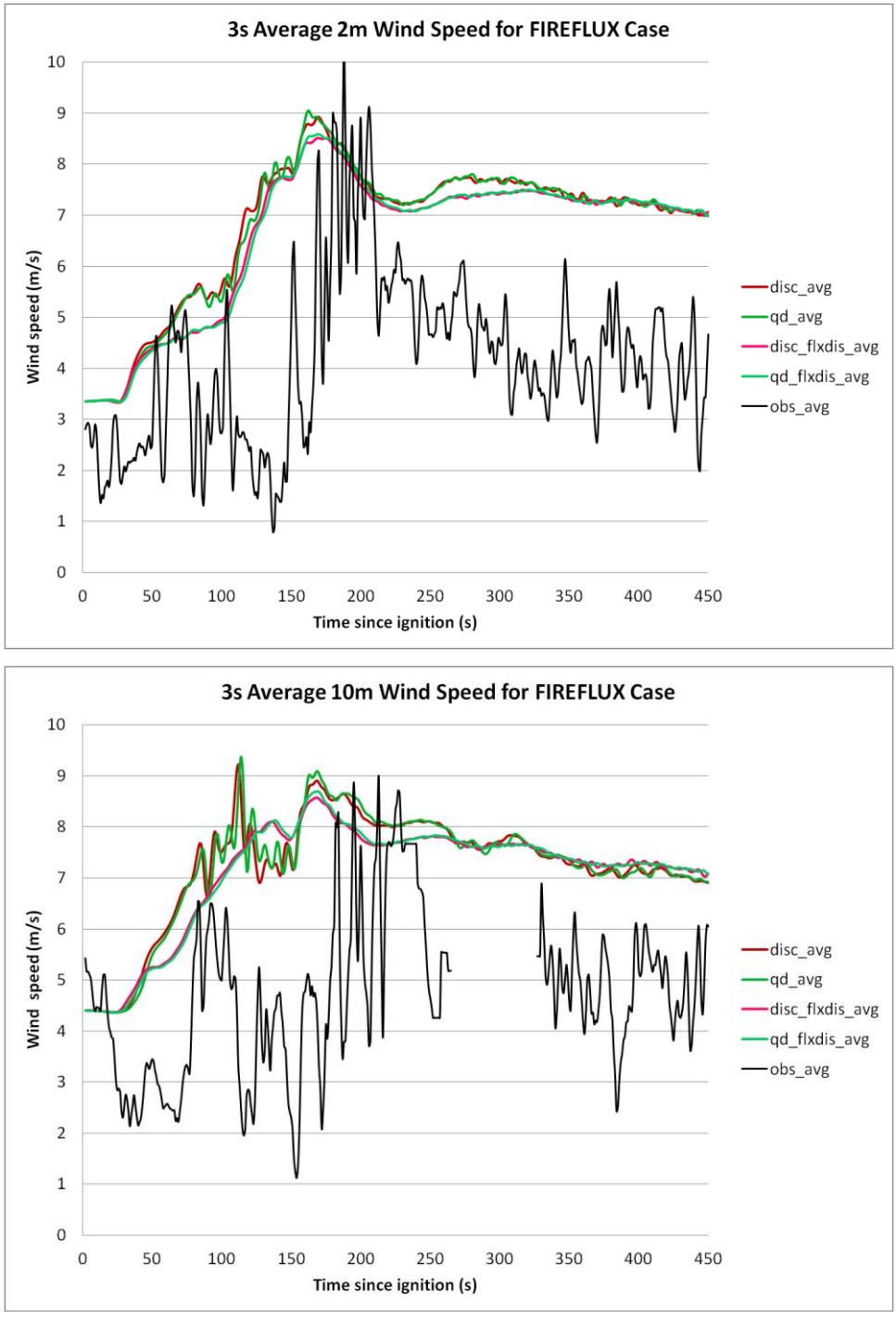

Figure 42: Same as Fig. 37, but for horizontal wind speed at 2 m (top) and 10 m AGL (bottom) at the location of the main tower.

an underestimate.) Considering the general quality of the results, however, a subsequent attempt at "tuning" the roughness length was not attempted.

Partitioning the estimated radiative and ground heat fluxes from the "bulk" sensible heat flux had no significant impact, producing results generally indistinguishable from those of the quasi-discrete simulation using only "bulk" sensible heat flux. (Due to the lack of distinction, that simulation was not included in the plots for Figs. 38 through 42.) In hindsight, this should have been expected simply becauseof the relative magnitudes of the radiative flux (~ 50 kW m^{-2} for a peak temperature near 1000 K and assuming the fuel radiates as a blackbody) and "bulk" sensible heat flux (~ 1 MW m^2 during peak combustion). However, it is interesting to note from Fig. 43 that the temperature predicted by the estimation method agreed well with the surface fuel temperature beneath the main tower during both the initial approach and the smoldering phases. It is clear that the peak temperature was substantially underestimated, suggesting possible misspecification of the Arrhenius coefficients *A* and *E* applied to (31). (This possibility is reinforced by the general disagreement on correct values in the literature as noted in Sinha et al., 2000.) Nevertheless, the general character of the curve provides supporting evidence of the accuracy of the simple exponential decay combustion model used in this study.

Despite the errors noted, these results suggest that the atmospheric response to intense surface heating associated with a wildfire of this sort is generally replicated adequately by ARPS for purposes associated with coupled fire spread modeling. For larger fires spreading over lengthier periods of time, accurate fine-scale depiction of processes within the narrow combustion zone is not computationally

tractable and the focus shifts to broader-scale feedbacks and more general depictions of fire spread. In such cases, these results suggest that vertical flux distribution should be employed; therefore, quadratic distributions over the lowest 10 m of the atmosphere were also specified for the Moore Branch and Rock House cases described in the next section.

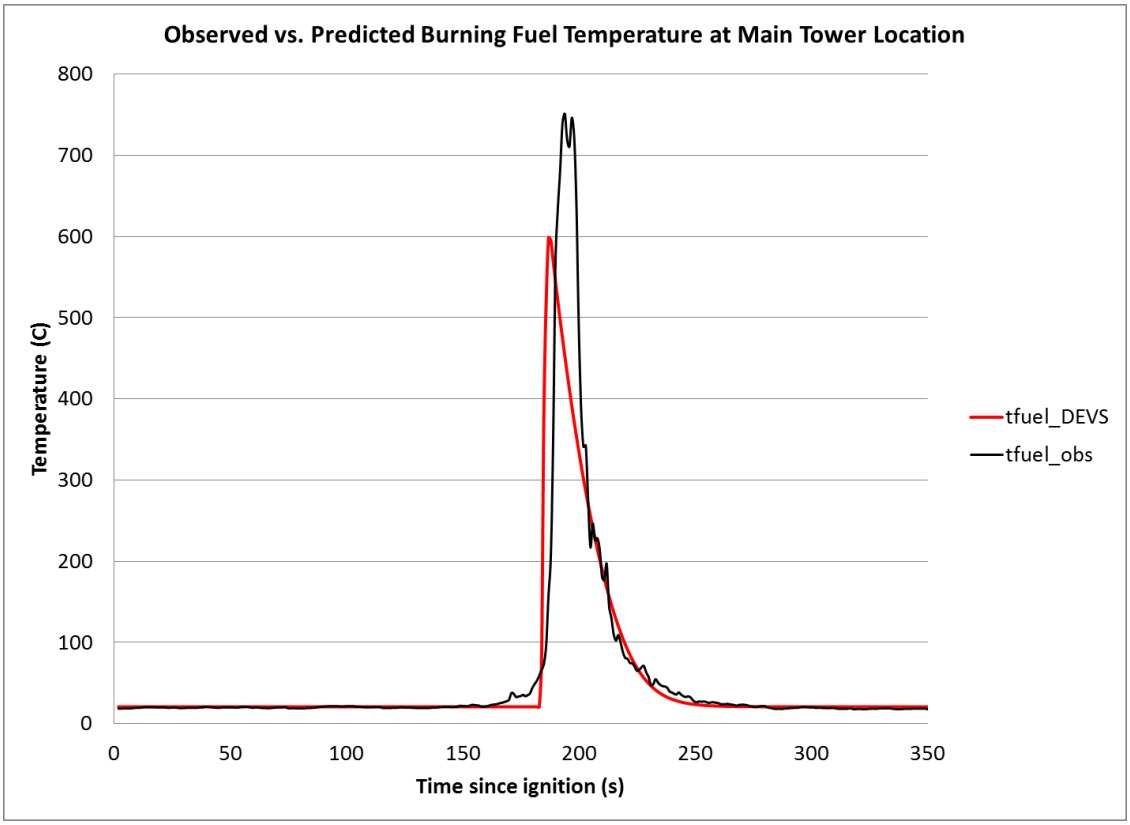

Figure 43: Comparison of observed fuel temperature (black) with fuel temperature estimated as described in Chapter 3 for quasi-discrete DEVS-FIRE.

D. Case Studies: the Moore Branch and Rock House Fires

Figure 44 shows the uncoupled 24-hour DEVS-FIRE test for Day 5 of the Moore Fire using the maximum wind speed and direction from Kirbyville (9.9 m s^{-1} at 33^0,

held constant) for the background conditions. From Table 5, it is evident that this method greatly overestimated the actual background wind speed, particularly earlier in the period. Knowing this, the similarity of the simulated and observed burn areas is surprising, with only limited overestimation of the burn area extent in the expected direction of maximum spread (i.e. south-southwest).

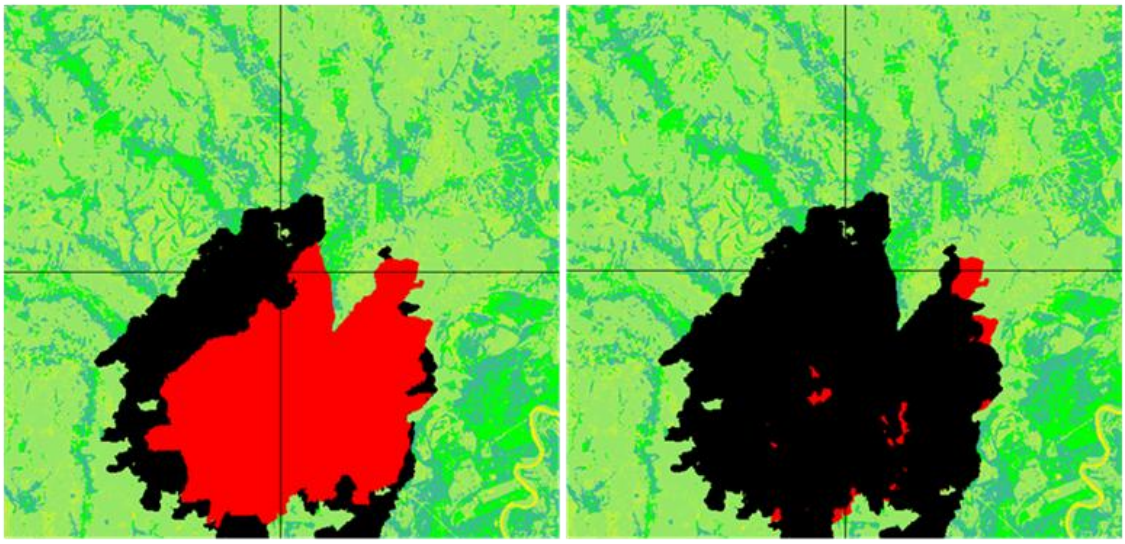

Figure 44: Moore Branch Day 5 observed burn area (red) and predicted burn area using Kirbyville data (black).

The possibility that wildfire-atmosphere feedbacks consistently and substantially amplified fire spread throughout the period is confirmed by Fig. 45, which compares the result of the uncoupled DEVS-FIRE test using the background conditions in Table 5 to the result using the coupled model operating at 60 m resolution. As shown in Fig. 46, whereas the eastern portion of the initial fire front stagnated in the uncoupled simulation due to the background winds being weak initially (and generally parallel to the front during the day), coupling the models greatly enhanced the across-fire

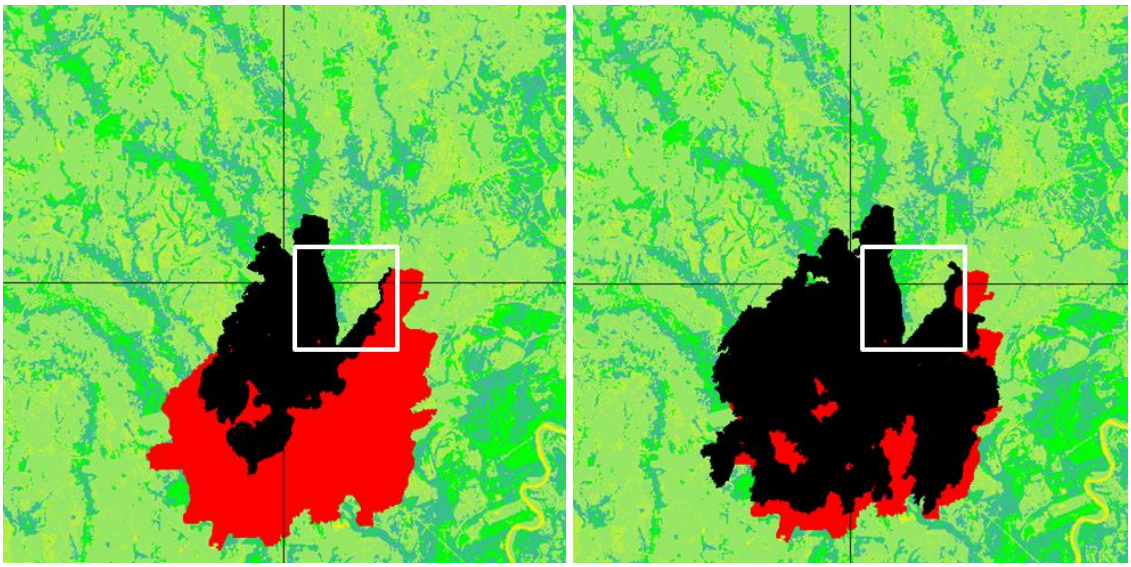

Figure 45: Same as Fig. 44, but for uncoupled burn area using background conditions interpolated from reanalysis data (left) and coupled burn area using 60 m resolution in ARPS. White squares indicate zoomed region plotted in Fig. 44.

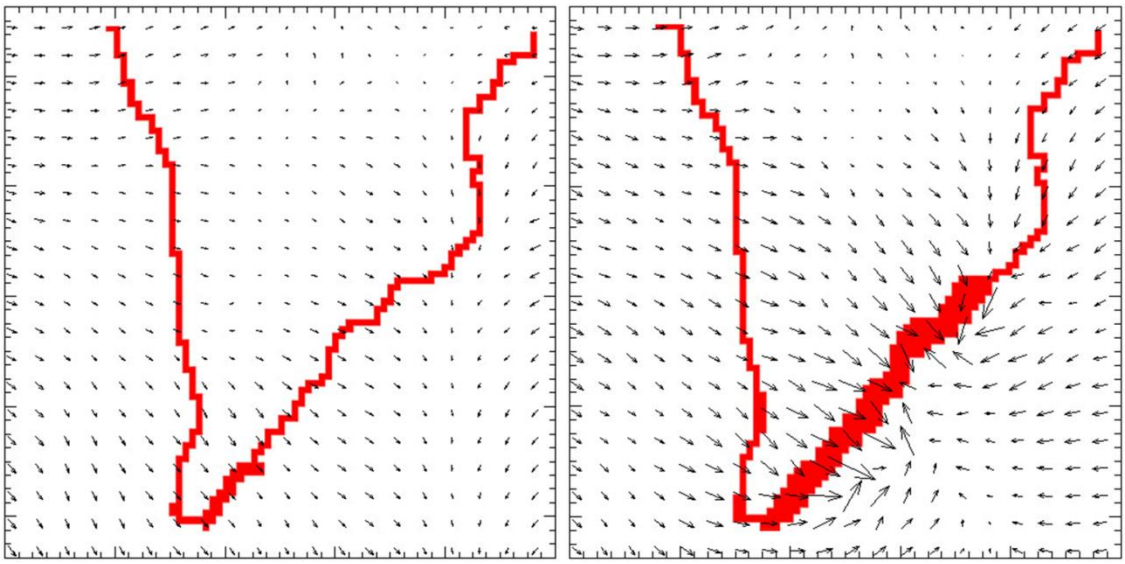

Figure 46: Fire front position (red) and perturbation winds (arrows) for reanalysis-based uncoupled test (left) and coupled test with ARPS resolution 60 m (right) at t = 40 min. Zoomed view corresponds to white boxes in Fig. 43.

component of the winds in this area, producing a burn area that agrees very well with observations. (The cause of the large "false alarm" region on the northwest side of the burn area is unclear, although it may be attributable to firefighting efforts preventing spread toward Newton. Without documentation of such efforts, there was no way for DEVS-FIRE to account for this possibility.)

To assess the sensitivity of the coupled result to ARPS grid spacing, additional coupled tests were run at resolutions of 150, 300, and 1200 m. Surprisingly, as shown in Fig. 47, decreasing the resolution by up to a factor of five did not negatively impact the skill of the forecast. In fact, as shown in Table 7, the skill scores were actually higher for the 150 m and 300 m tests. As expected, the choice of resolution demonstrably affected the extent and robustness of smaller-scale feedbacks (e.g. note the fingers developing in the northwest quadrant of the higher-resolution simulations in Fig. 48). However, these differences appear to have been transient, with the ultimate extent of the burn area largely unaffected. A similar lack of sensitivity to weather model resolution was noted when using WRF-SFIRE to replicate large wildfires in complex terrain (Jan Mandel and Adam Kochanski, personal communication).

Deleterious effects of increasing the spatial averaging of the heat flux from DEVS-FIRE and the degree of interpolation applied to the weather conditions from ARPS were not seen until the 1200 m test, at which point the impact of coupling was noticeably weakened (although still not eradicated). As shown by Figure 49, increasing the grid spacing generally produced lower perturbation temperatures spread over a larger area near the fire front. The additional impact of shifting to 1200 m resolution was two-fold: (1) the coarser resolution could not resolve the shape of the initial fire

front (essentially a "V" shape 2 km across) and thus could not produce the local modifications shown in Figure 46; and (2) the change in resolution brought the model into the mesoscale regime, for which the Moeng and Wyngaard TKE scheme was not intended. (Evgeni Fedorovich, personal communication) This unrealistically limited vertical mixing, reducing the efficiency of plume development and the onset of coupled feedbacks. (For a closer look at impacts of using the Moeng and Wyngaard scheme at mesoscale resolutions in the presence of enhanced surface heating, see Appendix C.)

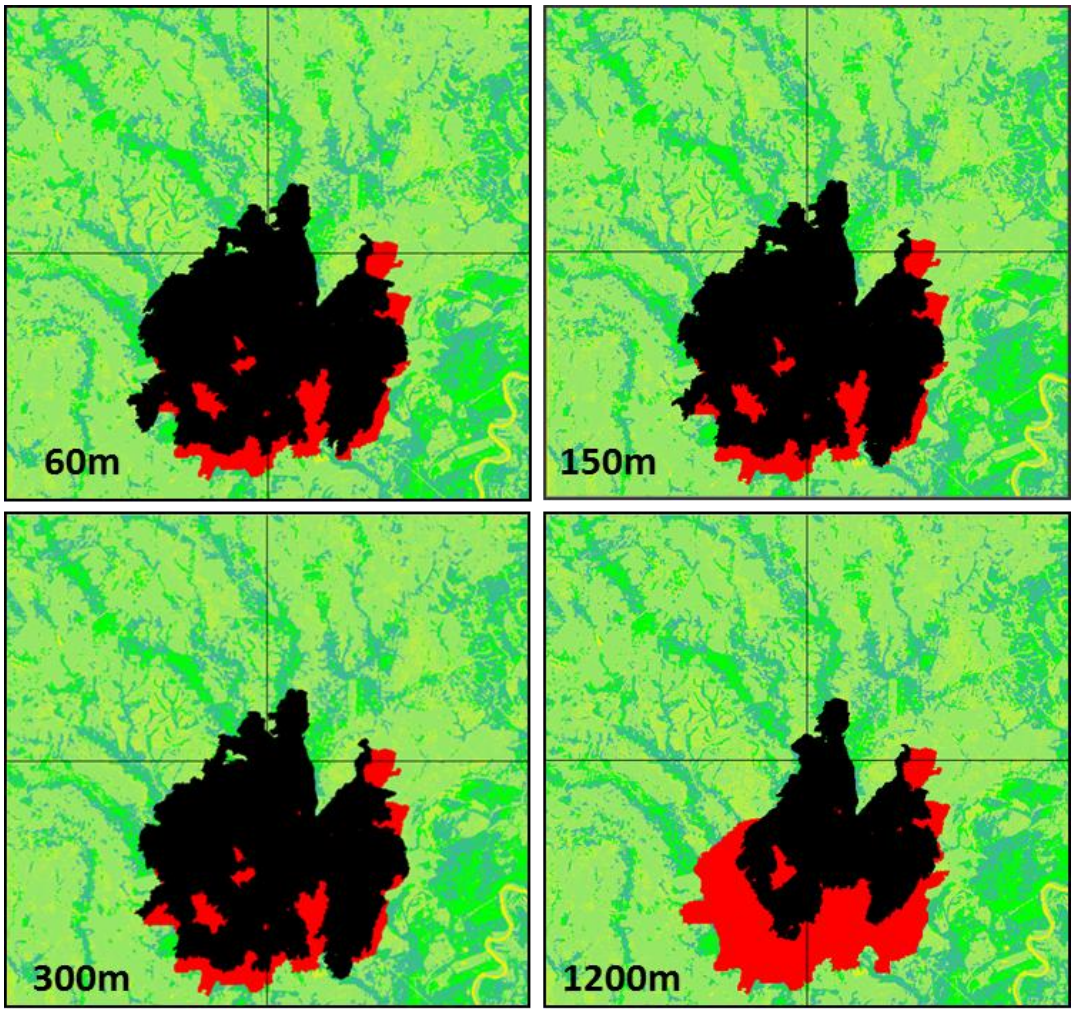

Figure 47: Comparison of coupled Day 5 burn results for ARPS resolutions of 60 (upper left), 150 (upper right), 300 (lower left), and 1200 m (lower right), plotted as in Fig. 42.

Table 7: Skill evaluation for Moore Branch simulations

Test Specification	False Alarm Rate	Critical Success Index	Heidke Skill Score
Uncoupled, NARR data	0.037	0.283	0.345
Uncoupled, Kirbyville data	0.202	0.584	0.626
Coupled, 60m ARPS res	0.093	0.624	0.689
Coupled, 150m ARPS res	0.089	0.638	0.703
Coupled, 300m ARPS res	0.087	0.642	0.708
Coupled, 1200m ARPS res	0.021	0.490	0.582

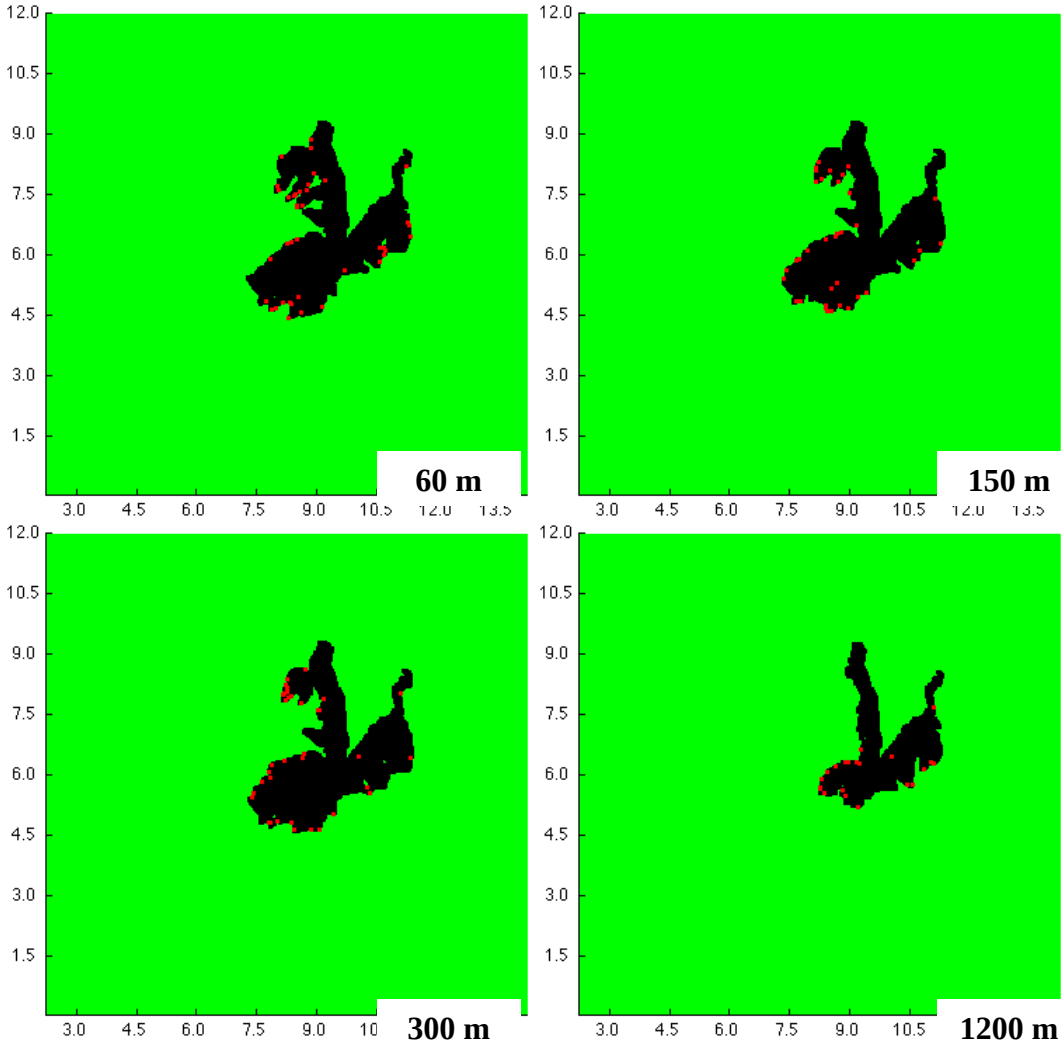

Figure 48: Burn areas at t = 12 h for coupled Moore Branch simulations at varying ARPS resolutions. Green indicates unburned fuel, red indicates cells ignited within the past 60 s, and black indicates previously-burned fuel. Distances (in km) from the grid origin are indicated on the *x* and *y* axes.

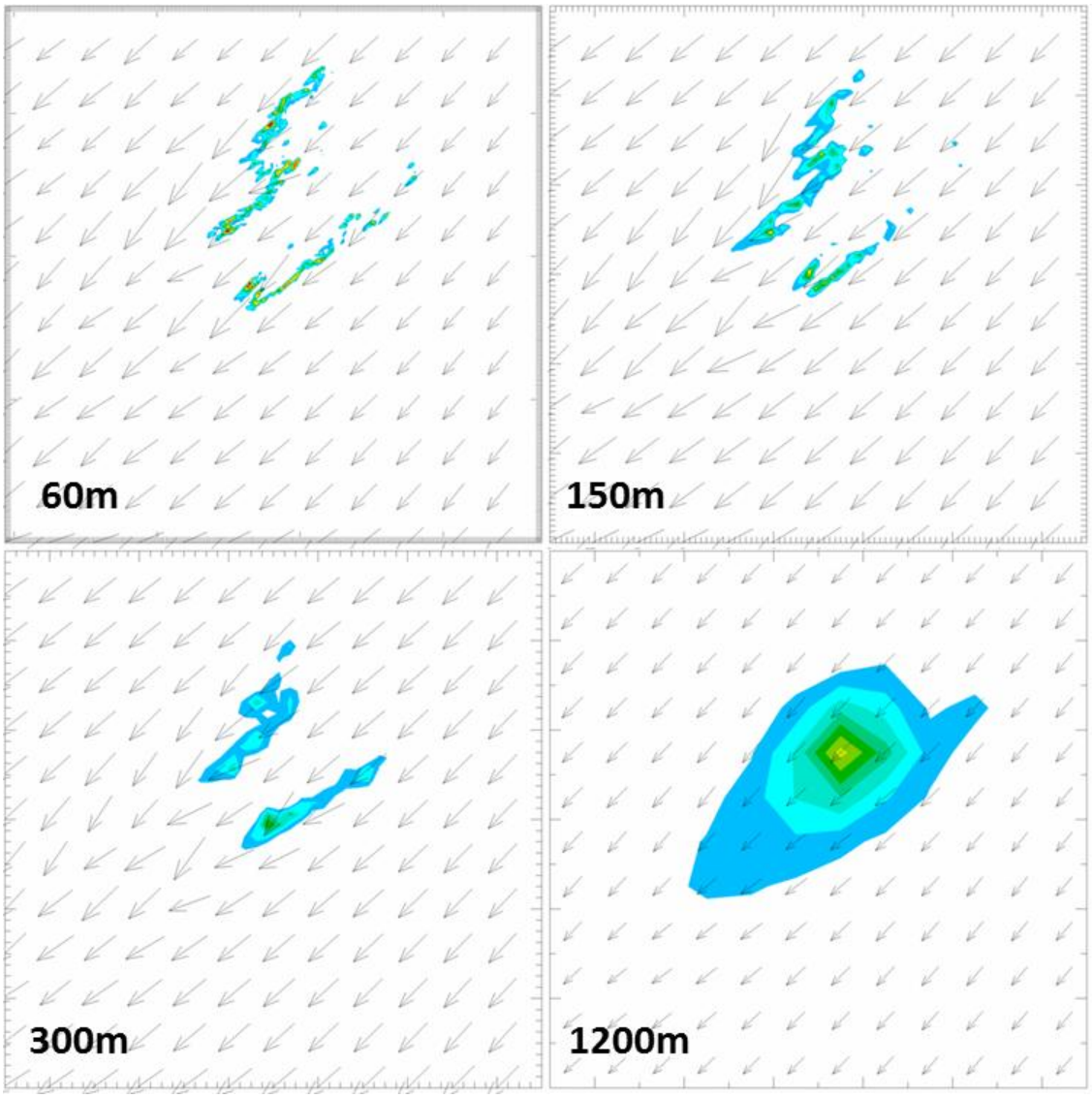

Figure 49: 6 m positive perturbation temperatures (color fills) and winds (arrows) at t = 12 h for coupled Moore Branch simulations at varying ARPS resolutions.

Nevertheless, since the coupled model is intended to address microscale feedbacks and therefore is meant to run within the LES regime, ARPS/DEVS-FIRE demonstrated a high degree of skill for the Moore Branch case when used appropriately. Unfortunately, this performance did not carry over to the Rock House fire. Figure 50 shows that ARPS/DEVS-FIRE was outperformed by the uncoupled

FARSITE model in this case, and that neither model captured the extent of the 6-hour fire spread well at all. One possible cause is a shortcoming of the use of standard fuel types; Martin (2011) notes that the observed spread is outside of the maximum capabilities of the standard fuel map for the region (predominantly grass and understory, i.e. fuel type 2 from Anderson, 1982). Only by artificially mapping faster-burning fuels to the grid was Martin able to replicate the observed burn area.

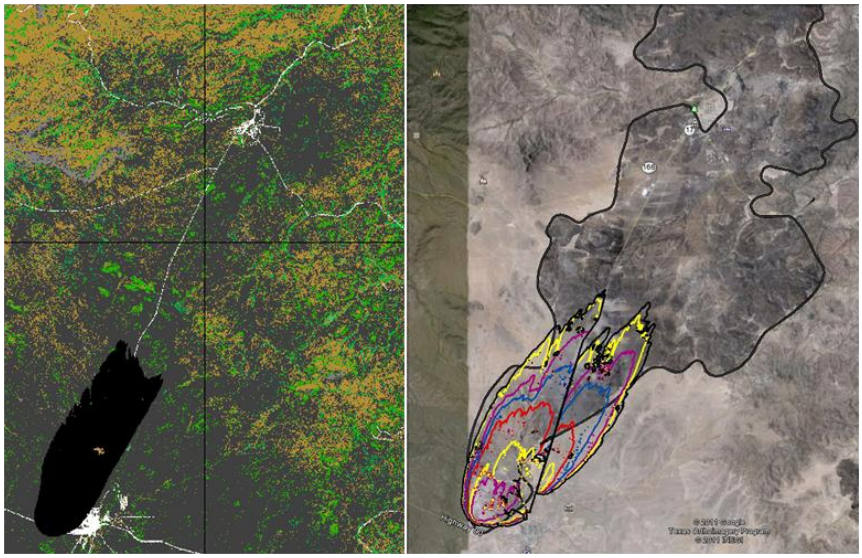

Figure 50: Simulated 6-hour burn areas from ARPS/DEVS-FIRE (left) and FARSITE (right, reproduced from Fig. 23) for the Rock House fire. Observed 6-hour burn area is shown in grey at right.

However, a primary cause for ARPS/DEVS-FIRE's lack of skill in this case appeared to be its representation of fire spread mechanisms. As noted previously, the background wind for the Rock House fire was quite strong (sustained at 15 m s^{-1}, gusting to 25 m s^{-1}); with brush and sparse timber included in the burn area, lofting of firebrands was a significant contributor to the overall progress of the fire. While such

behavior cannot be explicitly depicted, operational models generally employ stochastic methods to ignite areas ahead of the main fire front where the combined probability of burning material being lofted the specified distance and the probability of it landing in combustible (i.e. pre-dried) fuel exceeds a certain threshold. (Indeed, the "spotting" parameter in FARSITE was increased by nearly a factor of two from its default value in order to obtain the final results reported in Martin, 2011.) The current version of DEVS-FIRE treats fire spread purely as a progression from a cell to its immediate neighbors, on the other hand, and a "spotting" capability needs to be implemented in order for it to properly treat high-wind cases of this sort, whether or not it is coupled with an atmospheric model.

CHAPTER 5

CONCLUSIONS AND TOPICS FOR FUTURE STUDY

The results obtained with the coupled ARPS/DEVS-FIRE model in this study are decidedly mixed. On the one hand, the results of the uncoupled ARPS tests and the FIREFLUX simulations suggest that the parameterizations currently used to transfer heat from the fire into the atmosphere are sufficiently accurate to enable ARPS to produce reasonable approximations of high-resolution atmospheric response. Furthermore, the degree of temporal smoothing applied by a 60-second update interval appears to curtail error growth in idealized small-scale tests while still allowing sufficient feedback to produce distinct improvement in the fire spread forecast for the Moore Branch case.

However, deficiencies are clearly evident that cast considerable doubt on the model's reliability and current capabilities. The quality of the high-resolution atmospheric results from the FIREFLUX tests is partially negated by the idealized results showing that coupled fire spread prediction at high temporal resolution is highly sensitive to the sorts of fire front distortions to which DEVS-FIRE is inherently prone. This is particularly true in cases with high winds and/or quick-burning fuels, which (unfortunately) are cases in which a particularly high degree of decision-making assistance would be required for optimizing firefighting efforts. Moreover, the artifacts produced by these distortions closely mimic actual phenomena (in particular, the growth of dynamic "fingers") that pose considerable danger to firefighters; thus, the

reliability of predicting a feature of particular interest to safety managers is specifically precluded by the flaws of the DEVS-FIRE algorithm.

It is clear that efforts to refine the heat release through the quasi-discrete method had essentially a negligible impact on model accuracy for the resolutions tested here. This may be partially attributed to the fact that this method has the greatest positive impact for fire spread in cardinal directions (see Figs. 19 and 20), and therefore is of comparatively little assistance in the angular portions of the fire front where errors due to distortion predominate. Furthermore, the difference between the heat released by the discrete and quasi-discrete versions diminishes as spread rate increases; this means that fast-spread cases, which are the most prone to error, are also the least affected by the choice of heat release calculation method.

The quasi-discrete method did improve the initial spread rate forecast for the FIREFLUX tests slightly (similar to the report of Mandel et al., 2011, indicating that a gradual "drip torch" ignition method was required to prevent the initial fire from spreading too quickly). However, since only the temporally-smoothed version of ARPS/DEVS-FIRE appears justified for further use, and since temporal smoothing also reduces the difference between the discrete and quasi-discrete heat outputs, this distinction seems to be moot. Even laying this point aside, the benefit to model accuracy may well be too slight to justify the increase in computational expense. (Compare (25) to (28) and (29).)

Further study along this line should focus on determining whether the quasi-discrete version of the model is significantly more robust than the discrete version to

changes in grid resolution. This is particularly relevant because the current version of DEVS-FIRE is not parallelizable; even with the comparative efficiency of the cellular automaton approach, the computational speed of the current versions of DEVS-FIRE slows down as fire fronts enlarge on high-resolution grids, simply due to the fact that the number of "active" cells at any point in time increases exponentially as the grid spacing decreases. The fact that DEVS-FIRE and ARPS currently run separately adds to the computational load as well, since a higher resolution means a larger amount of data that DEVS-FIRE must read from ARPS (and write to ARPS) at every update time.

Typically, the speed of the weather model is the major factor limiting the speed of the coupled model. However, in the tests described in the study for which the DEVS-FIRE resolution was 10 m or less, the opposite became true after several minutes. Whereas the 30 m Moore Branch 24-hour results could be obtained in approximately 12 hours, the 10 m idealized 30-minute simulations often required 2 hours or more to complete, and the 3 m simulations were only able to complete 10 minutes or less before the requested 4-hour allotment on the supercomputer ran out. Therefore, simply using a very fine grid mesh to refine heat output and make the fire front smoother is not currently feasible.

Even in the Moore Branch case, the coupled model performance was clearly too slow to provide a useful forecast; by comparison, a 72-hour simulation of a wildfire of comparable size by WRF-SFIRE completed in approximately 4 hours. (Adam Kochanski, personal communication) Here, the external exchange of data required by the current algorithm (see Fig. 17) appeared to be a key contributor; with the model grid encompassing the entire Day 5 burn area, each update step generally required up to

five seconds to complete. Furthermore, external reading and writing performance suffers on the supercomputing clusters used for this work (see Acknowledgements) when system load is high. Thus, the time required to complete a given simulation varied widely from the run times described above. For reliable performance, it is crucial that the coupled model be updated to enable DEVS-FIRE to run within ARPS in order to avoid external I/O as much as possible.

Finally, even if the coupled model is confined to larger-scale simulations and/or slower-burning fuels so that DEVS-FIRE can justifiably be used, additional upgrades to the capabilities of DEVS-FIRE are required. The previously-described slowdowns and the results from the Rock House test clearly illustrate that parallelization and the implementation of a "spotting" algorithm to account for lofted firebrands are paramount. If higher-resolution treatment of atmosphere-wildfire feedbacks is desired, either the degrees of freedom in the fire spread model must also be increased substantially to reduce distortion (as in BFOLDS; see Fig. 5) or some other method must be found to smooth the effective shape of the fire front. However, such methods immediately suggest a transition to a vector-based methodology and, with the gain in efficiency from the raster-based approach tempered by the overriding cost of operating the weather model at the desired resolution, implementing them in DEVS-FIRE may not be an efficient or advisable course of action.

References

Albini, F.A., 1976: *Estimating wildfire behavior and effects*. USDA For. Serv. Gen. Tech. Rep. INT-30. ONLINE. Available: http://www.fs.fed.us/ rm/pubs_int/ int_gtr030.pdf [4 April 2014]

Albini, F.A., and E.D. Reinhardt, 1995: Modeling ignition and burning rate of large woody natural fuels. *Int. J. Wildland Fire* **5**(2): 81-91

Anderson, H.E., 1982: *Aids to determining fuel models for estimating fire behavior*. USDA For. Serv. Gen. Tech. Rep. INT-122. ONLINE. Available: http://www.fs.fed.us/rm/pubs_int/int_gtr122.html. [10 March 2014]

------, 1983: *Predicting Wind-Driven Wild Land Fire Size and Shape*. USDA For. Serv. Res. Pap. INT-305. ONLINE: Available: http://www.firemodels.org/ downloads/behaveplus/publications/Anderson_INT-305_1983_ocr.pdf [3 March 2014]

Andrews, P.L., 2012: *Modeling wind adjustment factor and midflame wind speed for Rothermel's surface fire spread model*. USDA For. Serv. Gen. Tech. Rep. RMRS-GTR-266. 39 pp.

------, 2014: Current status and future needs of the BehavePlus Fire Modeling System. *Int. J. Wildland Fire* **23**: 21-33

Byram, G.M., 1959: Combustion of forest fuels. *Forest Fire Control and Use*, Kenneth P. Davis, ed. McGraw-Hill Book Co., New York. pp. 61-89

Chan, R.W.C., and B.B. Krieger, 1982: Analysis of Chemical and Physical Processes During Devolatilization of a Single, Large Particle of Wood. *Seventh International Symposium on Chemical Reaction Engineering*, Boston, MA

Clark, T.L., J.L. Coen, and D. Latham, 2004: Description of a coupled atmosphere-fire model. *Int. J. Wildland Fire* **13**: 49-63

Clark, T.L., M.A. Jenkins, J. Coen, and D. Packham, 1996a: A Coupled Atmosphere-Fire Model: Convective Feedback on Fire-Line Dyanmics. *J. Appl. Meteor.* 35: 875-901

------, 1996b: A Coupled Atmosphere-Fire Model: Role of the Convective Froue Number on Dynamic Fingering. *Int. J. Wildland Fire* **6**(4): 177-190

Clarke, K.C., J.A. Brass, and P.J. Riggan, 1994: A cellular automaton model of wildfire propagation and extinction. *Photogrammetric Eng. and Remote Sensing* **60**(11):1355-1367.

Cliff, E.P., J.H. Price, C.O. Lindh, L.K. Mays, and H.D. Cochran, 1953: *The Rattlesnake Fire: July 9, 1953*. U.S. Department of Agriculture Board of Review. ONLINE. Available: http://www.fireleadership.gov/toolbox/staffride/downloads/lsr2/lsr2_resource4.pdf [17 Feb 2014]

Cui, W., and A.H. Perera, 2008: *A study of simulation errors caused by algorithms of forest fire growth models*. Ont. For. Res. Instit., Sault Ste. Marie, ON, For. Res. Rep. No. 167. 17 p.

Cunningham, P., and R.R. Linn, 2007: Numerical simulations of grass fires using a coupled atmosphere-fire model: Dynamics of fire spread. *J. Geophys. Res.* **112**,D05108, doi: 10.1029/2006JD007638

Emori, R.I., and K. Saito, 1983: A study of scaling laws in pool and crib fires. *Combustion Science and Technology* **31**(5-6): 217-231

Filippi, J.-B., F. Bosseur, X. Pialat, P.-A. Santoni, S. Strada, and C. Mai, 2011: Simulation of Coupled Fire/Atmosphere Interaction with the MesoNH-ForeFire Models. *Journal of Combustion* **2011**(540390): 13 pp. ONLINE. Available: http://www.hindawi.com/journals/jc/2011/540390/ [12 April 2014]

Finney, M.A., 1998: *FARSITE: Fire Area Simulator – Model Development and Evaluation*. USDA For. Serv. Res. Pap. RMRS-RP-4. ONLINE. Available: http://nature.berkeley.edu/stephens-lab/fireareaall.pdf [1 March 2014]

Frandsen, W.H., 1971: Fire spread through porous fuels from the conservation of energy. *Combust. and Flame* **16**: 9-16.

Gu, F., X. Hu, and L. Ntaimo, 2008: Towards validation of DEVS-FIRE wildfire simulation model. *Proceedings of the 2008 High Performance Computing and Simulation Symposium*, 355-361

IPCC, 2007: *Climate Change 2007: Impacts, Adaptation, and Vulnerability. Contribution of Working Group II to the Fourth Assessment Report of the Intergovernmental Panel on Climate Change*. M.L. Parry, O.F. Canziani, J.P. Palutikof, P.J. van der Linden, and C.E. Hanson, Eds., Cabridge University Press, Cambridge, UK, 976 pp.

Keane, R.E., J.K. Agee, P. Fulé, J.E. Keeley, C. Key, S.G. Kitchen, R. Miller, and L.A. Schulte, 2008: Ecological effects of large fires on US landscapes: benefit or catastrophe? *Int. J. Wildland Fire* **17**:696–712.

Kessler, E., 1969: *On the Distribution and Continuity of Water Substance in Atmospheric Circulations*, 84 pp.

Kiefer, M.T., Y.-L. Lin, and J.J. Charney, 2008: A Study of Two-Dimensional Dry Convective Plume Modes with Variable Critical Level Height. *J. Atmos. Sci.* **65:** 448-469

Klemp J.B., and R.B. Wilhelmson, 1978: The simulation of three-dimensional convective storm dynamics. *J. Atmos. Sci.* **35**:1070-1096

Limpasuvan, V., D. L. Wu, M. J. Alexander, M. Hu, M. Xue, S. Pawson, and J. Perkins, 2006: The ARPS Stratospheric Gravity Wave Simulation over Greenland during 24 January 2005. *Geophysical Research Abstracts*, **8**, 04762

Lin, Y.-L., R.D. Farley, and H.D. Orville, 1983: Bulk parameterization of the snow field in a cloud model. *J. Climate Appl. Meteor.* **22**: 1065-1092

Linn, R.R., and P. Cunningham, 2005: Numerical simulations of grass fires using a coupled atmosphere-fire model: Basic fire behavior and dependence on wind speed. *J. Geophys. Res.* **110**, D13107, doi:10.1029/2004JD005597

Mandel, J., J.D. Beezley, and A.K. Kochanski, 2011: Coupled atmosphere-wildland fire modeling with WRF 3.3 and SFIRE 2011. *Geosci. Model. Dev.* **4:** 591-601

Martin, C., 2011: *FARSITE Comparison of Versions of LANDFIRE Fuel Characteristics: Rock House Fire 2011 Texas*. Technical Memo to SGT Inc., Greenbelt, MD. 8 pp.

Moeng, C.-H., 1984: A large-eddy-simulation model for the study of planetary boundary layer turbulence. *J. Atmos. Sci.* **41**: 2052-2062

Novy, C.H., R. Edwards, D. Imy, and S. Goss. *SPC and its Products*. ONLINE. 2013. Available: http://www.spc.ncep.noaa.gov/misc/about.html#FireWx [12 Feb. 2014].

Ntaimo, L., X. Hu, and Y. Sun, 2008: DEVS-FIRE: Towards an Integrated Simulation Environment for Surface wildfire Spread and Containment. *SIMULATION* **84**: 137-155

Perera, A.H., F. Schnekenburger, D.J.B. Baldwin, D. Boychuk, G. Dennis, and K. Weaver, 2003: BFOLDS – a spatially explicit stochastic model to simulate Boreal Forest Landscape Dynamics. *Forest Research Information Papers* **155**: 152-154.

Peterson, S.H. M.E. Morais, J.M. Carlson, P.E. Dennison, D.A. Roberts, M.A. Moritz, and D.R. Weise, 2009: *Using HFIRE for Spatial Modeling of Fire in Shrublands*. USDA Fpr. Serv. Res. Pap. PSW-RP-259. ONLINE. Available: http://nature.berkeley.edu/moritzlab/docs/Peterson_etal_HFire_2008.pdf [14 April 2014]

Rothermel, R.C., 1972: *A mathematical model for predicting fire spread rate in wildland fuels*. USDA For. Serv. Res. Pap. INT-115. ONLINE. Available: http://www.fs.fed.us/rm/pubs_int/int_rp115.pdf [14 April 2014]

Sinha, S., A. Jhalani, M.R. Ravi, and A. Ray, 2000: Modeling of pyrolysis in wood: a review. *J. Solar Energy*, Society of India, **10**(1): 41-62

Smith, W.S., M.J. Brown, and D. DeCroix, 2002: Evaluation of CFD Simulations Using Laboratory Data and Urban Field Experiments. *12th Joint Conference on the Applications of Air Pollution Meteorology with the Air and Waste Management Association*, Norfolk, VA, Amer. Met. Soc. ed.

Sun, W.Y., and C.Z. Chang, 1986: Diffusion model for a convective layer. Part I: Numerical simulation of convective boundary layer. *J. Climate Appl. Meteor.* **25**: 1445-1453.

Sullivan, A.L., 2007: Convective Froude number and Byram's energy criterion of Australian experimental grassland fires. *Proc. Combust. Instit.* **31**: 2557-2564

-------, 2008: A review of wildland fire spread modeling, 1990-present. *Int. J. Wildland Fire* **18**: 347-403

Sun, R., S.K. Krueger, M.A. Jenkins, M.A. Zulauf, and J.J. Charney, 2009: The importance of fire-atmosphere coupling and boundary-layer turbulence to wildfire spread. *Int. J. Wildland Fire* **18:** 50-60

Todd, B., 1999: *User documentation for the Wildland Fire Growth Model and the Wildfire Display Program*. Canadian Forest Service, Fire Research Network Report 37.

Tymstra, C., R.W. Bryce, B.M. Wotton, and O.B. Armitage, 2009: *Development and structure of Prometheus: the Canadian wildland fire growth simulation model*. Information Report NOR-X-417, Natural Resources Canada, Canadian Forestry Service, Northern Forestry Centre, Edmonton. ONLINE. Available: http://nofc.cfs.nrcan.gc.ca/bookstore_pdfs/31775.pdf [14 April 2014]

U.S. Department of the Interior. Office of Policy Analysis. 2012: *Wildland Fire Management Program Benefit-Cost Analysis: A Review of Relevant Literature*. ONLINE. Available: http://www.doi.gov/ppa/upload/Wildland_fire_literature_review_060812FINAL.pdf [12 Feb. 2014].

U.S. Library of Congress. Congressional Research Service. 2013: *Wildfire Management: Federal Funding and Related Statistics*, by Kelsi Bracmort. CRS Report R43077. Washington, DC: Office of Congressional Information and Publishing, August 30, 2013

Western Forestry Leadership Coalition. *The True Cost of Wildfire in the Western U.S.* ONLINE. 2009. Available: http://www.wflccenter.org/news_pdf/324_pdf.pdf [23 Feb 2014]

Wyngaard, J.C., 2004: Toward Modeling in the "Terra Incognita." *Jour. Atmos. Sci.*, **61**: 1816-1826.

------- and R.A. Brost, 1984: Top-down and bottom-up diffusion of a scalar in the convective boundary layer. *J. Atmos. Sci.* **41**: 102-112

Xue, M., K.K. Droegemeier, and V. Wong, 2000: The Advanced Regional Prediction System (ARPS) – A multiscale nonhydrostatic atmospheric simulation and prediction tool. Part I: Model dynamics and verification. *Meteor. Atmos. Physics*, **75:** 161-193

Xue, M., K.K. Droegemeier, V. Wong, A. Shapiro, K. Brewster, F. Carr, D. Weber, Y. Liu, and D.-H. Wang, 2001: The Advanced Regional Prediction System (ARPS) – A multiscale nonhydrostatic atmospheric simulation and prediction tool. Part II: Model physics and application. *Meteor. Atmos. Physics.* **76:** 134-165

Xue, M., K. Brewster, D. Weber, K. W. Thomas, F. Kong, and E. Kemp, 2003: Real-time storm-scale forecast support for IHOP 2002 at CAPS. *Preprints, 15th Conf. on NWP and 19th Conf. on Weather Analysis and Forecasting*, San Antonio, TX, *Amer. Meteor. Soc.*, 4B.3.

Zalesak, S.T., 1979: Fully dimensional flux-corrected transport algorithms for fluids. *J. Comput. Phys.* **31**: 335-362

APPENDIX A: OVERVIEW OF ARPS

The Advanced Regional Prediction System (ARPS) is a nonhydrostatic three-dimensional model system developed by the Center for Analysis and Prediction of Storms (CAPS) specifically for storm-scale modeling, although it is also intended for explicit prediction of weather systems at larger scales. The system includes self-contained routines for data assimilation as well as visualization and analysis of the results. As described in Xue et al. (2000), the prediction model is based upon the compressible viscous equations of motion, state (moist air), mass continuity, and heat energy conservation in Cartesian coordinates:

$$
\begin{aligned}
u' &= -mp_x\rho^{-1} + (f + f_m)v - \tilde{f}w - uwa^{-1} + F_u \\
v' &= -mp_y\rho^{-1} - (f + f_m)u - vwa^{-1} + F_v \\
w' &= -p_z\rho^{-1} - g + \tilde{f}u + \left(u^2 + v^2\right)a^{-1} + F_w \\
\rho &= p\left(R_d T\right)^{-1}\left[1 - q_v\left(\gamma + q_v\right)^{-1}\right]\left(1 + q_v + q_{li}\right) \\
\rho' &= -\rho\left\{m^2\left[(u/m)_x + (v/m)_y\right] + w_z\right\} \\
\theta' &= Q'\left(C_p\pi\right)^{-1}
\end{aligned}
$$

A prime denotes a total time derivative, a subscript denotes a partial derivative with respect to the stated variable, m is the map projection factor, ρ is density, f is the coriolis parameter, a is the radius of the Earth, F is the forcing due to friction, R_d is the gas constant for dry air, γ is the ratio of the gas constants for dry air and water vapor, q_{li} is the total liquid water and ice mixing ratio, θ is potential temperature, Q is adiabatic heating, C_p is the specific heat for dry air at constant pressure, and π is the Exner function. Also included are equations governing precipitation and microphysics,

hydrometeor species conservation, parameterization of subgrid-scale and boundary layer turbulence and mixing, and radiative and moisture exchange between the surface layer and the ground (which is in turn characterized by soil and vegetation models which vary monthly based on climatological tables). To more accurately model nonhydrostatic processes, the state variables for these equations are treated as perturbations around a hydrostatic base state.

To account for orographic effects, the model employs a curvilinear coordinate system with an impermeable lower boundary that conforms to the actual topography. The governing equations are mapped onto this terrain using the transformations $\xi(x)$, $\eta(y)$, and $\zeta(x,y,z)$ for the spatial derivatives as follows:

$$J_1 \equiv -z_\xi y_\eta, J_2 \equiv -z_\eta x_\xi, J_3 \equiv -z_\zeta y_\eta, J_4 \equiv z_\zeta x_\xi$$
$$\sqrt{G} = z_\zeta x_\xi y_\eta$$
$$\phi_x = \left[(J_3\phi)_\xi + (J_1\phi)_\zeta \right] \Big/ \sqrt{G}$$
$$\phi_y = \left[(J_4\phi)_\eta + (J_2\phi)_\zeta \right] \Big/ \sqrt{G}$$
$$\phi_z = \left(x_\xi y_\eta \phi \right)_\zeta \Big/ \sqrt{G}$$

The transformation parallels the terrain at the surface and transitions to Cartesian coordinates aloft as shown in Fig. 11. The vertical grid stretching is governed by either a hyperbolic-tangent stretching function or a cubic function as described in Xue and Thorpe (1991).

In this curvilinear framework, the governing equations are solved using finite differences on an Arakawa C-grid, chosen for better representation of the geostrophic adjustment and straightforward treatment of advection/transport. Two measures are

employed to prevent instability from acoustic waves while maintaining computational efficiency: first, an artificial divergence damping term is included in the transformed governing equations; and second, a mode-splitting technique is employed whereby the acoustically-active terms are integrated in several small time steps within each large time step used for the slower modes. Multiple options exist for integrating the large time steps, including 2^{nd}- or 4^{th}-order centered leapfrog schemes and a flux-corrected transport scheme for advection of positive-definite scalars (which was utilized for the simulations in this study). For a full treatment of ARPS equations, parameterizations, and finite-difference schemes, the reader is referred to Xue et al. (2000) and Xue et al. (2001).

The treatment of orographic effects in the model was first verified against the analytical solution for various types of flows (linear/nonlinear waves, hydrostatic/nonhydrostatic regimes) in the vicinity of an idealized bell-shaped mountain. (See Fig. A.1.) The model was then tested against observations and previous simulations of the 1972 Boulder, CO windstorm, with general agreement in the results. Validation of the soil-vegetation model and the treatment of surface and planetary boundary layer (PBL) physics was performed in a case study using data from the Wangara experiment; the simulated surface fluxes and PBL evolution agreed "remarkably well" with the observed data. (See Figs. A.2 and A.3.) Additional validation of the surface model in a variety of conditions was later carried out using the Oklahoma Mesonet.

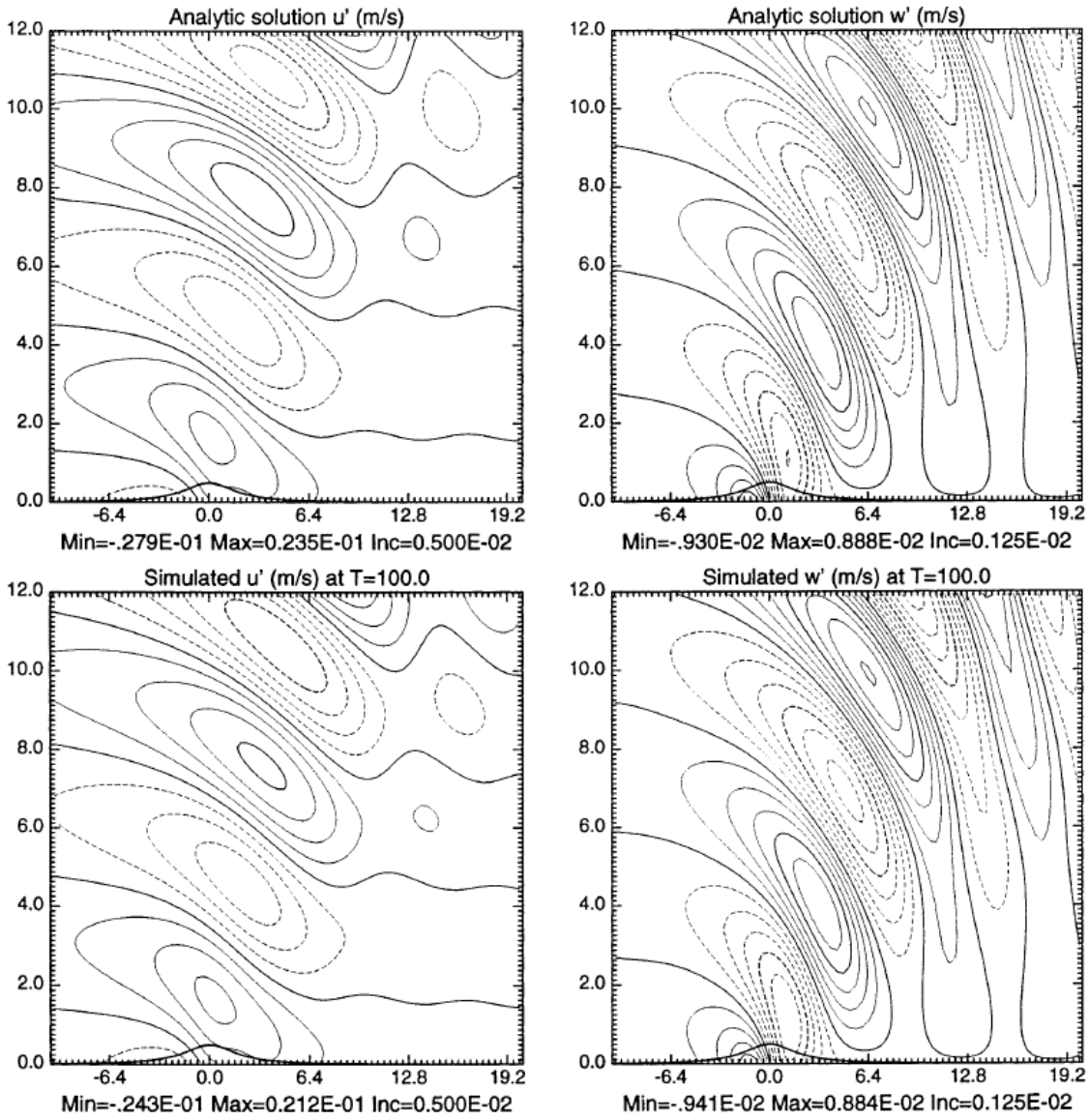

Figure A.1: Analytic (upper) and ARPS-simulated (lower) solutions for *u'* (left) and *w'* (right) after 100 advective time-scale steps for a finite-amplitude nonlinear nonhydrostatic wave over an idealized bell-shaped mountain of height 503 m with a 2-km half-width (from Xue et al., 2000, p.179)

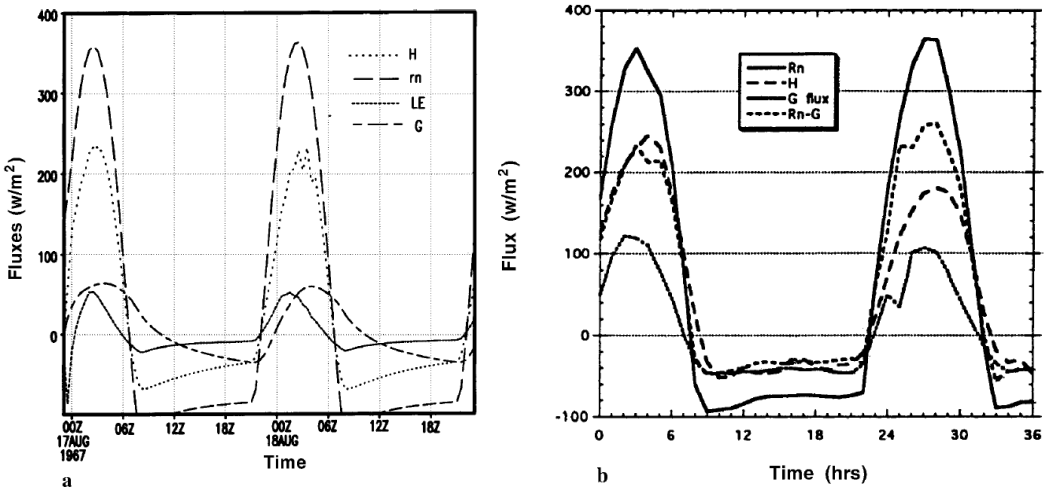

Figure A.2: Simulated (left) and observed (right) surface fluxes of net radiation (R_n) and sensible (H), latent (LE), and ground heat (G) for the Wangara experiment, Days 33-34 (from Xue et al., 2001, p.150)

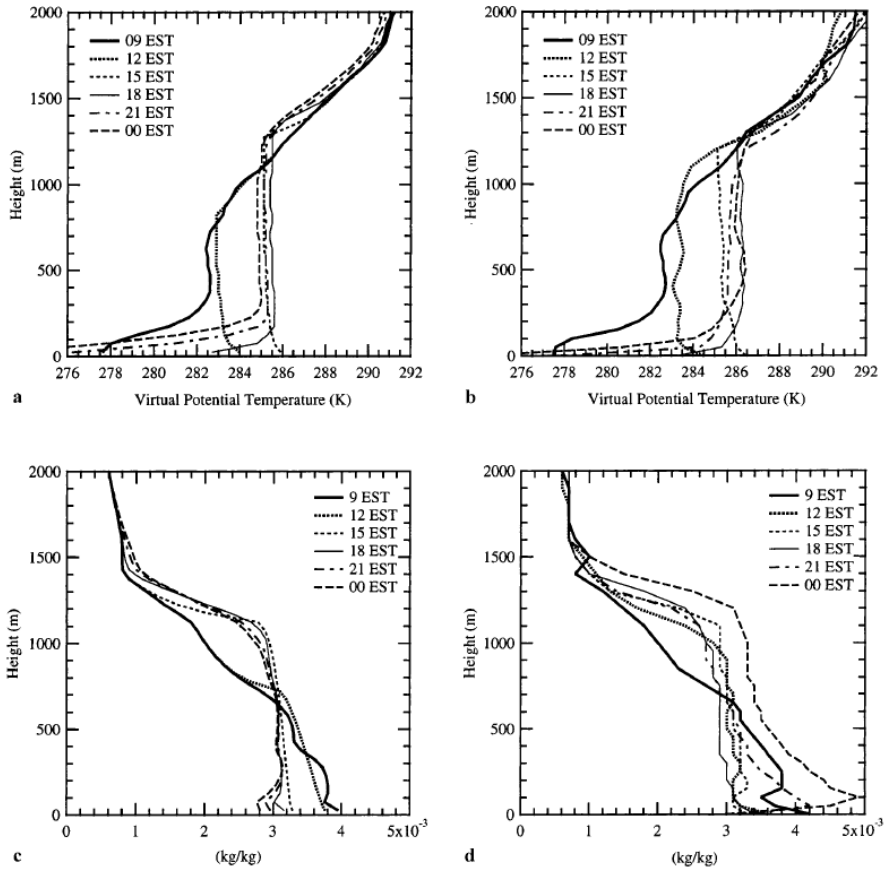

Figure A.3: Simulated (left) and observed (right) profiles of virtual potential temperature (top) and specific humidity (right) for Day 33 of the Wangara experiment (from Xue et al., 2001, p.149)

Various case studies (described in Xue et al., 2001) illustrate the accuracy and multi-scale capability of ARPS in strongly-convective situations. The 20 May 1977 Del City tornadic supercell was reproduced from an initialized warm bubble in a sounding-derived environment on a 64×64×16 km grid with 1 km horizontal resolution and vertical resolution stretched from 100 m at the surface to 700 m at the upper boundary; three different scalar advection schemes (flux-corrected transport, 4^{th}-order centered, Lafore positive-definite 4^{th}-order centered) and two different microphysical parameterizations (ice, Kessler warm-rain) were employed. All simulations were consistent with expected behavior, although the monotonic flux-corrected transport scheme and ice microphysics produced the best results. (See Fig. A.4.)

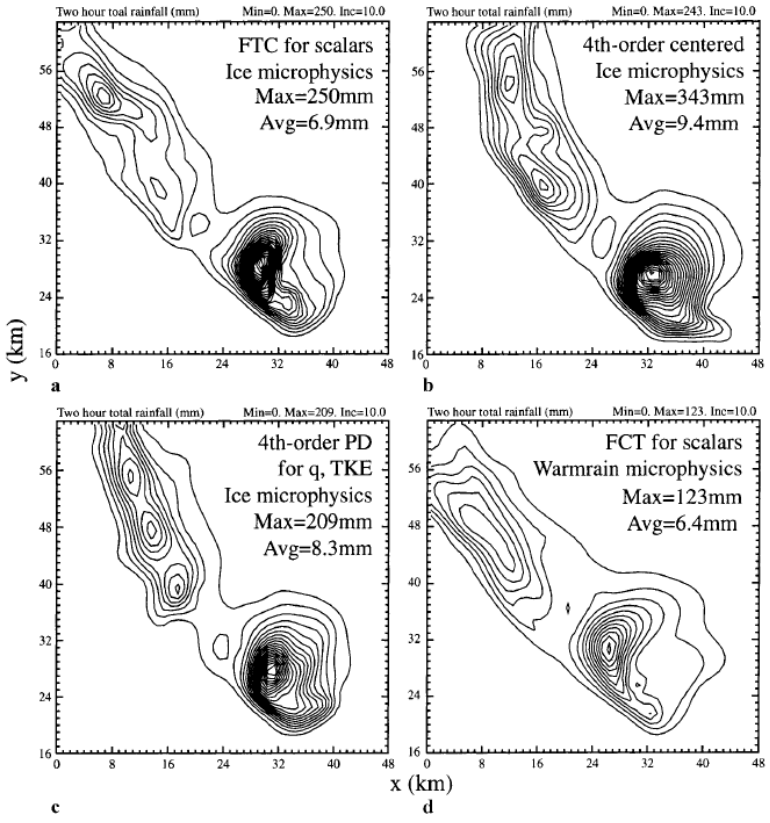

Figure A.4: Two-hour accumulated precipitation from simulations of the 20 May 1977 Del City supercell storm (from Xue et al., 2001, p.154)

The 21-23 January 1999 tornado outbreak case was modeled using nested grids to resolve both synoptic (215×155×43, 32-km horizontal resolution, Kain-Fritsch cumulus parameterization) and mesoscale (372×372×43, 6-km horizontal resolution) features. The resulting forecast compared favorably with both the corresponding Eta analysis and the actual observations throughout the 48-hour forecast. (See Fig. A.5.) Furthermore, analysis on a 2-km grid nested inside the 6-km grid was able to resolve supercell morphology and low-level rotation in the outbreak area. (See Fig. A.6.) Other successful convective simulations include the 28 March 2000 Fort Worth tornado and the initiation of thunderstorms along a dryline during the International H_2O Project (Xue et al., 2003a). This demonstrated ability to accurately simulate rapid changes in an unstable environment makes ARPS a good candidate for coupling with a wildfire model.

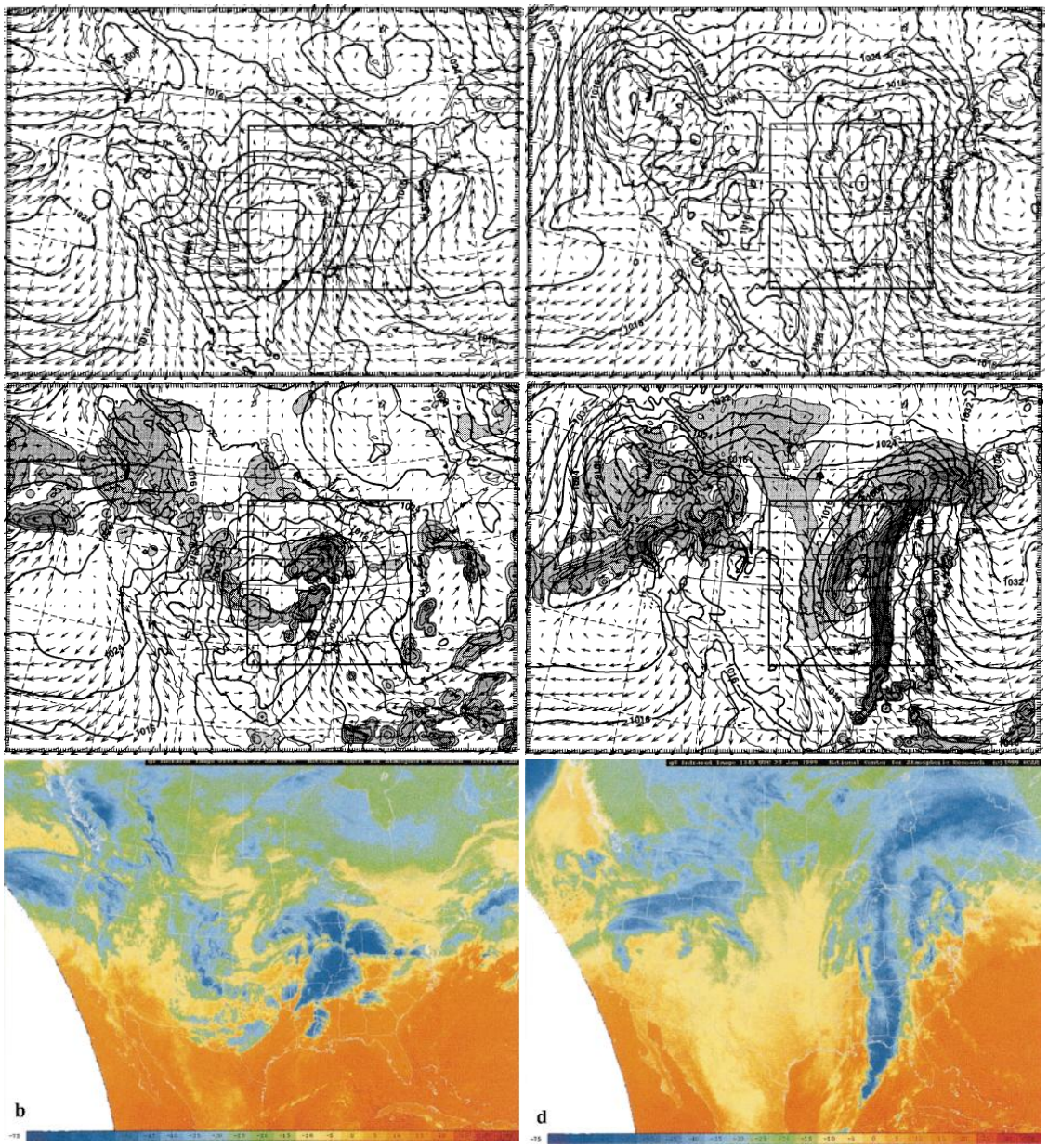

Figure A.5: Eta analysis (top) and ARPS forecast (middle) valid 00Z (left) and 12Z (right) on 22 January 1999; compare ARPS and Eta sea level pressure (hPa) contours, as well as ARPS precipitation (shaded) and IR cloud top temperature satellite images (bottom) at 2245Z on 21 January (left) and 1045Z on 22 January (right) (from Xue et al., 2001 pp.158-160)

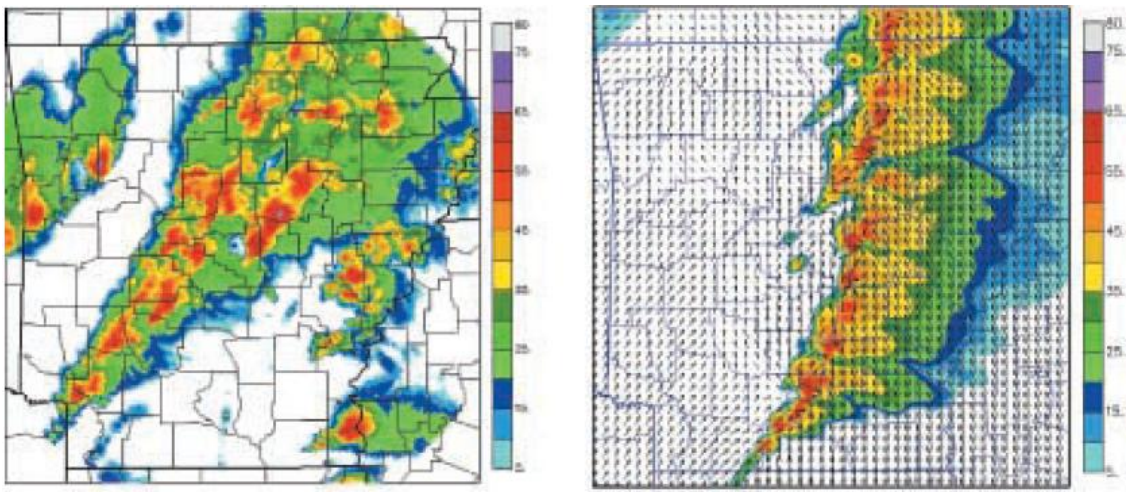

Figure A.6: Actual radar observation from KLZK (left) and ARPS 14-hour forecast composite reflectivity (right) for 02Z on 22 January 1999 (from Xue et al. 2001, p.148)

APPENDIX B: QUASI-DISCRETE HEAT RELEASE DERIVATION

As stated in Chapter 3, the basic premise of the quasi-discrete approach is the assumption that the fire may be represented within a DEVS-FIRE grid cell of length and width Δx as a straight line segment moving through the cell at a constant rate R obtained by applying the Rothermel formula (10) to the current conditions (fuel type, wind speed and direction, terrain, etc.). From Fig. B.1, if the fire front is oriented at an angle θ relative to the proximal grid axis, the distance from it to any point (x,y) within the cell is

$$D = \frac{x}{\cos\theta} + b\sin\theta$$

Since $b = y - a$ and $a = x\tan\theta$,

$$D = \frac{x}{\cos\theta} + (y - x\tan\theta)\sin\theta = x\left(\frac{1-\sin^2\theta}{\cos\theta}\right) + y\sin\theta$$

which reduces to

$$D = x\cos\theta + y\sin\theta$$

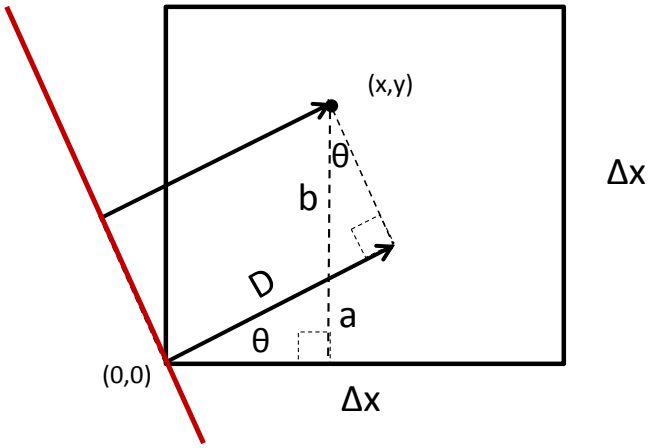

Figure B.1: Geometric framework for determining distance from fire front (red line) to a point (x,y) inside a DEVS-FIRE grid cell with resolution Δx

Since the fire front is spreading at a rate R, the time at which it reaches the point $\boldsymbol{x} = (x,y)$ is given by

$$t_i(\boldsymbol{x}) = t_i(\boldsymbol{x_o}) + \frac{D}{R} = t_i(\boldsymbol{x_o}) + \frac{x\cos\theta}{R} + \frac{y\sin\theta}{R}$$

where $\boldsymbol{t_i(x_o)}$ is the time at which the cell ignites in the fire spread model. It should be noted that this method proceeds edge-to-edge, while the fire spread model operates center-to-center; the delay implied by this discrepancy is minimal and consistently applied to all cells after ignition. Furthermore, it is necessary to maintain consistency between the heat model and the spread model, avoiding heat release from cells that the spread model never ignites. (Xiaolin Hu and Haidong Xue, personal communication)

Locally, combustion is modeled as an exponential decay of the fuel fraction as described by (25). Spatially averaging this fuel fraction over the grid cell requires the area integral given in (27). When $\theta = 0$ ("straight" spread), evaluating (27) is relatively straightforward. As shown in Fig. B.2, the burn area is rectangular with length Δx and width equal to $D = R[t\text{-}t_i(\boldsymbol{x_o})] \equiv Rt_e$ while the fire front is inside the cell and Δx after the front leaves the cell at time $t_f = t_i(\boldsymbol{x_o}) + \Delta x/R$. During this time interval, (27) takes the form

$$F(t) = 1 - \frac{1}{(\Delta x)^2}\int_0^{\Delta x}\int_0^{Rt_e} 1 - \exp\left(\frac{\frac{x}{R} - t_e}{W}\right) dx\, dy$$

$$= 1 - \frac{Rt_e}{\Delta x} + \frac{1}{(\Delta x)^2}\exp\left(\frac{-t_e}{W}\right)\int_0^{\Delta x}\int_0^{Rt_e} \exp\left(\frac{x}{RW}\right) dx\, dy$$

$$= 1 + \left(\frac{R\,W}{\Delta x}\right)\left[1 - \frac{t_e}{W} - \exp\left(\frac{-t_e}{W}\right)\right]$$

After the fire front leaves the cell (i.e. $t_e \geq \Delta x/R$), the integral is

$$F(t) = 1 - \frac{1}{(\Delta x)^2}\int_0^{\Delta x}\int_0^{\Delta x} 1 - \exp\left(\frac{x}{R} - t_e}{W}\right) dx\, dy$$

$$= \frac{1}{(\Delta x)^2}\exp\left(\frac{-t_e}{W}\right)\int_0^{\Delta x}\int_0^{Rt_e} \exp\left(\frac{x}{RW}\right) dx\, dy$$

$$= \left(\frac{R\,W}{\Delta x}\right)\exp\left(\frac{-t_e}{W}\right)\left[\exp\left(\frac{\Delta x}{R}\right) - 1\right]$$

These are the formulas given in (28).

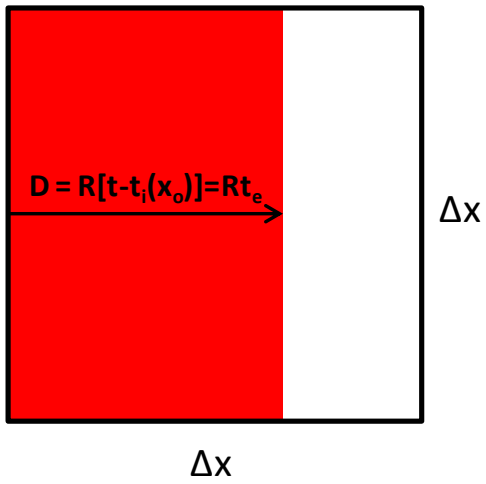

Figure B.2: Schematic of "straight" fire spread through a DEVS-FIRE cell. The current burning area is shown in red.

As shown in Fig. B.3, the case of "diagonal" spread ($\theta = \pi/4$) is complicated by the changing geometry of the burn area, which is simplified by rotating the coordinate axis to align the ordinate with the direction of spread (thereby eliminating the $y\sin\theta/R$ term). Up until time $t_c = t_i(\boldsymbol{x_o}) + \Delta x/R\sqrt{2}$, the burn area is a triangle and (27) takes the form

$$F(t) = 1 - \frac{1}{(\Delta x)^2}\int_0^{Rt_e}\int_{-x}^{x} 1 - \exp\left(\frac{\frac{x}{R} - t_e}{W}\right) dy\, dx$$

$$= 1 - \frac{1}{(\Delta x)^2}\int_0^{Rt_e} 2x\left[1 - \exp\left(\frac{x}{RW}\right)\exp\left(\frac{-t_e}{W}\right)\right] dx$$

$$= 1 - \left(\frac{Rt_e}{\Delta x}\right)^2 + 2\left(\frac{R\,W}{\Delta x}\right)^2\left[\frac{t_e}{W} + \exp\left(\frac{-t_e}{W}\right) - 1\right]$$

For t_e between t_c and $t_f = t_i(\boldsymbol{x_o}) + \Delta x\sqrt{2}/R$, the burn area is pentagonal. During this interval, the integral must be split as follows:

$$F(t) = 1 - \frac{1}{(\Delta x)^2}\left[\int_0^{\frac{\Delta x}{\sqrt{2}}}\int_{-x}^{x} 1 - \exp\left(\frac{\frac{x}{R} - t_e}{W}\right) dy\, dx + \int_{\frac{\Delta x}{\sqrt{2}}}^{Rt_e}\int_{x-\Delta x\sqrt{2}}^{\Delta x\sqrt{2}-x} 1 - \exp\left(\frac{\frac{x}{R} - t_e}{W}\right) dy\, dx\right]$$

$$= 1 - \frac{1}{(\Delta x)^2}\left[\int_0^{\frac{\Delta x}{\sqrt{2}}} 2x\left[1 - \exp\left(\frac{x}{RW}\right)\exp\left(\frac{-t_e}{W}\right)\right] dx + \int_{\frac{\Delta x}{\sqrt{2}}}^{Rt_e} 2(\Delta x\sqrt{2} - x)\left[1 - \exp\left(\frac{x}{RW}\right)\exp\left(\frac{-t_e}{W}\right)\right] dx\right]$$

$$= \left(\frac{Rt_e}{\Delta x} - \sqrt{2}\right)^2 + 2\left(\frac{R\,W}{\Delta x}\right)^2\left[1 + \frac{\Delta x\sqrt{2}}{R} - t_e + \left[\exp\left(\frac{-t_e}{W}\right)\right]\left[1 - 2\exp\left(\frac{\Delta x}{R\,W\sqrt{2}}\right)\right]\right]$$

Finally, for t_e greater than t_f (i.e. after the fire front departs), the integral is

$$F(t) = 1 - \frac{1}{(\Delta x)^2}\left[\int_0^{\frac{\Delta x}{\sqrt{2}}}\int_{-x}^{x} 1 - \exp\left(\frac{\frac{x}{R} - t_e}{W}\right) dy\, dx + \int_{\frac{\Delta x}{\sqrt{2}}}^{\Delta x\sqrt{2}}\int_{x-\Delta x\sqrt{2}}^{\Delta x\sqrt{2}-x} 1 - \exp\left(\frac{\frac{x}{R} - t_e}{W}\right) dy\, dx\right]$$

$$= 1 - \frac{1}{(\Delta x)^2}\left[\int_0^{\frac{\Delta x}{\sqrt{2}}} 2x\left[1 - \exp\left(\frac{x}{RW}\right)\exp\left(\frac{-t_e}{W}\right)\right] dx + \int_{\frac{\Delta x}{\sqrt{2}}}^{\Delta x\sqrt{2}} 2(\Delta x\sqrt{2} - x)\left[1 - \exp\left(\frac{x}{RW}\right)\exp\left(\frac{-t_e}{W}\right)\right] dx\right]$$

$$= 2\left(\frac{R\,W}{\Delta x}\right)^2 \exp\left(\frac{-t_e}{W}\right)\left[1 + \exp\left(\frac{\Delta x\sqrt{2}}{R\,W}\right) - 2\exp\left(\frac{\Delta x}{R\,W\sqrt{2}}\right)\right]$$

These are the formulas given in (29).

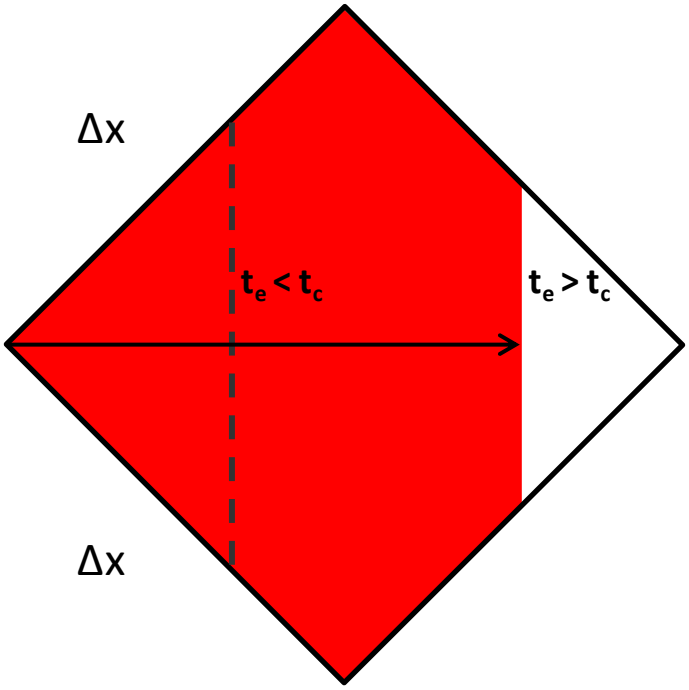

Figure B.3: As in Fig. B.2, but for the case of diagonal fire spread. Dotted line delineates example burn area for $t_e < t_c$.

APPENDIX C: ARPS TURBULENCE PARAMETERIZATION NEAR ENHANCED SURFACE HEATING

A. Overview

Atmospheric models operating at different scales account for turbulent mixing in different ways. When the spatial averaging scale is much smaller than the length scale of the turbulence (large-eddy simulation or LES), the turbulent fluxes are largely resolved by the filtered motions calculated on the model grid; however, when the opposite is true (as is the case in mesoscale modeling), turbulent fluxes are not resolved and must be estimated using subgrid-scale parameterizations. When the turbulence length scale and the effective grid scale are nearly equivalent, turbulence simulation/modeling enters "terra incognita" for which parameterizations have not been explicitly developed. (Wyngaard, 2004) Numerical simulations of processes in the atmospheric boundary layer all too often select a turbulence closure scheme from one of these regimes for operation in the other, apparently without considering the possible ramifications.

As an example of one such choice, this project investigates comparisons between the local 1.5-order TKE closure scheme detailed in Moeng (1984) and Wyngaard and Brost (1984) with the non-local closure scheme described by Sun and Chang (1986). Both schemes parameterize kinematic fluxes and production/dissipation of turbulent kinetic energy (TKE) using eddy diffusivity coefficients dependent on turbulence length scale *l*:

$$K_m = 0.1 l \overline{\mathrm{E}}^{\frac{1}{2}} \qquad K_h = \left(1 + \frac{2l}{\Delta s}\right) K_m \qquad \varepsilon = \mathrm{C}\overline{\mathrm{E}}^{3/2}/l$$

The key difference lies in the definition of l for each scheme as shown in the equation sets below:

$$\textit{Moeng and Wyngaard}:\ l = \Delta s \quad \text{(unstable)}, \quad l = \min\left(\Delta s, \frac{1}{2}\frac{\bar{E}^{1/2}}{\beta(\partial\bar{\theta}/\partial z)}\right) \quad \text{(stable)}$$

$$\textit{Sun and Chang}:\ l = 0.25\left\{1.8Z_i\left[1 - \exp\left(-\frac{4z}{Z_i}\right) - 0.0003\exp\left(\frac{8z}{Z_i}\right)\right]\right\} \quad \text{(unstable)}$$

Δs is the effective grid resolution (i.e. the geometric mean of the grid spacing in the x, y, and z directions), E is the turbulent kinetic energy, β is a reference buoyancy parameter, θ is potential temperature, and Z_i is the depth of the mixed layer. When the boundary layer is stable, the Sun and Chang parameterization behaves the same as the Moeng and Wyngaard parameterization; in a convective boundary layer (CBL), the length scale in the Sun and Chang scheme is smoothly decreased from its value at Z_i to 3% of that value at the third grid level above Z_i in order to damp vigorous gravity waves that can develop in the inversion above.

B. Method

The degree of vertical mixing from turbulence may be tracked based on the assumption that the vertical profile of a conserved scalar quantity should be constant within a well-mixed layer. In the case of dry adiabatic motion, potential temperature θ is an example of such a scalar; therefore, in the absence of moisture effects, the vertical θ profile can be used to estimate the mixing depth. In nature, boundary layer mixing of θ (i.e. sensible heat flux) is generally driven by variations in the surface energy budget, which can be spatially and temporally complex; however, to simplify the problem under study, a constant, spatially-uniform heat flux of 1 kW/m^2 was specified over an

idealized, flat, homogeneous surface. A group of four two-dimensional ARPS simulations was performed for each TKE scheme on a 100km-by-6km grid at horizontal resolutions of 100 m, 500 m, 1 km, and 2 km. The vertical grid was hyperbolically stretched from 6m resolution just above ground level to an average of 120 m aloft, with an isothermal (288 K) initial atmosphere and a vertically-uniform westerly wind of 5 m/s. Impermeable top and bottom boundary conditions and periodic lateral boundary conditions were employed on the assumption that convection does not impact the top boundary and the surface spatial homogeneity extends an infinite distance in all directions.

Turbulence was induced via random temperature perturbations ranging from 0 to 1 K introduced at the first level AGL at initialization, and the roughness length was held constant at 0.01 m. To ensure numerical stability, mode splitting was employed with an integration time step of 0.5 seconds for the governing equations and 0.25 seconds for acoustic wave modes. The characterization of the turbulence constituted a complicating factor; since it is recommended that anisotropy be assumed (i.e. only vertical mixing is considered) when the horizontal grid resolution is much greater than the vertical grid resolution (120 m in this case), isotropic turbulence was specified for the 100 m and 500 m cases while anisotropic turbulence was specified for the 1 km and 2 km cases.

Two-dimensional plots of potential temperature in the lowest 3 km were used for qualitative comparison of the results. In order to assess any approach to "terra incognita," the ratio of the turbulence length scale (diagnosed by ARPS) to the vertical resolution was plotted as a time series for each simulation. Finally, the vertical profiles

of layer-averaged potential temperature, zonal wind, and resolved kinematic heat flux (estimated as the sample covariance of the perturbation vertical velocity and perturbation potential temperature relative to the layer means) were plotted at regular intervals to provide a quantitative indication of the impact of the choice of TKE parameterization scheme on model performance.

C. Results and Discussion

Comparison of the plotted 30-km-by-3-km theta profile sequences indicated that the 500 m and 2 km simulations are qualitatively similar to the 100 m and 1 km simulations, respectively. Therefore, discussion here will focus on the results from the 100 m and 1 km simulations. Figure C.1 gives the time series of the ratio between the calculated turbulence length scale and the effective grid resolution at 1 km AGL for each model run. It is clear that the 100 m Sun and Chang run remains firmly in the LES regime, while the 100 m Moeng and Wyngaard run is generally much closer to "terra incognita." Similarly, the 1 km Sun and Chang run is near "terra incognita" while the 1 km Moeng and Wyngaard simulation is firmly in the mesoscale modeling regime.

The use of the Moeng and Wyngaard formulation outside the LES regime produces undesirable artifacts. The much smaller turbulence length scale implies much greater dissipation of TKE and therefore greatly reduced vertical theta mixing. As a result (as shown in Fig. C.2), an unrealistically-intense superadiabatic layer develops in the first half-hour after initialization and instigates an explosive period of autoconvective adjustment. When the Sun and Chang formulation is used at 1 km

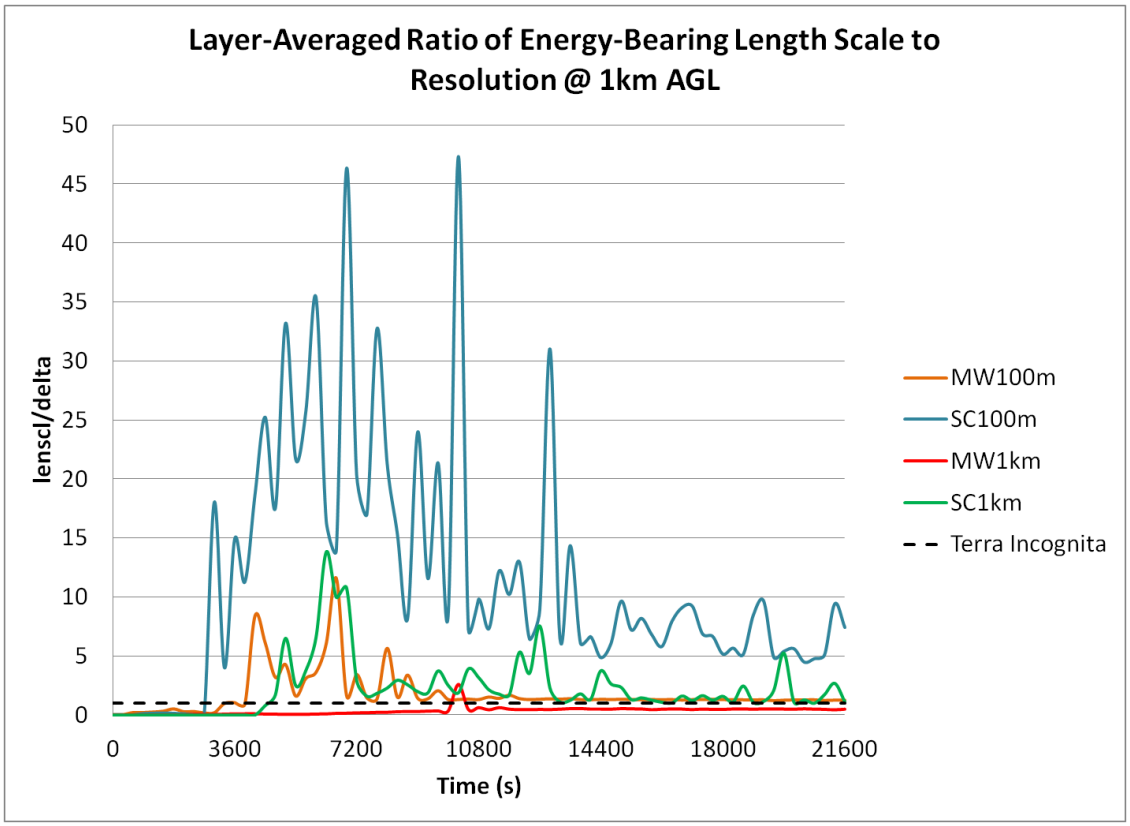

Figure C.1: Ratio of turbulence length scale to vertical grid resolution as a function of time for 100 m Moeng and Wyngaard (orange), 100 m Sun and Chang (blue), 1 km Moeng and Wyngaard (red), and 1 km Sun and Chang simulations (green). A ratio of unity (a rough benchmark for "terra incognita") is plotted with a dashed line.

horizontal resolution instead (see Fig. C.3), the turbulent length scale in the CBL tends to be somewhat greater (although this difference decreases over time as the CBL depth Z_i increases), which means the mixing is more efficient. The superadiabatic surface layer is much more realistic in both depth and intensity, and no explosive adjustment occurs.

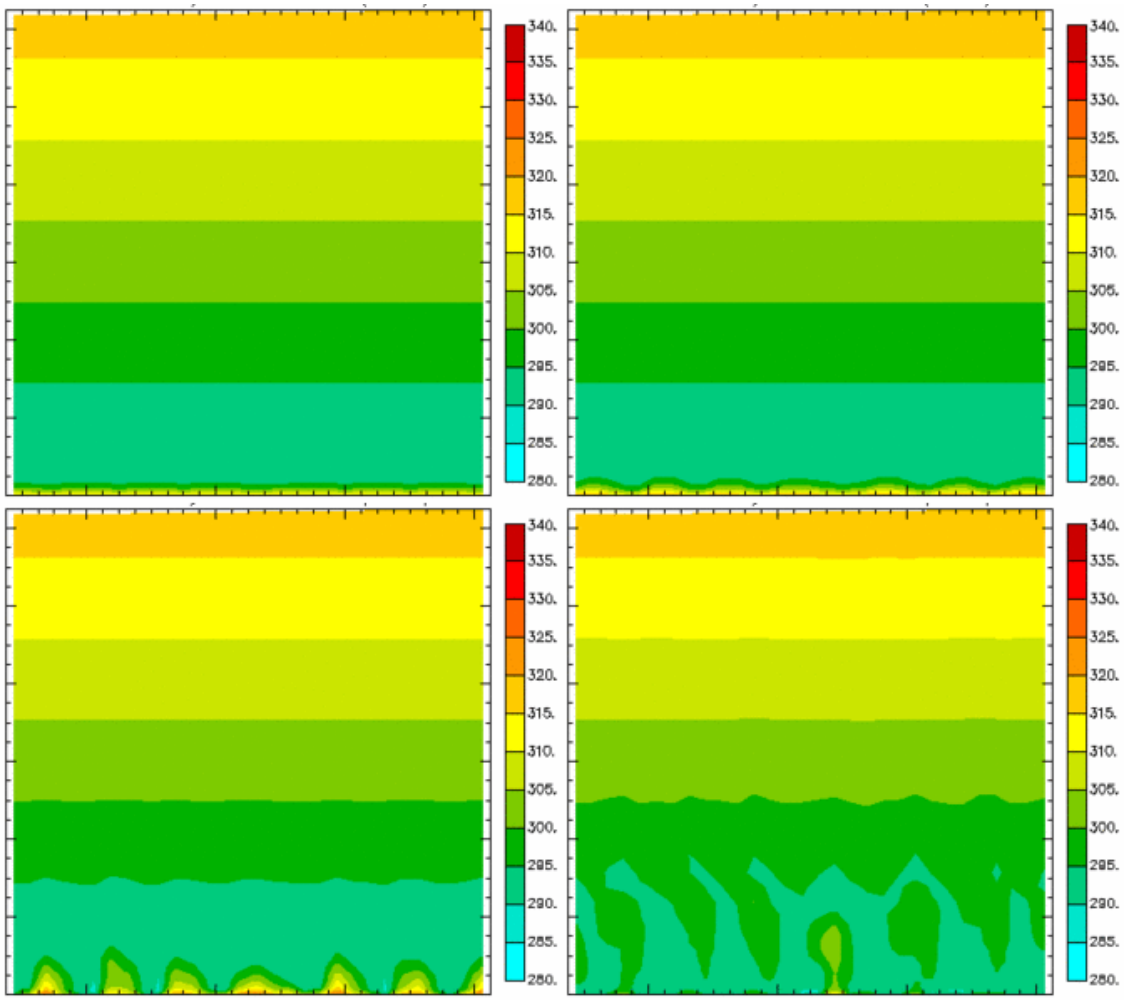

Figure C.2: Vertical profile of potential temperature from x = 35 to x = 65 km and from z = 0 to z = 3 km for the Deadorff 1km resolution ARPS run at t=2100 s (upper left), 2400 s (upper right), 2700 s (lower left) and 3000 s (lower right)

Additional difficulty is clear from the vertical kinematic heat flux profiles resolved on the model grids for the various runs as shown in Fig. C.4. Initially, all profiles show the "S" shape characteristic of convective boundary layers (Evgeni Fedorovich, personal communication) and, interestingly, the Sun and Chang 1 km run shows a more intense vertical gradient than its Moeng and Wyngaard counterpart. However, while the other simulations tend to mitigate gradients over time, the Moeng and Wyngaard 1 km run does not. The near-surface flux appears to be increasing

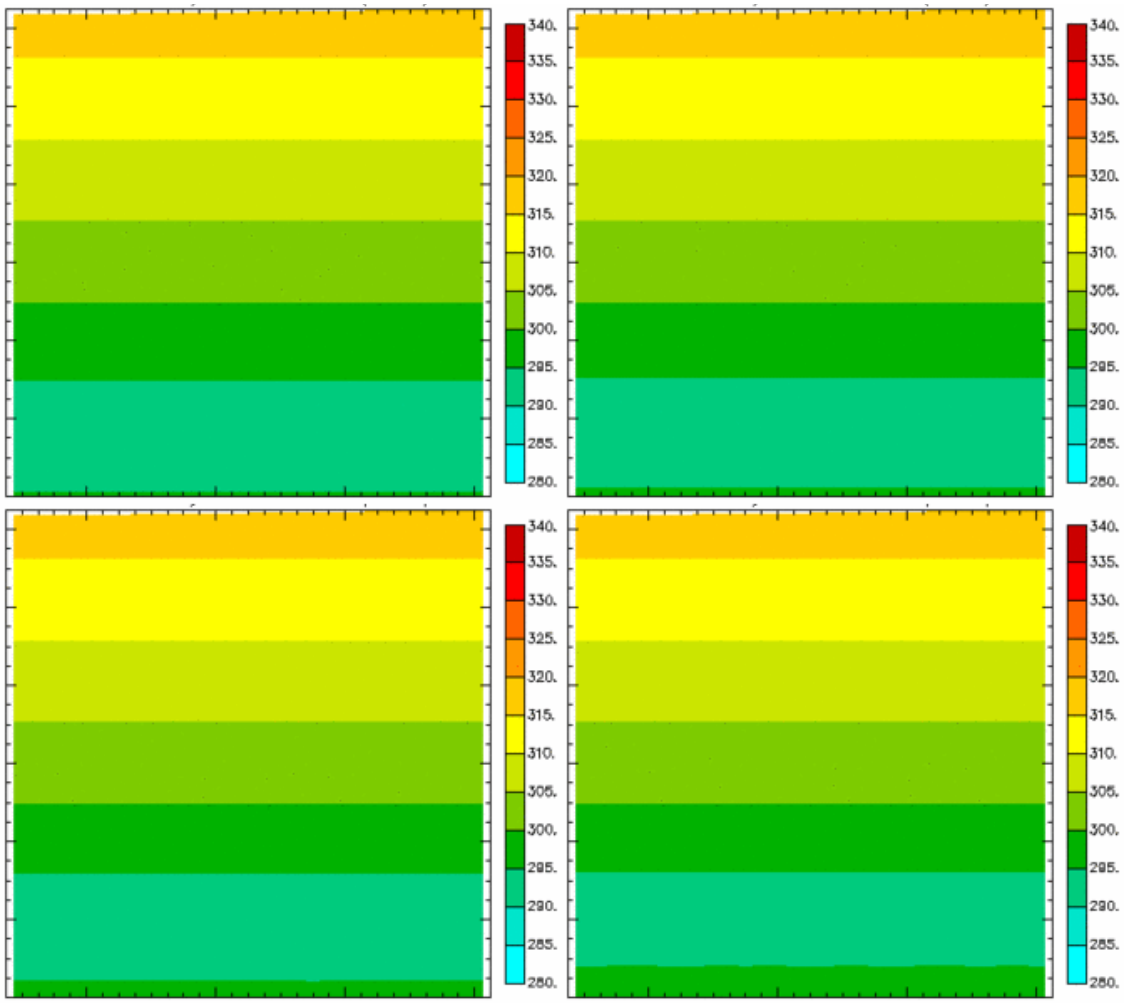

Figure C.3: Same as Fig. C.2, but for Sun and Chang 1 km resolution ARPS run.

rapidly at the end of the run, suggesting the possibility of numerical instability and model crash if the simulation is carried much beyond six hours. Overall, it appears that using the Moeng and Wyngaard formulation is not reliable for boundary layer mesoscale applications with enhanced surface heating.

Having determined that the Sun and Chang parameterization is superior at coarser resolutions, it is now instructive to consider results using grid resolutions closer to the LES regime. From Fig. C.1, it is clear that the length scale for the Sun and Chang simulation is much greater than it is for the Moeng and Wyngaard simulation; the

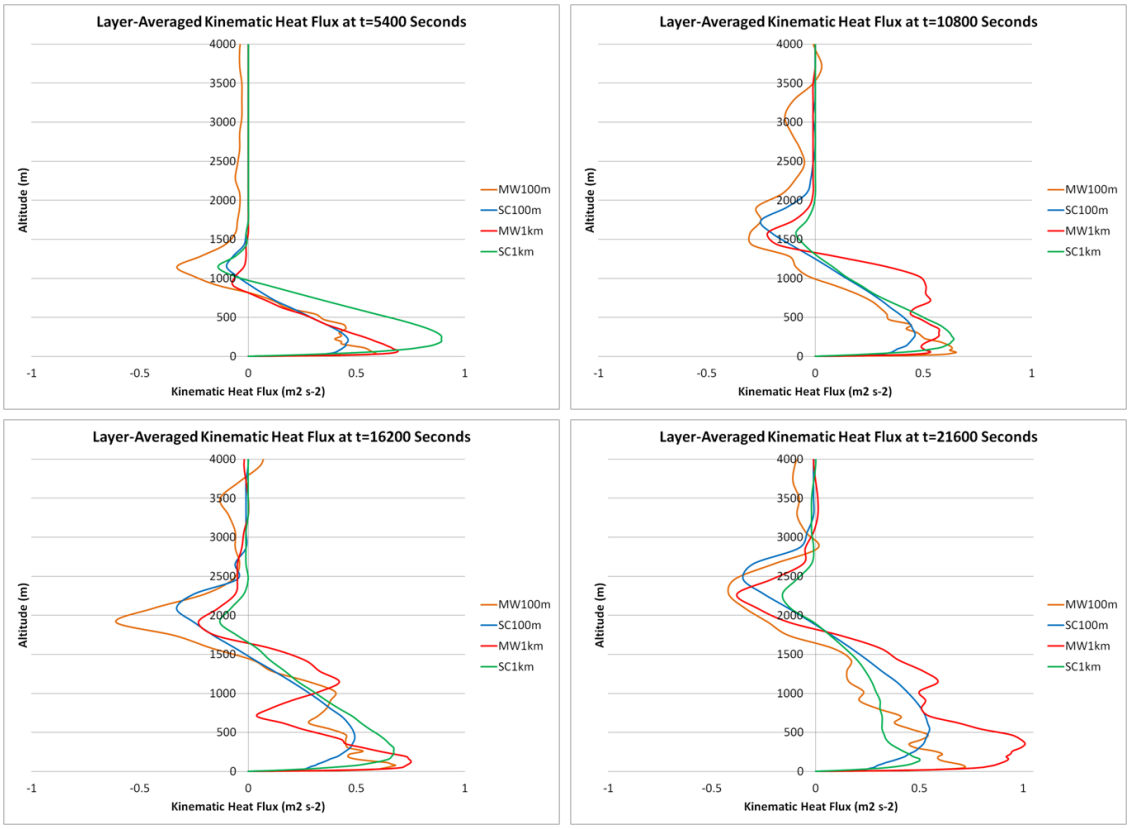

Figure C.4: Vertical profiles of grid-resolved kinematic heat flux at 1.5 hours (upper left), 3 hours (upper right), 4.5 hours (lower left), and 6 hours (lower right) with simulations designated by color as in Fig. C.1.

mixing is more robust and persistent, since dissipation is inversely related to length scale. This, in turn, leads to a mixed layer depth much greater (several hundred meters by the end of the simulation) than for any of the other simulations as shown in Fig. C.5. Since the use of the Sun and Chang formulation in ARPS was only validated against Wangara experiment data for 1-D mixing (i.e. neglecting horizontal turbulent mixing as specified for the 1 km and 2 km simulations in this study), it would seem that the mixed layer depth for the other three simulations is more nearly correct while the 100m Sun and Chang simulation overestimates it. Also, one would expect from the stability correction to the log-wind profile used for Monin-Obukhov similarity that robust

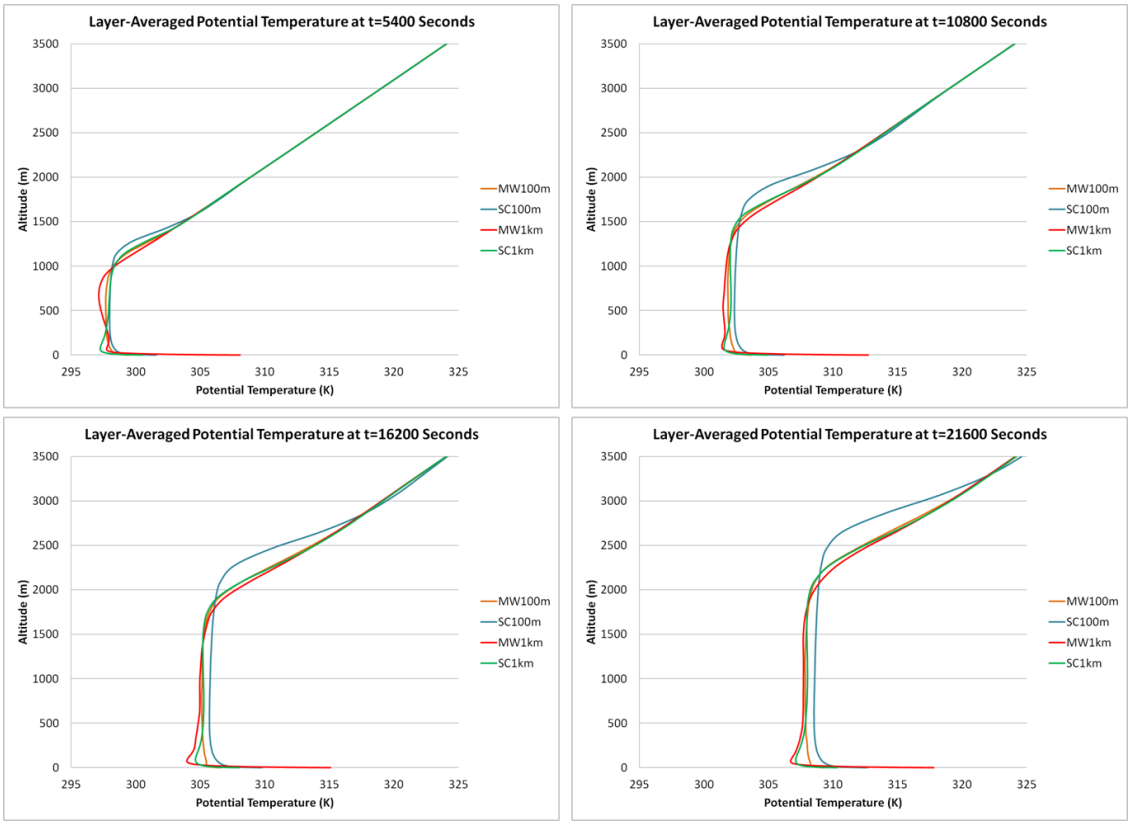

Figure C.5: Layer-averaged potential temperature profiles for t = 1.5, 3, 4.5, and 6 hours, arranged as in Fig. C.4.

buoyancy-driven turbulence would largely disperse the base-state flow near the surface; the layer-averaged zonal wind profiles in Fig. C.6 show this to be the case for the Moeng and Wyngaard runs but not so much for the Sun and Chang runs. Therefore, while the Sun and Chang parameterization appears to be somewhat more adaptable across the "terra incognita" than the Moeng and Wyngaard formulation is, the Moeng and Wyngaard formulation is more reliable for LES applications.

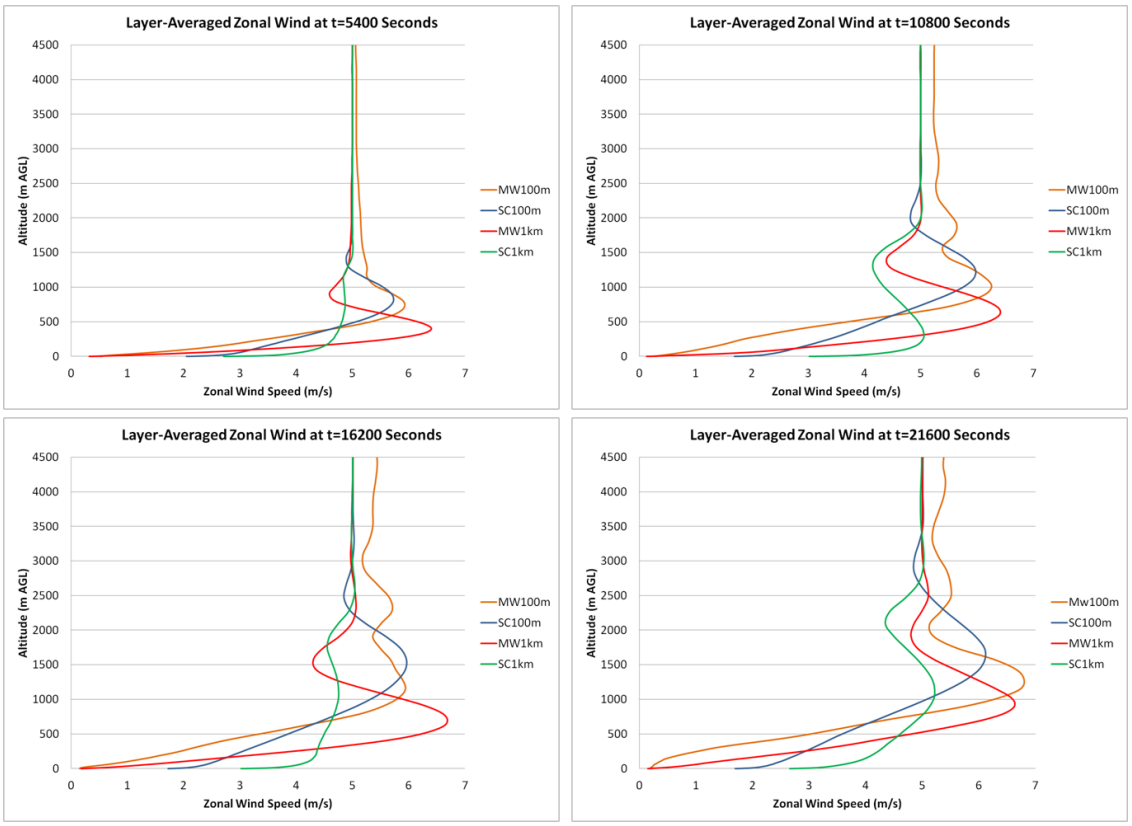

Figure C.6: Layer-averaged zonal wind profiles for t = 1.5, 3, 4.5, and 6 hours, arranged as in Fig. C.4.